# Robust Control Of Surge And Rotating Stall In An Axial Compressor

by

**Shengfang Liao**

B.E., Tsinghua University, Beijing, 1991
M.E., Institute of Engineering Thermophysics, Beijing, 1994

**Submitted to the Department of Aeronautics and Astronautics in partial fulfillment of the requirements for the degree of**

**Doctor of Philosophy**

at the

Massachusetts Institute of Technology

September 2000



Author_____
Department of Aeronautics and Astronautics
August 11, 2000

Certified by_____
James D. Paduano
Principal Research Engineer
Thesis Supervisor

Certified by_____
Alan H. Epstein
R. C. MacLaurin Professor of Aeronautics and Astronautics

Certified_____
Choon S. Tan
Senior Research Engineer

Certified by_____
Eric Feron
Associate Professor of Aeronautics and Astronautics

Accepted by_____
Nesbitt W. Hagood
Associate Professor of Aeronautics and Astronautics
Chairman, Committee on Graduate Students

# Robust Control Of Surge And Rotating Stall In An Axial Compressor

by

Shengfang Liao

Submitted to the Department of Aeronautics and Astronautics
on August 11, 2000, in partial fulfillment of the
requirements for the degree of
Doctor of Philosophy

## Abstract

This thesis presents an investigation of the stability of axial compression systems when external disturbances are introduced. Aerodynamic stability is considered from a nonlinear perspective. From this perspective, the goal is to enhance the ability of compressor systems to remain stable in the face of external disturbances.

Experiments were conducted on a low-speed three-stage axial compressor. Instead of achieving extension of linearly stable operating range, this research is focused on the followings: (1). The operability of the compressor, the ability of maintaining the stable operations of the compressor near the operating points in the presence of the external disturbances, was considered. The concept of domain of attraction was adopted to characterize the operability or the disturbance rejection of the compressor. An experimental method was developed to generate disturbances and measure the approximate domain of attraction in terms of the zeroth and first mode flow perturbations. (2). Improvement of the approximate domain of attraction was demonstrated by active control. Both the constant gain control which has been used in many range extension tests and the sliding mode control which is model based, doubles the maximum allowable amplitudes of the zeroth and first mode flow perturbations. (3). The downstream bleed was chosen as the actuation, which is easy to implement and more practical. The number of the bleed valves was chosen to be four to compromise the goal of reducing the number of actuators and the requirement of achieving a satisfactory control effectiveness. (4). The domain of attraction was also examined under inlet distortions. The nonlinear simulation showed that the disturbance rejection of the compressor with background distorted flow was improved by active control.

Thesis Supervisor: James D. Paduano
Title: Principal Research Engineer

# ACKNOWLEDGMENTS

I would like to thank my thesis advisor, Dr. James D. Paduano, for his guidance, expertise and patience throughout this research project. I also thank my thesis committee members: Prof. Alan H. Epstein, Dr. Choon S. Tan and Prof. Eric Feron for their continuous interests and supports.

Jimmy Letendre, Victor Dubrowski and Bill Ames did all the necessary work on the rig and helped me in every emergent situation. Their assistance is greatly appreciated. Jon Protz and Duc Vo helped me get my experiments run and were always willing to answer my frequent questions.

A lot of discussions with Yifang Gong, Zolti Spakovsky, Yong Wang and Dan Fontain are very valuable. Especially, Yifang helped me a lot through these years. I would like to thank them and all other GTL students and professors. Also I thank Lori Martinez and Holly Anderson for their kindness and help.

The financial support by AFSOR Grant #F49620-95-1-0409 managed by Dr. Marc Jacobs, is gratefully acknowledged.

I am also indebted to Prof Jingyi Chen (Institute of Engineering Thermophysics, China) and Prof Liping Xu (University of Cambridge, United King) for their continuous and encouraging support.

I would like to express my gratitude to my family, especially my parents, for their love and support. Finally, I would like to thank my wife, Hongmei, who made everything possible.

# CONTENTS

# List of Figures

# List of Tables

# NOMENCLATURE

## Roman

| | |
|---|---|
| $A_n$ | coefficient of the general solution for linearized 2D duct flow |
| $a, b$ | triangular Fourier coefficients of mass flow |
| $B$ | Greitzer's B parameter |
| $B_n, C_n$ | coefficient of the general solution for linearized 2D duct flow |
| $E, A, T$ | |
| $S, \mathcal{G}, J$ | coefficients for state space model |
| $\mathcal{F}$ | actuation shape matrix |
| $F$ | discrete Fourier transform matrix |
| $j$ | $\sqrt{-1}$ |
| $K$ | control gain |
| $K_t$ | throttle coefficient |
| $L$ | unsteady losses |
| $l_I$ | upstream duct length |
| $l_e$ | downstream duct length |
| $l_b$ | distance between compressor exit and bleed |
| $l_c$ | overall length of compressor |
| $n$ | mode number |
| $R$ | rotor reaction of compressor |
| $r$ | mean radius of compressor |

| | |
|---|---|
| $U$ | rotating speed at mean radius |
| $u$ | actuation |
| $x$ | non-dimensional axial coordinate |

## Greek

| | |
|---|---|
| $\beta$ | relative angle between inlet distortion and disturbance |
| $\Phi, \bar{\phi}$ | mean mass flow |
| $\phi$ | non-dimensional mass flow |
| $\phi_e$ | equilibrium mass flow |
| $\mu$ | compressor fluid inertia |
| $\lambda$ | rotor fluid inertia |
| $\xi$ | non-dimensional time |
| $\theta$ | angle around annulus |
| $\rho$ | air density |
| $\psi$ | non-dimensional pressure |
| $\psi_c$ | actual compressor characteristic |
| $\psi_i$ | ideal compressor characteristic |
| $\omega$ | frequency |
| $\tau$ | time constant for unsteady losses |
| $\gamma$ | bleed valve opening |

## Subscripts

| | |
|---|---|
| $b$ | bleed |
| $d$ | downstream |
| $dist$ | inlet distortion |

| | |
|---|---|
| $e$ | compressor exit or equilibrium |
| $1, 2, 3, ...$ | station number |
| $r$ | rotor |
| $s$ | stator |
| $ss$ | steady state |
| $t$ | total pressure, temperature, etc |
| $T$ | throttle |
| $u$ | upstream |

# CHAPTER 1

# INTRODUCTION

The performance of the compressor in a gas turbine engine is limited by instabilities that occur when the mass flow is reduced. The instabilities mainly include two kinds of aerodynamic phenomena, known as surge and rotating stall. A physical explanation of rotating propagation of stall cell were first presented by Emmons [1]. Extensive researches have been ever done in the past three decades to elucidate the physical mechanisms associated with these phenomena, and more recently to establish methods for active stabilization of these instabilities. A brief summary of the related research work is presented in this chapter. This thesis will concentrate on the characterization and active control of nonlinear stability of the compression system. More extensive information of this subject can be found in Greitzer's review [2].

## 1.1 Compressor Stabilities And Modeling

There are two main aerodynamic instabilities in compressors (Figure 1-1). Rotating stall is a circumferentially non-uniform flow characterized by a reduced flow region in the compressor annulus. This reduced flow region (stall cell) rotates at a fraction of rotor speed (around 20% - 60%). Surge is an axial flow oscillation throughout the whole compression system with a lower frequency. Both phenomena cause many harmful effects on the compression system. For example, surge may suck hot gas

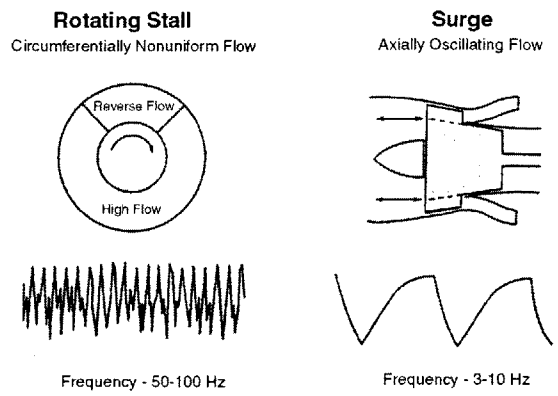


**Figure 1-1:** Rotating Stall And Surge (from [2])

from the combustor to the compressor area, which is not designed for running at high temperature. Rotating stall may stress compressor blades. They are usually not acceptable in real engine applications.

Typical compressor performance maps are shown in Figure 1-2. The left figure

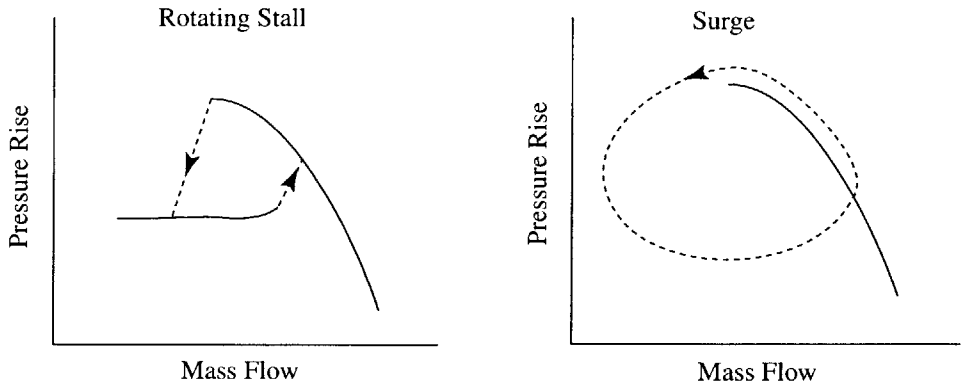


**Figure 1-2:** Compressor Performances With Instabilities

represents the case of a compressor entering rotating stall. When the mass flow is reduced to some critical value, rotating stall occurs. The pressure rise drops to a lower value. Although rotating stall is an unsteady phenomenon, the corresponding point on the compressor map is represented by a steady point. If the throttle is opened to recover the stable operating point after rotating stall is developed, it may have to be opened beyond the throttle setting at which rotating stall occurs, as shown in the figure. This phenomenon is called hysteresis. Beyond the destructive effects of

rotating stall, the significant pressure drop and recovery hysteresis are the other two important reasons why rotating stall must be avoided or prevented. The right plot in Figure 1-2 shows surge. Even on the compressor map, there is no steady operating point once surge occurs. So it is impossible to achieve the design pressure rise and mass flow required for the gas turbine.

To understand the mechanism of onset of rotating stall, stall inception has been intensively investigated. There are two main types of stall inception. One is so-called modal inception, which is a rotating wave occurring several revolutions prior to fully developed rotating stall, as observed in low speed compressor by McDougall [3] and Garnier [4]. The other type of stall inception was reported by Day [5]. This type of stall inception is characterized as short length scale, sometimes referred to as pips or spikes, which are regions of low mass flow over only a few blade passages. These spikes usually rotate faster than modal waves, at up to 70% of rotor speed. For our purpose, only modal wave stall inception will be studied.

While many experimental results were presented to characterize these compressor instabilities, several modeling efforts were also undertaken to understand, predict and describe these phenomena. Emmons [1] constructed a linear surge model by considering the oscillation to be a Helmholtz resonator which includes the upstream duct, compressor and downstream duct. Greitzer [6] extended this model to a nonlinear one, accompanying simulation and experimental data on a three stage compressor. In his paper, Greitzer also proposed a non-dimensional B parameter which characterizes whether surge or rotating stall will occur in a particular compressor. Later, Moore [7] proposed a 2D theory and described many features of rotating stall, such as stall rotating speed, etc. Moore and Greitzer [18] combined their models together and constructed a more complete model to capture the main features of surge and rotating stall. We refer to this model as the Moore-Greitzer model. The Moore-Greitzer model is a 2D incompressible inviscid model which accounts for axial and circumferential flow and neglects radial flow (valid for high hub-to-tip ratio compressors). The compressor is treated as a semi-actuator-disk which accounts for pressure

rise across the compressor and a first order unsteady pressure rise characteristic. The Moore-Greitzer model has been confirmed by many experiments [3, 4, 23].

Extensions to the Moore-Greitzer model were made to account for compressibility effects [8, 9]. Weigl [10] conducted investigations on a single stage transonic compressor (NASA Stage 35) experimentally. The comparisons of theoretical and measured eigenvalues showed that the dominant low frequency zeroth and first harmonic modes matched fairly well. Chi [35] did even more detailed modeling and was able to capture more dynamics theoretically.

In addition, many efforts were undertaken to model the three-dimensional nature of some rotating stall inception events, like part-span stall and "spike" stall inception. These events can not be described by a two-dimensional model. Hoying et al [24] conducted CFD calculations on a single rotor blade row and found that the tip vortex can cause local flow field breakdown and subsequently cause rotating stall. Gong [25] proposed a three-dimensional computational model and was able to simulate short wavelength stall inception.

## 1.2 Active Control And Range Extension

A compelling motivation for investigating surge and rotating stall is to enhance compressor performance which might be degraded by these instabilities. In contrast to the traditional method for avoiding these instabilities, Epstein et al [11] proposed that feedback control technology could be used to provide additional damping to the modal disturbances which otherwise would grow into fully developed rotating stall or surge. Figure 1-3 shows the idea of the effect of active control. In the figure, Point A represents a conventional operating point with active control, while Point B represents an actively stabilized operating point which is normally unstable without control. Consequently the surge line of this compressor is extended to a lower mass flow and the stable operating range is enlarged. Active control might make it possible for a compressor to run at a lower mass flow but higher pressure rise point.

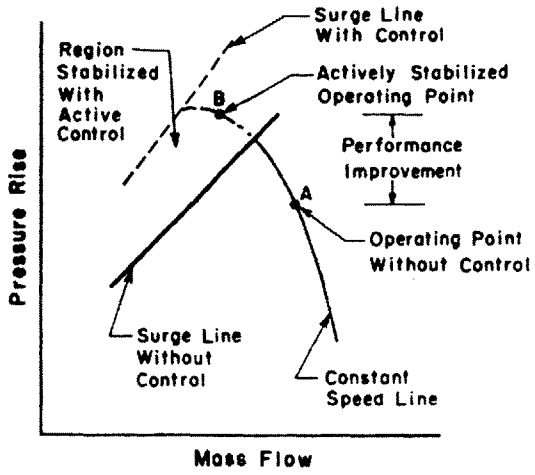


**Figure 1-3:** The Effect of Active Control on Compressor Performance (from [11])

Active control technology was applied to surge first by Ffowcs Williams and Huang [12] who used plenum pressure measurements and a loud speaker mounted in the plenum to stabilize surge. Later, several authors succeeded in suppressing surge. Simon et al [13] analyzed the effectiveness of various sensing and actuation configurations based on a linearized surge model and linear control theory.

In the area of rotating stall control, Paduano [19] was the first to implement a constant gain harmonic controller on a single stage compressor using an array of 12 IGV actuators. A significant range extension was achieved by controlling the first three spatial modes. A complete forced response procedure was also built to identify the system dynamics experimentally, which gave the first experimental fittings of the parameters in the Moore-Greitzer model and therefore verified it. Haynes [20] was able to implement this control configuration successfully into a three stage low speed compressor. Van Schalkwyk [15] demonstrated active control with inlet distortion on the same experimental rig studied by Haynes.

Weigl [10] demonstrated range extension on a single stage transonic compressor at 70% speed with similar constant gain control. However, constant gain control law failed at 100% speed. An $H_\infty$ controller was then designed and successfully achieved range extension at 100% speed. Chi [35] then found that the constant gain controller

was still effective at 100% speed if the acoustic mode was filtered out. Spakovszky et al [36] were able to extend the operating range on the same rig with radial and circumferential distortion.

This approach is based on the assumption of long wavelength rotating stall inception. Actuation waves are generated in response of detected flow perturbation to suppress those perturbations. In order to generate these actuation waves, many actuators are needed to be installed around the compressor annulus. Also the approach is completely based on the linear stability theory, which means that relatively large external disturbances are not considered. In real engines, these large amplitude disturbances may be very important and affect the stability of the compressors.

## 1.3 Nonlinear Stability and Active Control of Operability

As many demonstrations of range extension were successfully achieved, more researches were focused on making active control more practical. Reducing the number of actuators and the required bandwidth is one of the most compelling goals. This motivated a totally different approach of active control. Instead of range extension, this approach is focused on the "operability" of the peak of the compressor characteristic. Here the "operability" means that the goal of active control is maintaining the operation of the compressor near the peak without losing stability in the face of external disturbances.

This approach was first motivated by the theoretical argument that a one-dimensional plenum bleed can be used to modify the local stability property (bifurcation) near the peak [41]. This theory was based on the three-state simplified Moore-Greitzer model derived by McCaughan [26] in which a rigorous bifurcation study was conducted. Physically, the control idea based on the bifurcation theory is to eliminate the hysteresis phenomena of rotating stall and therefore enhance the compressor op-

erability. Eveker et al [29, 30] were able to demonstrate the elimination of rotating stall hysteresis by a one dimensional throttle control on low speed and high speed compressors. D'Andrea et al used pulsed air injection to demonstrate range extension and elimination of hysteresis. Yeung [32] used both axisymmetric bleed and air injection to eliminate the hysteresis loop and also show the importance of rate limit of actuators.

Although there are several experiments targeting eliminating the stall hysteresis, it is generally difficult to do that in a real engine. It is also not necessary to limit the number of actuator to be one. Further research is motivated to further explore the concept of operability. This approach does not provide quantitatively the disturbance tolerance of the compression system either, even though the control targets rejecting disturbances.

Other nonlinear analysis and control are listed briefly as follows. Mansoux [27] conducted a theoretical nonlinear analysis of surge and rotating stall based on Lyapunov function. Setiawan [28] then tried a distortion tolerance characterization by numerical simualtions. Protz [17] demonstrated the measurements of a controller's distortion tolerance.

## 1.4 Scope And Outline Of Thesis

As mentioned above, many demonstrations of active control of compressor instabilities have been done. More practical implementations need to be considered. For instance, complexity, cost and reliability are all important for real industrial operations. Type and number of actuators are major considerations. In this context, IGVs are not attractive for a variety of reasons. Many blades must be actuated to accurately generate the required feedback. They are also ineffective for surge mode suppression. Jet injection needs a very complicated high pressure air supply or recirculation which is very difficult and costly to implement on real engines. In this thesis, downstream bleeds will be used, because they are relatively easy to implement.

In addition, bleed valves already exist in modern aircraft engines for other purposes. It may be possible to better use existing bleed ports with high-speed actuations to generate some useful control schemes. We will not go to the extreme of using just one actuator, but will reduce the number of actuators.

Rather than range extension, the concept of operability is adopted. In the original stall margin experiments, the linearly stable operating range was measured experimentally. A safety margin was also set to account for possible disturbances. The idea of range extension targets extending this linearly stable operating range by active control and therefore makes it possible to run compressors at higher pressure ratio with the same stall margin. To achieve range extension, we need to stabilize unstable operating points, which may require more number and higher bandwidth of actuators. In this thesis, instead of trying to stabilize those unstable operating points, the existing stable operating points will be made "more stable" in the sense of nonlinear stability. If those originally stable operating points can resist relatively larger disturbances, the compressor may be safely run at lower mass flows without worrying about instabilities induced by large disturbances. The compressor can then run near the boundary of linear stability. In this perspective, the operable range of a compressor is extended. This thesis will explore this idea more thoroughly and implement it experimentally.

The main objective of this thesis is to implement a practical two-dimensional actuation scheme for improving compressor disturbance rejection (robustness of stability) in a realistically scaled multistage compressor rig. In order to achieve this, the following sub goals are necessary:

- Construct and validate a model of non-axisymmetric downstream bleed. Test the control effectiveness of downstream bleed.
- Characterize the nonlinear stability of operating points by nonlinear simulations and experiments.
- Develop an experimental method to generate disturbance and measure the ap-

proximate domain of attraction (characterization of nonlinear stability).

- Demonstrate the enhancement of robustness of stability by actively actuating the downstream bleed valves.
- Investigate the approximate domain of attraction and active control with inlet distortion by numerical simulations

The thesis is organized as follows. Chapter 2 introduces the experimental rig, the GTL three stage low speed compressor, and describes the instrumentation. Chapter 3 contructs and verifies the downstream bleed model. Chapter 4 tests the ability of the downstream bleed valves to extend the compressor operating range with constant gain control. Chapter 5 discusses the concept of nonlinear stability. The concept of domain of attraction is introduced to measure how robust an operating point is to external disturbances. The experimental measurements of approximate domain of attraction is also performed. Active control is applied to the compression system to improve the nonlinear stability. Chapter 6 explores the domain of attraction with inlet distortion.

# CHAPTER 2

# EXPERIMENT SETUP

All experiments were conducted on a low speed three stage compressor. This compressor facility was also used by Haynes [20], Van Schalkwyk [15] and Fahim [34]. In this chapter, I will give an introduction to the rig and associate instrumentation.

## 2.1 MIT Low Speed Compression System

The test rig is a low speed, three stage compressor originally used to study blading concepts for the Pratt and Whitney JT9D program. It was used to study rotating stall and active control at GTL by Haynes [20], Van Schalkwyk [15], Vo [16], Protz [17] and Fahim [34]. More information about this rig can be found in their theses. Table 2.1 summarizes the main design parameters of the rig.

**Table 2.1:** Parameters of Compressor Rig

| | | | |
|---|---|---|---|
| Tip Radius (in) | 12.000 | Pressure Rise at peak (psig) | 1.081 |
| Hub Radius (in) | 10.558 | Flow Velocity at peak (ft/s) | 125.44 |
| Mean Radius (in) | 11.279 | Mass Flow at peak (scfm) | 5341.2208 |
| Duct Area ($in^2$) | 102.192 | Design Reaction | 0.75 |
| US Duct Length (in) | 33.750 | Plenum Volume ($ft^3$) | 341.264 |
| DS Duct Length (in) | 17.250 | Compressor Length (in) | 26.250 |

A schematic of the three stage compressor rig is shown in Figure 2-1. The com-

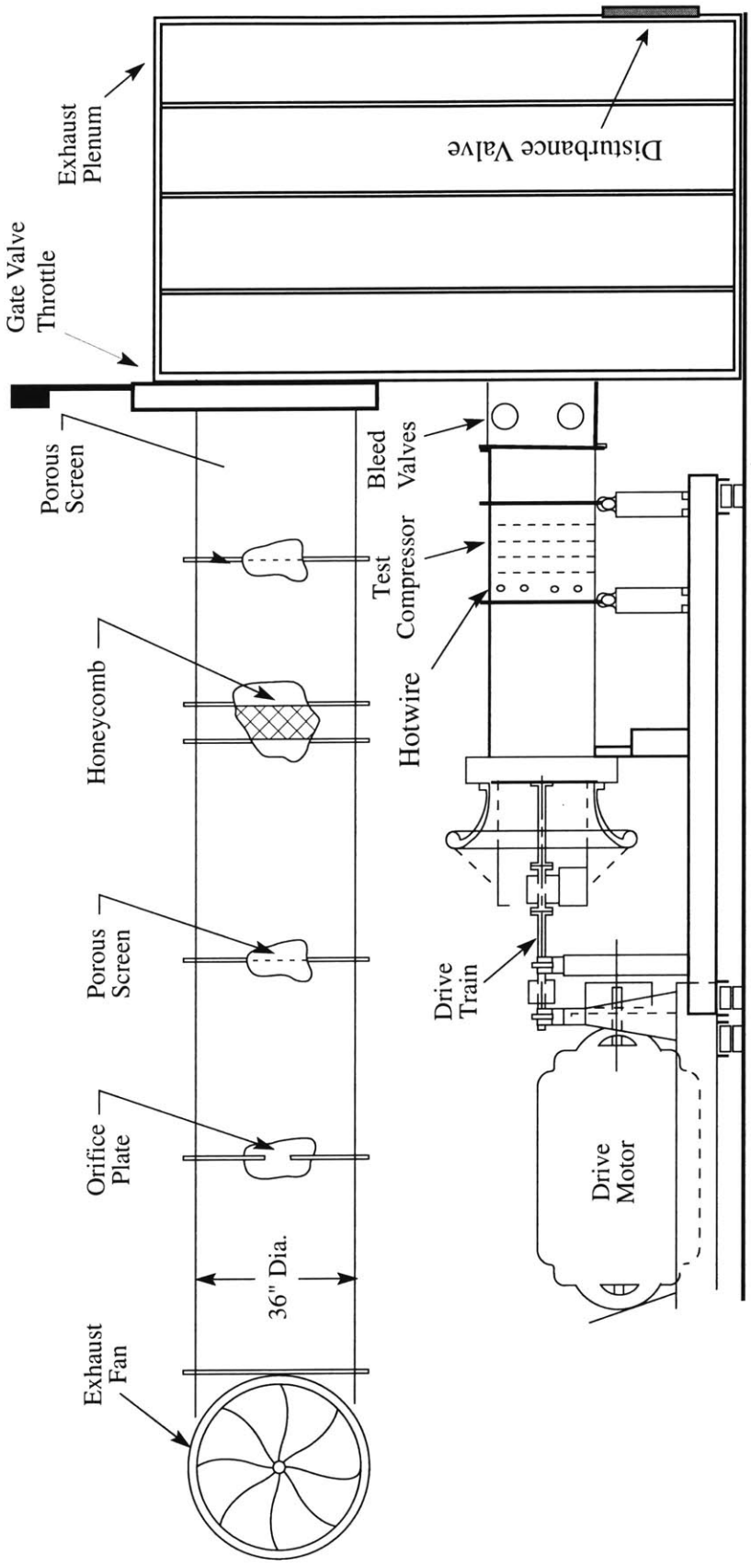


**Figure 2-1:** Schematic of Three Stage Compressor Test Rig

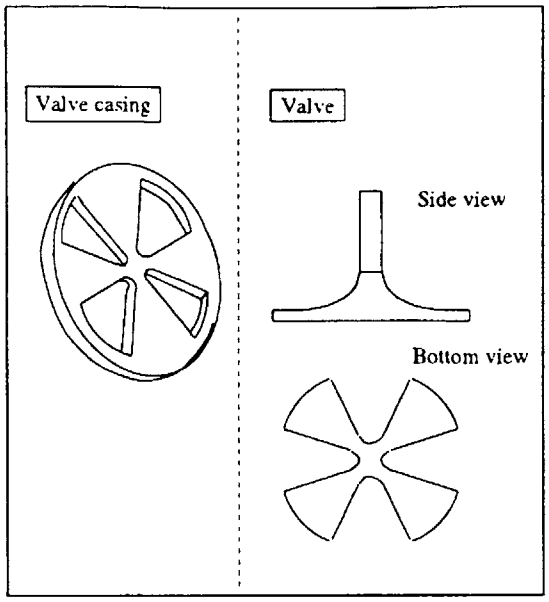


**Figure 2-2:** Schematic of Downstream Bleed Valve (from Figure 2-7 of [34])

pressor is a high hub-to-tip ratio (0.88) three stage axial compressor with an operating speed of 2400 rpm. The compressor exhausts into a large downstream plenum added by Protz [17]. The original purpose of adding this plenum was to allow the compression system to surge to investigate the control of the system with high B parameter. The internal volume of the plenum is about 340 cubic feet. The B parameter is approximately 0.9 at 2400 RPM. We adopted this plenum setting to investigate robustness of stability. We are not only interested in rotating stall behavior, but also zeroth mode (surge) behavior. So a high B system fits our needs.

The actuators chosen for our experiments are downstream bleed valves. There are four bleed valves evenly distributed around the annulus (Fahim [34]). Figure 2-2 shows a schematic of the downstream bleed valve. The valves are driven by servo motors. Because of the symmetry of the valves and valve casings, turning angle greater than 45 degree will cause repeating patterns of relative positions of the valves and casings. Therefore the turning range of the valves is set from 0 to 45 degree. The frequency response of these valves is shown in Figure 2-3. The maximum bleed mass flow when running at the peak of compressor characteristics is about 15% of the peak mass flow. The valves also have a rate limit of 450°/s according to Fahim's measurement [34].

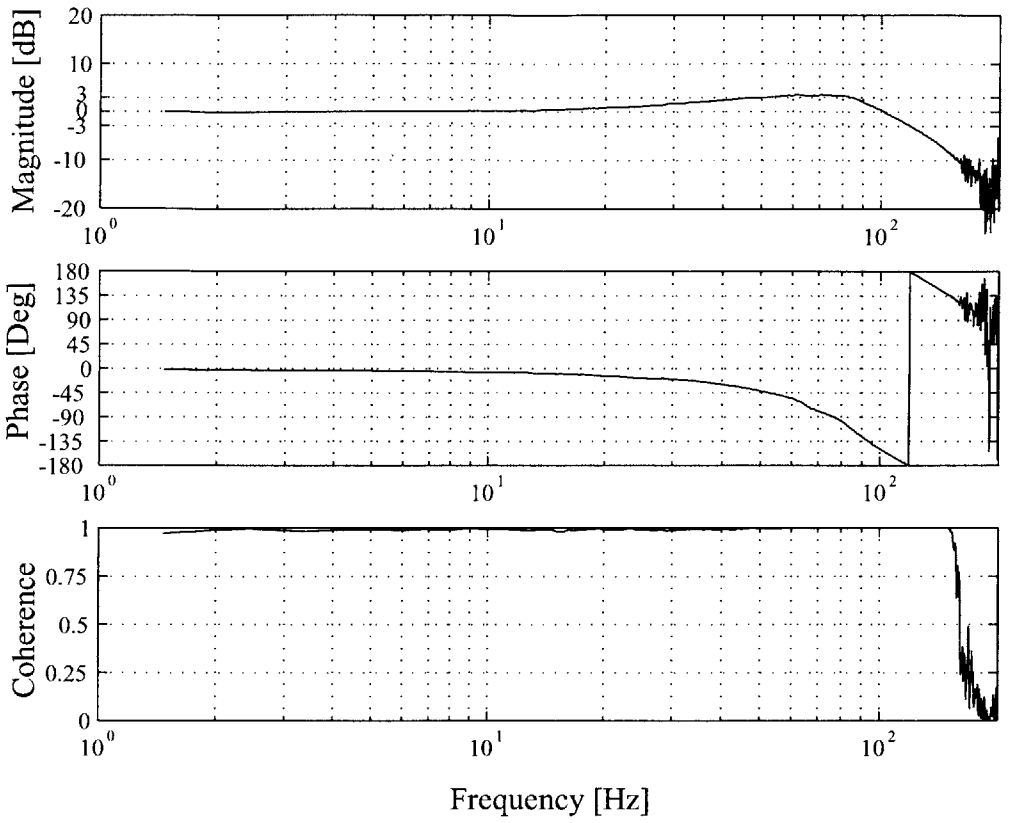


**Figure 2-3:** Frequency Response of a Single Bleed Valve

The leakage of the valves was measured to be less than 1% of the total mass flow capacity of the valves. Calibrations also shows that the mass flow through the valve is quite linear with the opening angle under constant pressure [34]. This means that the discharge coefficient can be assumed constant, which we also assume later in Chapter 3. The bleed valves are installed downstream of the compressor at a distance of approximately one compressor mean radius, due to practical considerations. The penalty is that this distance causes exponential decay of the potential upstream effects of the actuation, which will be shown in the forced responses of Chapter 3.

## 2.2 Instrumentation

Steady sensors are installed on the rig to measure local static and total pressures around the annulus and in the plenum. Hot wires are also installed around the

annulus to measure local velocities. An unsteady pressure transducer is installed in the plenum. In the following subsections, a brief summary of the instrumentation is given. More details can be found in the theses of previous students [14, 20, 15, 16, 17].

Figure 2-4 shows the sensor locations on the rig.

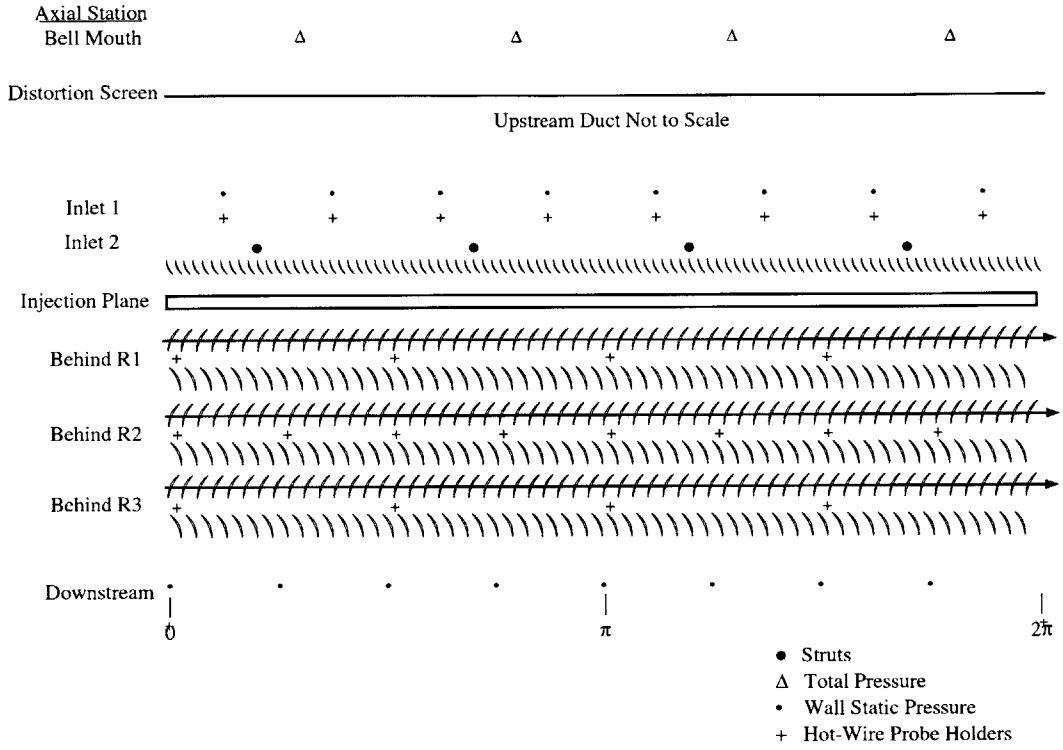


**Figure 2-4:** Instrumentation Scheme of Three Stage Compressor

### 2.2.1 Steady Measurement

Steady state pressure at various locations in the rig is measured by a Scanivalve SSS-48C multi-port pressure sensing system. The SSS-48C is controlled and read by a Scanivalve SDIU-MK3 interface which is connected to the control computer. The Scanivalve was configured with a stepping rate of 3 ports per second to allow the pressure to settle before reading. The pressure sensor was calibrated by a MKS Baratron 170M-6C unit. The accuracy of steady pressure measurement is around +/-0.005 psig or about 1.7% of peak pressure rise.

The steady state flow coefficient of the compressor was calculated from the total and static pressure at the bellmouth, using calibration information from [20]. More details about this approach are given in Haynes [20].

The ambient temperature is measured by a mercury thermometer to calibrate the air density. The temperatures of the bearings were monitored with Omega type K thermocouples.

### 2.2.2 Unsteady Measurements

The unsteady measurements include pressure in the plenum and flow measurement by hot wires. The unsteady pressure in the plenum was measured by a Druck 820 strain-gauge type pressure probe which measures pressures up to 2.5 psi. The pressure probe has a natural frequency of 28 kHz.

There are eight hot wires evenly distributed around the annulus at 0.6 mean rotor radii upstream of the first rotor. Each hot wire anemometer consists of a Dantec 56C17 bridge and a Dantec 55-P11 hot wire probe which has a 20 $\mu$m tungsten wire of about 1.2 mm in length. The hot wires were placed at the mid-span of the annulus, which is the most effective location for detecting stall precursors as reported by Haynes [20]. The hot wires have bandwidths of 50 kHz. The hot wire signals were filtered with fourth order Bessel filters before they were discretized by an A/D converter. The filter cutoff frequency was set to 250 Hz, which is low enough to give about 80 dB attenuation of rotor blade passing frequency. The hot wires were calibrated over the range of 0 m/s to 50m/s by steady measurements every running day. The anemometer output voltage (E) in volts is related to the velocity (V) by King's Law:

$$E^2 = A_0 + A_1 V^m \tag{2.1}$$

where $A_0$, $A_1$, $m$ are parameters obtained through calibration.

### 2.2.3 Data Acquisition

Data acquisition was done by two computers. An Industry Pentium-133 Computer was used to acquire and store unsteady data. This computer stored 16 seconds of unsteady data during each run. An Analogic HSDAS-16 A/D converter is used to sample the unsteady signals. A DASMUX-64 multiplexer was used to multiplex 30 sensor signals to the 16 channels of the HSDAS-16. Each of the 32 channels was sampled at a rate of 1 kHz.

The steady signals were acquired by another PC connected to the Scanivalve SDIU-MKS3 interface. There is also a RS-232 serial connection between these two PCs to synchronize the data acquisition during calibration.

Finally, there is also an eight-channel Datel D/A board to provide outputs to an oscilloscope or spectralanalyzer for online monitoring.

### 2.2.4 Motion Control of Servo Motors

The servo motors used to drive the bleed valves are Pacific Scientific 4VM62-220-1 low inertia DC motors. The DMC 430 digital PID servo motion controllers are used to control these motors. The controllers use shaft encoders to measure motor position. The resolution is 4096 counts per revolution or 11.3778 counts per degree.

## 2.3 Plenum Disturbance Generation

A plenum disturbance valve was built to enable generation of downstream disturbances, to investigate the disturbance tolerance of an operating point. This section describes the plenum disturbance valve and its characteristics. Finally, a filtering technique for processing the stall inception data is introduced.

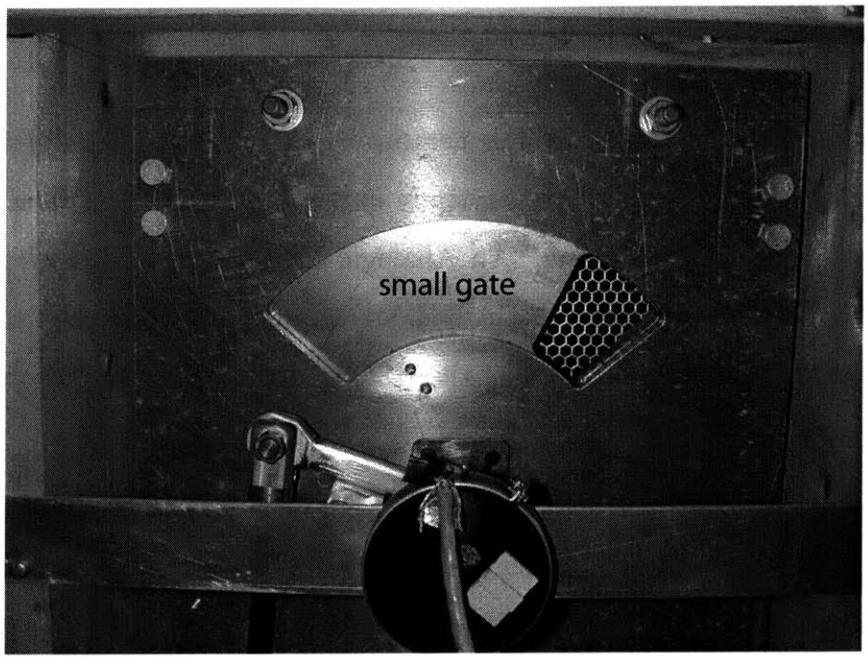


**Figure 2-5:** Schematic of Plenum Disturbance Valve

### 2.3.1 Plenum Disturbance Valve

A small gate was installed on the wall of the plenum. The gate can either open or close, driven by a piston connected to a high pressure source. A potentiometer was attached to the axis of the rotating gate to measure its angular position in real time. Figure 2-5 shows a schematic of the plenum disturbance valve. Four opening settings can be achieved. The closing speed can be tuned by regulating the pressure of a high pressure source.

The transient of the closing action of the plenum disturbance valve is shown in Figure 2-6. From the figure, the transient of the closing action lasts about 0.005 seconds which is much faster than the zeroth mode dynamics of the compression system. So the closing action finishes much earlier than the system transient reacting to it. The system transient can then be considered to be free.

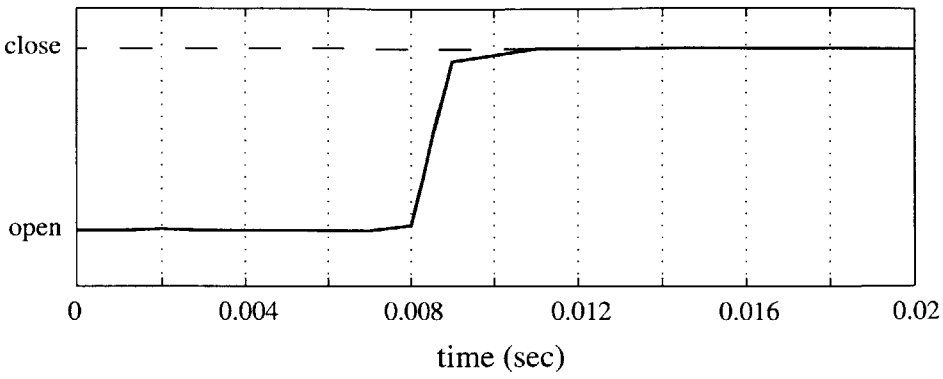


**Figure 2-6:** Transient of Closing the Plenum Disturbance Valve

### 2.3.2 Data Extraction And Filtering

Plenum disturbances also induce first spatial mode disturbances when the mass flow transient value goes below the stalling mass flow. Due to random excitation of the first mode, the system may either remain stable after it is disturbed, or go into rotating stall. We wish to determine the largest disturbances for which the system remains stability by applying the plenum perturbations of various amplitudes. To determine the size of the disturbances, it is necessary to extract magnitude information from the experimental data. Because the noise level is relatively high on this rig, the disturbances are hard to distinguish when they are small. Also, any circumferential non-uniformities due to hot wire measurement can add more uncertainty to the data. Therefore a filtering algorithm was developed to process the experimental data.

The noise in the first mode estimate comes from two sources: one is the flow noise in the measurement; the other one is circumferential non-uniformity due to drift of the hot wire calibration. These two may also mix together. Merely filtering the signals of each hot wire by some band-pass filter is not the best way, because this method filters only the electrical noise of each hot wire. Instead, we construct a more efficient filter by using the rotating nature of the nth spatial harmonic. The filter actually band passes only those signal contents rotating at frequencies near the nth mode rotating frequency. The details of this filter can be found in Appendix A.

Figure 2-7 shows an example of the filter performance. The dashed lines are

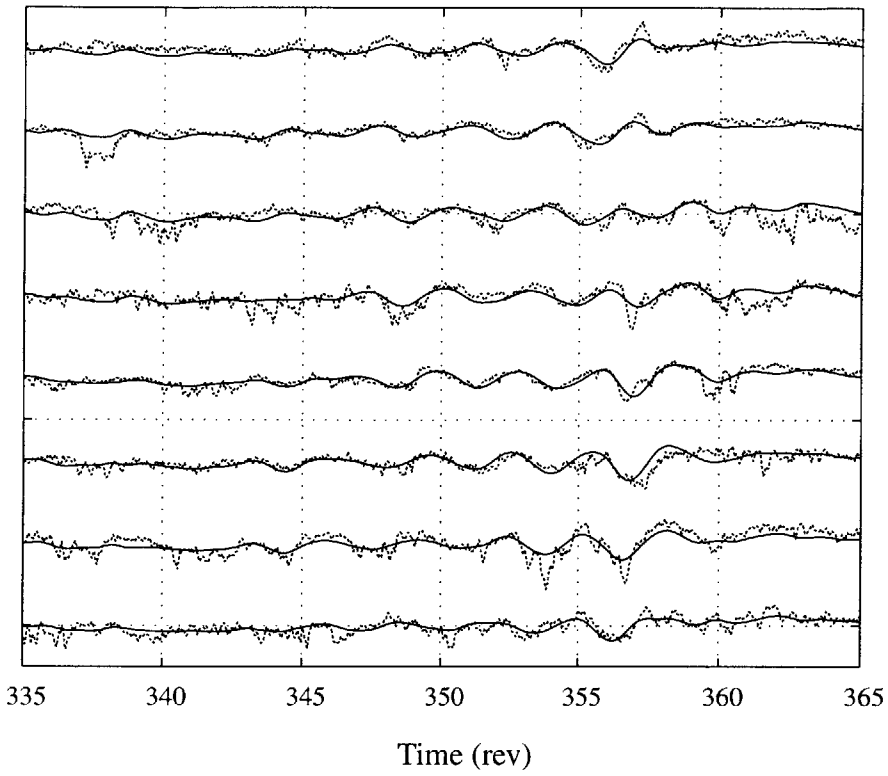


**Figure 2-7:** The Original And Filtered Hot Wire Traces (dashed — original, solid — filtered)

the original hot wire traces, while the solid lines are the filtered traces. We see that any independent bumps of an individual hot wire signal are filtered very well, because these small bumps are not rotating around the annulus. Filters applied to any individual hot wire signal would not distinguish these independent bumps from real physical signals because no knowledge of the adjacent hot wires would be available to the filter. The filter employed here, on the other hand, preserves the rotating waves and eliminates non-rotating or stationary (hot wire drift induced) waves.

# Chapter 3

# Modeling Distributed Bleed Actuation

In this chapter, a downstream bleed model will be constructed. Because there are only four actuators used which can not generate a continuous wave accurately, the model is derive by considering discrete actuation around the annulus. The model will be incorporated into a full compression system model which is based on the Moore-Greitzer [18] model framework. A multi-input multi-output (MIMO) state-space representation will then be derived. Finally, forced response data will be compared with theoretical model predictions.

## 3.1 Assumptions

In this section, we summarize the main modeling assumptions which were introduced by Moore and Greitzer [18]. These assumption will be adopted in our downstream bleed model. They are:

- The flow is incompressible. This assumption limits the model validity to low speed compressors. In our experiment setup, the mean blade Mach number is about 0.2 and the Mach number based on rotating speed of modal waves is less than 0.1.

- The flow is two dimensional. This assumption implies that flow in the radial direction is neglected, which is a good approximation for high hub-to-tip ratio compressor. The hub-to-tip ratio of the MIT low speed compressor is 0.88.

- The duct flow is inviscid. Haynes [20, 21] found that in this compressor, the Reynolds number seen by the $n$ th spatial harmonic is on the order of $6.27 \times 10^5/n$, which means that the first several modes are dominated by inertial effects. So the viscous effects can be neglected in the ducts.

- The compressor is modeled as a semi-actuator disk. This assumption allows us to model compressor pressure rise without considering the detailed flows through the blade rows.

- The flows in the upstream and downstream ducts are linearized, assuming that the quadratic terms in the flow fields are much smaller than the first-order terms. Hynes and Greitzer [22] and Lavrich [14] showed that this assumption is valid even for strongly distorted flow.

## 3.2 Notation

The compression system is simplified into the following components: inlet distortion screen, upstream duct, compressor, downstream duct, bleed valves, plenum and throttle. The schematic of the system is shown as Figure 3-1.

In this section, the variables and parameters used in the system model will be listed and explained. Whenever possible, we use the same nomenclature as Moore and Greitzer.

The system equations are non-dimensionalized with respect to the following reference parameters:

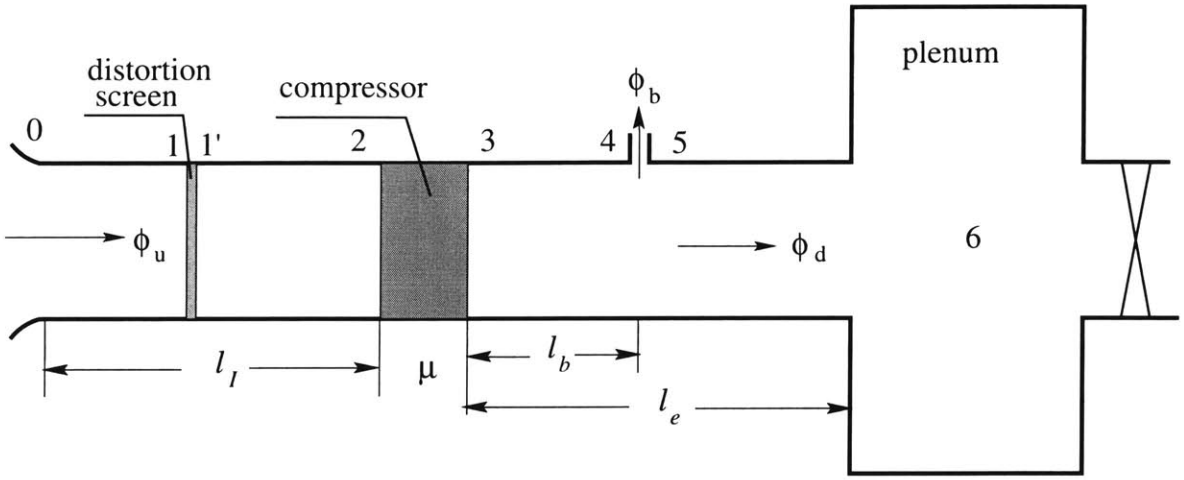


**Figure 3-1:** Schematic of Compression System

$r$ mean radius of compressor,

$U$ rotating speed at mean radius,

$\rho$ ambient air density.

The non-dimensionalizations are done as follows:

$$\frac{\text{length}}{r}, \frac{\text{velocity}}{U}, \frac{\text{pressure}}{\rho U^2}, \frac{\text{time}}{r/U}.$$

The independent variables are:

$\theta$ angle around annulus. Positive $\theta$ is in the direction of rotor rotation;

$\xi$ non-dimensional time;

$x$ non-dimensional axial coordinate. Positive values are in the flow direction. The origin is located at the compressor face.

The flow of the system is described by the following quantities. These quantities are all non-dimensionalized with the reference parameters mentioned above.

$\phi(\theta, \xi, x)$ local flow coefficient (axial velocity/$U$)

$\psi(\theta, \xi, x)$ local static pressure

$\psi_t(\theta, \xi, x)$ local total pressure

$\phi_b(\theta, \xi)$ bleed flow coefficient

Several other parameters must be introduced to describe the behavior of the semi-actuator-disk compressor and throttle. Compression system dimensions are marked in the schematic (Figure 3-1). This figure serves as the definition for the corresponding non-dimensional parameters.

$\psi_c(\phi)$ compressor total-to-static pressure rise,

$\psi_i(\phi)$ ideal compressor characteristics,

$\Phi_T(\psi)$ throttle characteristics ($= \sqrt{\frac{2}{K_t}\psi}$),

$\Psi_{dist}(\theta, \phi)$ total pressure inlet distortion,

$L_r(\theta, \xi)$ unsteady loss in rotor,

$L_s(\theta, \xi)$ unsteady loss in stator,

$L_{ss}(\theta, \xi)$ difference between ideal and actual pressure rise across compressor,

$R$ rotor reaction of compressor,

$B$ Greitzer's B parameter,

$\lambda$ rotor fluid inertia,

$\mu$ compressor fluid inertia.

## 3.3 Downstream Bleed Model

This derivation of our model of distributed bleed actuation includes a bleed actuator model, an account of the distributed nature of the actuation and the response of downstream duct flow. A more general inter-stage bleed model is included in Appendix B. Detailed Moore-Greitzer model derivation will not be repeated here.

### 3.3.1 Actuator Disk Model For Bleed

The location of the distributed bleed valves is modeled as an actuator-disk in which only mass and momentum conservation are considered upstream and downstream of the bleed valve. This approach neglects the flow details and viscous effects in the valve region. By applying mass conservation, we have that

$$\phi_4 = \phi_5 + \phi_b \tag{3.1}$$

By applying Bernoulli's equation, we have the following momentum relationship

$$\psi_4 + \frac{1}{2}\phi_4^2 = \psi_5 + \frac{1}{2}\phi_5^2. \tag{3.2}$$

### 3.3.2 Downstream Duct Flow

The flow field in the downstream duct is linearized as mentioned before. The linearization implies that the potential and vortical parts of the flow field are decoupled. The validity of flow field linearization was addressed and proven by many researchers [18, 22]. We will start with a general solution for linearized two dimensional duct flow used by Longley [23].

The flow field quantities are represented as a mean part plus a disturbance part

$$\phi(\theta, \xi, x) = \bar{\phi}(\xi) + \delta\phi(\theta, \xi, x),$$

and the disturbance term is decomposed as follows:

$$\delta\phi = \sum_{n=-\infty}^{\infty} \hat{\phi}_n e^{jn\theta+j\omega\xi}.$$

The general solution for a linearized 2D annulus duct flow can be written as

$$\begin{pmatrix} \delta\phi \\ \delta v/U \\ \delta\psi \\ \delta\psi_t \end{pmatrix} = \sum_n \begin{pmatrix} 1 & 1 & 1 \\ \dfrac{\omega}{n\bar{\phi}} & -\dfrac{j|n|}{n} & \dfrac{j|n|}{n} \\ 0 & \dfrac{j\omega}{|n|} - \bar{\phi} & -(\dfrac{j\omega}{|n|} + \bar{\phi}) \\ \bar{\phi} & \dfrac{j\omega}{|n|} & -\dfrac{j\omega}{|n|} \end{pmatrix} \begin{pmatrix} A_n e^{jn\theta - j\omega x/\bar{\phi}+j\omega\xi} \\ B_n e^{jn\theta-|n|x+j\omega\xi} \\ C_n e^{jn\theta+|n|x+j\omega\xi} \end{pmatrix} \tag{3.3}$$

where $e^{jn\theta-j\omega x/\bar{\phi}+j\omega\xi}$ term represents the vortical effects, $e^{jn\theta-|n|x+j\omega\xi}$ and $e^{jn\theta+|n|x+j\omega\xi}$ represents the potential effects.

We note that there are three unknown parameters for the flow in each duct region. The main idea of the following derivation is: we solve the flow field of the duct between the compressor and the bleed valves using compressor exit quantities. Based on this, we can get flow quantities at station 4. The flow field between the bleed valves and the plenum is solved using quantities at station 5, with the assumption that the flow is mixed out in the plenum. Finally, we use the actuator disk relation across the bleed valves to match the flow field solutions and complete the derivation. We also need to note that the general solution is valid for each duct region, so the axial coordinate $x$ is a local coordinate, whose origin is different in each duct region.

We start the derivation for the duct between the bleed valves and the plenum (from station 5 to 6). The expansion coefficients are written as $A_n^{②}$, $B_n^{②}$, $C_n^{②}$, where the superscript ② means it is for the region from station 5 to 6. Assuming the plenum is far downstream, and that the flow there is uniform, the flow field solution should

not have exponentially growing terms along the axial direction. Thus we have

$$\begin{cases} C_n^{②} &= 0 \\ B_n^{②} &= \dfrac{\hat{\psi}_{n,5}}{(\dfrac{j\omega}{|n|} - \bar{\phi})} \\ A_n^{②} &= \hat{\phi}_{n,5} - B_n^{②} \end{cases} \tag{3.4}$$

For the duct between the compressor and bleed valves (denoted by superscript ①), we use the quantities of station 3 to solve for the expansion coefficients, yielding

$$\begin{cases} A_n^{①} &= \dfrac{-\bar{\phi}\hat{\psi}_{n,3} + \dfrac{\omega^2}{n^2}\hat{\phi}_{n,3}}{\dfrac{\omega^2}{n^2} + \bar{\phi}^2}, \\ B_n^{①} &= \dfrac{\dfrac{j\omega}{|n|}\hat{\phi}_{n,3} + \hat{\psi}_{n,3}}{2(\dfrac{j\omega}{|n|} - \bar{\phi})}, \\ C_n^{①} &= \dfrac{\dfrac{j\omega}{|n|}\hat{\phi}_{n,3} - \hat{\psi}_{n,3}}{2(\dfrac{j\omega}{|n|} + \bar{\phi})}, \end{cases} \tag{3.5}$$

The matching conditions for station 4 and 5 are the mass and momentum equations across the bleed valves (Equation (3.1) and (3.2)). The circumferential velocity remains the same across the bleed valves, because the bleed valves do not induce any swirl. The quantities at station 4 and 5 can be obtained from the general solution with the above coefficients.

Because the total bleed mass flow is about 15% of the mean flow, we regard the bleed mass flow as "small". We also assume that the disturbances are "small" compared to the mean flow under the consideration that the actuation will be saturated and the system will not be stable beyond this disturbance level. In the process of linearization, we neglect quadratic forms of these "small" quantities. Linearization of

Equation (3.2) gives

$$\bar{\psi}_4 = \bar{\psi}_5 - \bar{\phi}_4\bar{\phi}_b, \tag{3.6}$$

and

$$\hat{\psi}_{n,4} = \hat{\psi}_{n,5} - \bar{\phi}_4\hat{\phi}_{bn}. \tag{3.7}$$

So the matching conditions are Equation (3.7), the following continuity equation:

$$\hat{\phi}_{n,4} = \hat{\phi}_{n,5} + \hat{\phi}_{bn}, \tag{3.8}$$

and

$$\frac{\delta v}{U}|_4 = \frac{\delta v}{U}|_5. \tag{3.9}$$

Algebraic manipulation of these equations gives the following relation:

$$\frac{j\omega}{|n|}\hat{\phi}_{n,3} - \hat{\psi}_{n,3} = \bar{\phi}\hat{\phi}_{bn}e^{-|n|l_b} + \frac{j\omega}{|n|}\hat{\phi}_{bn}e^{-|n|l_b}. \tag{3.10}$$

We can also write this in differential form as follow:

$$\delta\psi_3 = \frac{1}{|n|}\dot{\delta\phi} - \frac{1}{|n|}\delta\dot{\phi}_b e^{-|n|l_b} - \bar{\phi}\delta\phi_b e^{-|n|l_b}. \tag{3.11}$$

The differential equation for the mean quantities can be similarly derived as shown by Moore and Greitzer [18] with additional consideration of mass conservation across the bleed valves. We have the following equation

$$\psi - \psi_3 = -(l_b + l_d)\dot{\bar{\phi}} + l_d\dot{\bar{\phi}}_b + \bar{\phi}\bar{\phi}_b \tag{3.12}$$

where $l_d = l_e - l_b$. As we will see later, the states of the system (variables that fully describe the system behavior) are the flow coefficient at the compressor face and

plenum pressure. In the above two equations, we drop the subscript of $\psi_6$ as $\psi$. We also write mass flow at compressor face $\phi_2$ and $\phi_3$ (they are equal) as $\phi$ by dropping the subscripts.

The pressure relation of upstream and compressor can be derived in the exact same way as in Reference [18, 20]. The upstream pressure relation is

$$\frac{P_{t2} - P_{t0}}{\rho U^2} = -\frac{1}{|n|}\frac{\partial \delta\phi}{\partial t} - l_I \frac{\partial \bar{\phi}}{\partial \xi} + \Psi_{dist}(\theta) \tag{3.13}$$

where $\Psi_{dist}$ represents the total pressure loss across the inlet distortion screen. The total-to-static pressure rise across the compressor is modeled as

$$\frac{P_3 - P_{t2}}{\rho U^2} = \psi_c(\phi) - \lambda \frac{\partial \phi}{\partial \theta}|_{\eta=0} - \mu \frac{\partial \phi}{\partial \xi}|_{\eta=0} \tag{3.14}$$

where $\mu$ and $\lambda$ are inertia parameters for the rotor and the full compressor respectively. $\psi_c(\phi)$ is the steady state compressor characteristic.

The plenum mass flow balance gives

$$\dot{\psi} = \frac{1}{4 l_c B^2}\left[\bar{\phi} + \bar{\phi}_b - \sqrt{\frac{2}{K_t}\psi}\right] \tag{3.15}$$

where $K_t$ is throttle coefficient.

Unsteady losses in the compressor are also considered. The unsteady losses in the rotor and stator are modeled as a first order lags as derived by Haynes [20]. The time constant of this first order lag is denoted as $\tau$. Then the rotor unsteady loss $L_r$ and stator unsteady loss $L_s$ can be written as

$$\begin{aligned} \tau(\dot{L}_r + \frac{\partial L_r}{\partial \theta}) &= -L_r + R L_{ss}, \\ \tau \dot{L}_s &= -L_s + (1 - R) L_{ss}. \end{aligned} \tag{3.16}$$

where $L_{ss} = \psi_i - \psi_c$, $\psi_i$ is the ideal compressor characteristic, and $R$ is rotor reaction of the compressor.

The overall system differential equations can be obtained by combining Equation (3.11), (3.12), (3.13), (3.14), (3.15 and (3.16). Finally we obtain the system of differential equations

$$\begin{cases} l_c\dot{\bar{\phi}} + (\frac{2}{|n|} + \mu)\dot{\delta\phi} + \lambda\frac{\partial\delta\phi}{\partial\theta} = \psi_c(\phi) - \psi + \Psi_{dist} + (l_d\dot{\bar{\phi}}_b + \frac{1}{|n|}\dot{\delta\phi}_b e^{-|n|l_b}) \\ \qquad\qquad + (\dot{\bar{\phi}}\bar{\phi}_b + \dot{\bar{\phi}}\delta\phi_b e^{-|n|l_b}), \\ \dot{\psi} = \frac{1}{4l_cB^2}\left[\bar{\phi} - \bar{\phi}_b - \sqrt{\frac{2}{K_t}}\psi\right], \\ \tau(\dot{L}_r + \frac{\partial L_r}{\partial\theta}) = -L_r + RL_{ss}, \\ \tau\dot{L}_s = -L_s + (1-R)L_{ss}. \end{cases} \tag{3.17}$$

Where $l_c = l_I + \mu + l_d$ is the effective length of the compression system. $\tau$ is the time constant of unsteady losses. $R$ is the rotor reaction of the compressor. $B$ is Greitzer's B parameter [6] characterizing the compliance of the plenum.

From Equation (3.10), we see that the effect of the downstream bleed on the compressor is a potential one, which is subject to exponential decay as it goes upstream. This implies that the actuators should be located close to the compressor in order to control higher spatial harmonics.

### 3.3.3 Distributed Nature of Actuation

The actuation action in real life does not vary continuously around the annulus. If the number of actuators is enough to generate the required control modes, it is appropriate to approximate the actuation as continuous around the annulus. In our case, there are only four bleed valves. To account for this discrete nature of the actuations, a model is constructed.

We start with one actuator and describe its effect on the compressor. To get the complete actuation effect, we then add the circumferential contribution of each actuator. The bleed mass flow circumferential distribution of one actuator is assumed to have a square shape, with the peak centered at the location of the actuator. Fig-

ure 3-2 shows a duct segment from station 3 to 4 (see Figure 3-1) with the annulus unwrapped. As indicated in the figure, $\phi_b(\bar{\theta}, \theta)$ is a square shape with a width $\Delta\theta$,

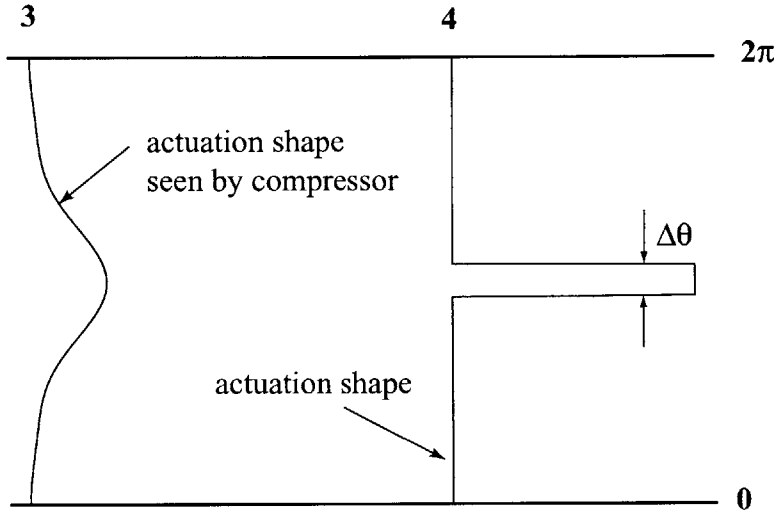


**Figure 3-2:** Distributed Nature of Actuation

which is the width of the actuator. $\bar{\theta}$ is the location of the actuator centerline. The upstream decayed effect seen by the compressor is also illustrated.

The bleed mass flow $\phi_b(\bar{\theta}, \theta)$ is decomposed into spatial Fourier form:

$$\phi_b(\bar{\theta}, \theta) = a_0 + \sum_{n=1}^{N} (a_n(\bar{\theta}) cosn\theta + b_n(\bar{\theta}) sinn\theta).$$

Then the mass flow with exponential decay (seen by the compressor) $f(\bar{\theta}, \theta) = \phi_b(\bar{\theta}, \theta) e^{-nl_b}$ can be written as

$$f(\bar{\theta}, \theta) = a_0 + \sum_{n=1}^{N} e^{-nl_b} (a_n(\bar{\theta}) \cos n\theta + b_n(\bar{\theta}) \sin n\theta)$$

where

$$a_0 = \bar{\phi}_b = \frac{\Delta\theta}{2\pi},$$

$$a_n = \frac{1}{\pi} \int_0^{2\pi} \phi_b(\bar{\theta}, \theta) cosn\theta d\theta = \frac{1}{n\pi} \sin n\theta |_{\bar{\theta}-\Delta\theta/2}^{\bar{\theta}+\Delta\theta/2},$$

$$b_n = \frac{1}{\pi}\int_0^{2\pi} \phi_b(\bar{\theta},\theta) sinn\theta d\theta = -\frac{1}{n\pi}\cos n\theta|_{\bar{\theta}-\Delta\theta/2}^{\bar{\theta}+\Delta\theta/2}.$$

In our case, the distance between compressor exit and the bleed valves (between station 3 and 4) is the non-dimensional length ($l_b = 1$). The number of spatial modes N needed is found to be only three by comparing the resulted $\phi_b(\bar{\theta},\theta)e^{-n}$ ($l_b = 1$) with $N = 3$ and $N = 250$.

To obtain the complete actuation effect, we first define the following matrix $\mathcal{F}$:

$$\mathcal{F} = \begin{pmatrix} f(\bar{\theta}_1,\theta_1) & f(\bar{\theta}_2,\theta_1) & f(\bar{\theta}_3,\theta_1) & f(\bar{\theta}_4,\theta_1) \\ f(\bar{\theta}_1,\theta_2) & f(\bar{\theta}_2,\theta_2) & f(\bar{\theta}_3,\theta_2) & f(\bar{\theta}_4,\theta_2) \\ \cdots & \cdots & \cdots & \cdots \\ f(\bar{\theta}_1,\theta_M) & f(\bar{\theta}_2,\theta_M) & f(\bar{\theta}_3,\theta_M) & f(\bar{\theta}_4,\theta_M) \end{pmatrix} \tag{3.18}$$

where $\bar{\theta}_m, m = 1,2,3,4$ is the location of the nth actuator. $\mathcal{F}$ is a coefficient matrix which transform the discrete valve commands into circumferential actuation waves. The term $\bar{\phi}\phi_b e^{-|n|l_b}$ in the system equations can be written as

$$\begin{pmatrix} \vdots \\ \bar{\phi}\phi_b(\theta_k)e^{-|n|l_b} \\ \vdots \end{pmatrix} = \bar{\phi}\mathcal{F}\begin{pmatrix} u_1 \\ u_2 \\ u_3 \\ u_4 \end{pmatrix}$$

where $u_1$, $u_2$, $u_3$, $u_4$ are the bleed mass flow rates for each actuator. More details on this discrete representation are given in the next subsection.

### 3.3.4 State Space Representation

The model developed in the last subsection can be written in state space form, which is more convenient for analysis, simulation and control design. Mansoux [27] developed a state space representation of the Moore-Greitzer model by choosing circumferential mass flows at finite circumferential positions and plenum pressure to

be states. This representation actually discretizes the flow quantities along the circumferential axis. We will convert our model into this kind of state space by briefly introducing the notation, omitting the detailed derivations. For more information, see Mansoux [27].

Underlined variables are vectors of circumferential quantities. The discrete spatial Fourier transform matrices are defined as follows, where $N$ is the number of spatial modes.

$$F = \frac{1}{2N+1} \begin{bmatrix} & \vdots & \\ \cdots & \left(e^{\frac{-j2\pi}{2N+1}}\right)^{nk} & \cdots \\ & \vdots & \end{bmatrix}_{n=+N}^{n=-N}$$

Using this notation, the system of differential equations (3.17) can be written as

$$\begin{cases} E\dot{\underline{\phi}} = -A\underline{\phi} + \psi_c(\underline{\phi}) - T\psi + \underline{\Psi}_{dist} + (S^T\underline{\phi})\mathcal{F}\underline{u} + \mathcal{G}\mathcal{F}\dot{\underline{u}} \\ \dot{\psi} = \dfrac{1}{4l_cB^2}\left[S^T\underline{\phi} - S^T\mathcal{F}\underline{u} - \sqrt{\dfrac{2}{K_t}\psi}\right] \\ \tau\dot{\underline{L_r}} = -J\underline{L_r} + r\underline{L_{ss}} \\ \tau\dot{\underline{L_s}} = -\underline{L_s} + (1-r)\underline{L_{ss}} \end{cases} \tag{3.19}$$

where

$$E = F^{-1} \begin{pmatrix} \ddots & & & & \\ & \frac{2}{|n|} + \mu & & \mathbf{0} & \\ & & \ddots & & \\ & & & l_c & \\ & & & & \ddots \\ & \mathbf{0} & & & \frac{2}{|n|} + \mu \\ & & & & & \ddots \end{pmatrix}_{n=+N}^{n=-N} F$$

$$\mathcal{G} = F^{-1} \begin{pmatrix} \ddots & & & & & \\ & \frac{1}{|n|} & & \mathbf{0} & & \\ & & \ddots & & & \\ & & & l_d & & \\ & & & & \ddots & \\ & \mathbf{0} & & & \frac{1}{|n|} & \\ & & & & & \ddots \end{pmatrix}_{n=+N}^{n=-N} F$$

$$J = (I + \tau F^{-1} D_r F), \quad S^T = \frac{1}{2N+1}[1, 1, \cdots, 1, 1], \quad T = [1, 1, \cdots, 1, 1]^T$$

$$A = F^{-1} \begin{pmatrix} \ddots & & \\ & j\lambda n & \\ & & \ddots \end{pmatrix} F, \quad D_r = \begin{pmatrix} \ddots & & \\ & jn & \\ & & \ddots \end{pmatrix}$$

## 3.4 Model Validation

In order to verify the actuation model constructed in Section 3.3, experimental steady state and forced response results are presented in this section, including comparisons to model predictions. The methods and procedures to conduct system identification by measuring forced responses were described by Paduano [19]. In Section 3.4.2, we introduce these methods briefly. The model is linearized around the operating points of the experiments. Linearized comparisons are then conducted.

### 3.4.1 Steady State Measurement

Steady state measurements of system pressure rise were conducted with the bleed valves either fully open or fully closed. The results show that the plenum pressure rise with bleed valves fully open is higher than that with the bleed valves fully close. It is reasonable to assume that pressure rise at the compressor exit is the same for these two cases for a given upstream mass flow setting . So the higher plenum pressure

is caused by the changes due to the downstream components (i.e. the bleed valves). This is quantitatively consistent with the actuator disk treatment of the bleed in Section 3.3, where the momentum equation implies pressure rise across the bleed valves due to the diffuser-like effect of bleed. Steady state pressure rises are shown in Figure 3-3. In the figure, it is also shown that the compressor exhibits very deep hysteresis.

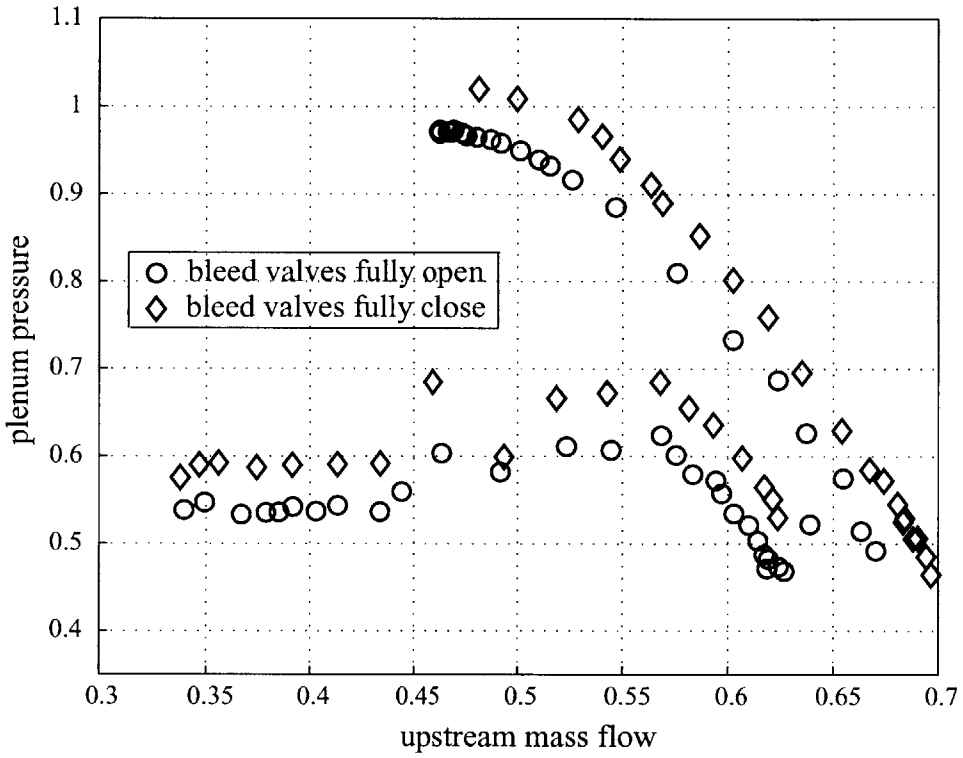


**Figure 3-3:** Steady State Pressure Rise in Plenum

From Equation 3.6, the steady state pressure rise across the bleed valves is $\bar{\phi}\bar{\phi}_b$. We can assume that the characteristics of the bleed valves are quadratic curves (the same as any orifice or throttle). Therefore we write the pressure rise across the bleed station as

$$\delta\psi = \bar{\phi}\bar{\phi}_b = \bar{\phi}\gamma\sqrt{\psi_3}$$

where $\gamma$ represents the bleed valve opening, and $\psi_3$ is the pressure at the compressor exit. In the steady state, pressure at the compressor exit is the same as pressure just before the bleed valves. To verify this pressure rise expression, we start by calculating

the value of $\delta\psi$ using the experimental data shown in Figure 3-3. The bleed valves are set fully open in this test, so $\gamma$ can be assumed constant (we didn't directly measure it). If this remains true at different operating points, we are confident that the expression is appropriate. The result is plotted in Figure 3-4. Only stable (i.e. steady) operating points are taken into account in calculating $\gamma$.

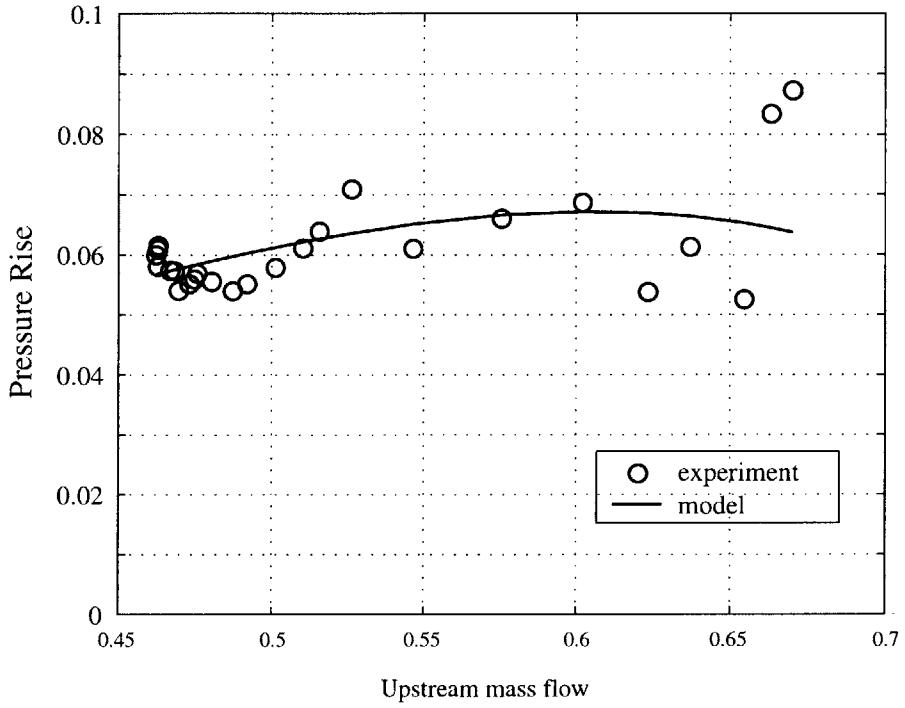


**Figure 3-4:** Estimation of Bleed Valve Opening $\gamma$

In Figure 3-4, circles represent the pressure rise calculated from experimental data. The solid line is calculated from the model. From the results, we observe that the model prediction agrees with the experimental data well. The data in higher mass flow region is more scattered, but the model will not be used in that region.

### 3.4.2 Forced Response Experiments

System identification experiments were performed to verify the dynamics of the model we constructed. There are various methods of system identification as described by Paduano [19]. Here we use the sinusoidal excitation, which is a widely used method

for measuring transfer functions in very noisy environments. In our case, because of the decay of the spatial modes of actuation, the signal-to-noise-ratio (SNR) is low, especially for higher spatial modes. To extract the system dynamics, sinusoidal excitations were done at multiple discrete frequencies, over the frequency range of interest. Then the magnitude and phase of the outputs were measured and calculated by calculating the power density of each frequency content. In order to compare the results with the MIMO model, the excitations were performed on one bleed valve each time. Details can be found in many references [19, 15].

To compare the experimental results and model predictions, the state space model (Equation 3.19) is linearized around equilibrium points (stable operating points) by first order Taylor expansions of the nonlinear terms. The resulted linear state space model is then transformed into transfer function form as

$$\begin{pmatrix} \phi_1 \\ \phi_2 \\ \vdots \\ \phi_8 \end{pmatrix}(s) = \begin{pmatrix} g_{11}(s) & g_{21}(s) & \cdots & g_{41}(s) \\ g_{12}(s) & g_{22}(s) & \cdots & g_{42}(s) \\ \cdots & \cdots & \cdots & \cdots \\ g_{18} & g_{28} & \cdots & g_{48}(s) \end{pmatrix} \begin{pmatrix} u_1 \\ u_2 \\ u_3 \\ u_4 \end{pmatrix}(s)$$

where $\phi_n$ is the flow coefficient measured by the nth hotwire and $u_n$ is the nth actuator. In our case, there are eight hotwires and four bleed valves. Due to circumferential symmetry, there are only eight independent elements of the transfer function matrix. For example

$$g_{11}(s) = g_{23}(s) = g_{35}(s) = g_{47}(s)$$

So, theoretically we only need to excite one actautor to identify all of the system dynamics. In practice, we excite each of the four bleed valves separately to verify the symmetry and also get four sets of data for each independent transfer function by the above equality.

The experiments were run at three different mass flows. The excitations were done using the full range of actuator motion, to get the clearest output signals. The data are processed and plotted in frequency response form. In the following, we will

present the one closest to the stall point of the three cases.

Figures 3-5 through 3-12 are the frequency responses computed by actuating bleed valve No. 1. As we mentioned above, the data corresponding to other valves are also put in these plots by appropriately shifting indices. Different symbols represent data from different bleed valves. The results show that the bleed model captures the system dynamics very well. There are two resonant peaks in each magnitude plot, which represent respectively the surge mode (frequency around 2.5Hz) and first rotating stall mode (frequency around 13Hz). Data at lower frequencies (around 0.1Hz) are not accurate because we only recorded 16 seconds of data (less than one cycle of those frequency contents). Therefore the calculation of the power spectra at these frequencies is not accurate. At the high frequency end, the SNR is low because the higher actuation modes decay upstream, which make the hotwire outputs relatively small under the same noisy background. So we didn't pursue frequencies higher than the second rotating stall mode.

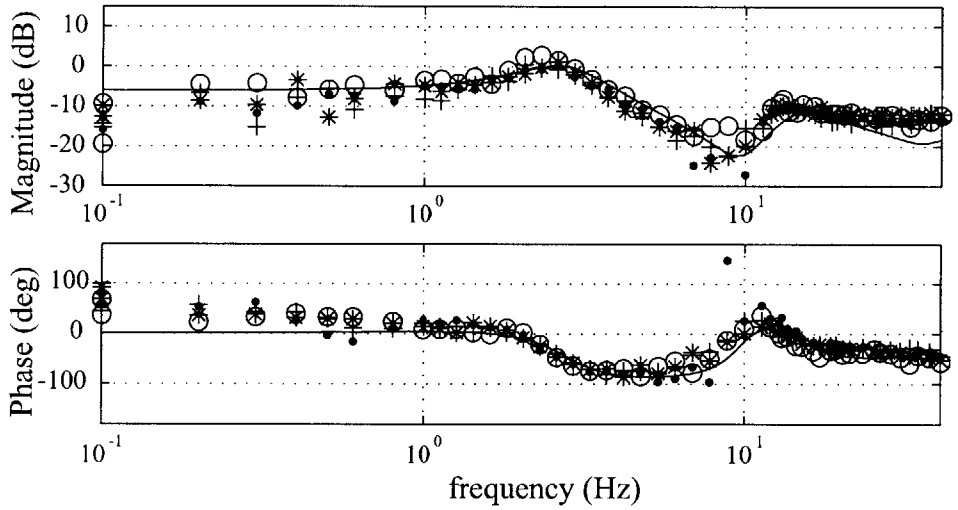


**Figure 3-5:** Frequency Response of $g_{11}(s)$ (symbols are experiment data, solid line is model prediction), $\bar{\phi}$ = stalling mass flow + 1.5%

To conduct more comparisons at different mass flow settings, we first average the four sets of data for each transfer function. Then we fit poles and zeros to each transfer function. By comparing with model predictions, we can clearly see how these poles and zeros migrate with changing operating points.

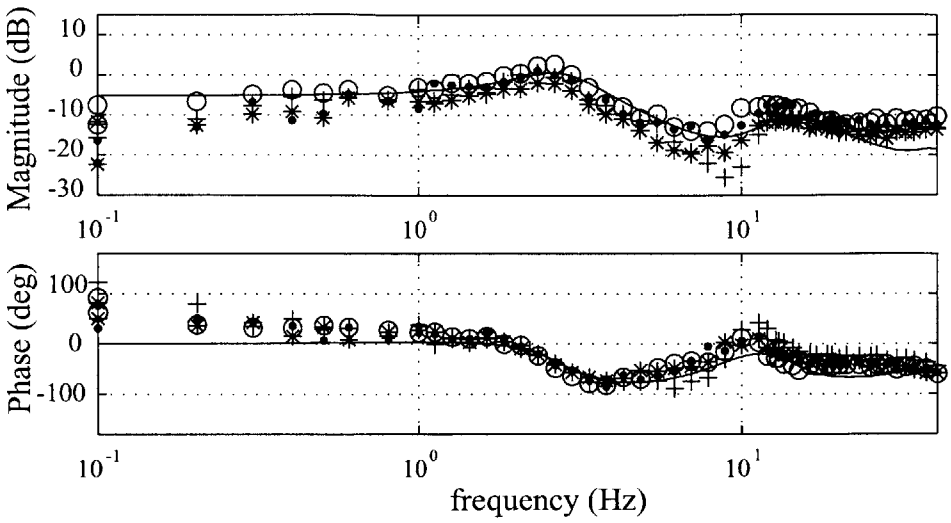


**Figure 3-6:** Frequency Response of $g_{12}(s)$ (symbols are experiment data, solid line is model prediction), $\bar{\phi}$ = stalling mass flow + 1.5%

Figures 3-13 and 3-14 show the poles and zeros of the experiments and corresponding model predictions. From these figures, we observe that there are two sets of system poles (in rectangular frames) with surge frequency (the lower ones) and first rotating stall mode (the upper ones). There is also a set of zeros. As predicted by theory, the poles and zeros migrate toward the imaginary axis as the mass flow is reduced.

From these figures, we see that the agreement between the experiment data and the model predictions is better for $g_{11}(s)$, $g_{12}(s)$, $g_{17}$ and $g_{18}(s)$ than for the other other transfer functions. This is because the responses for these transfer functions come from those hot wires which are closer to the alignment of actuated bleed valves. We also note that the experimentally derived poles and zeros related to higher mass flows are not as accurate as those close to the stall mass flow, because the damping for higher mass flows is higher, resulting in weaker responses at the hot wires. The low SNR results in less accurate transfer function fits.

We can conclude from these results that the bleed model constructed in the last section captures the main dynamics of the real system. It gives us confidence that the model can be used for the investigations discussed in Chapter 5 and Chapter 6.

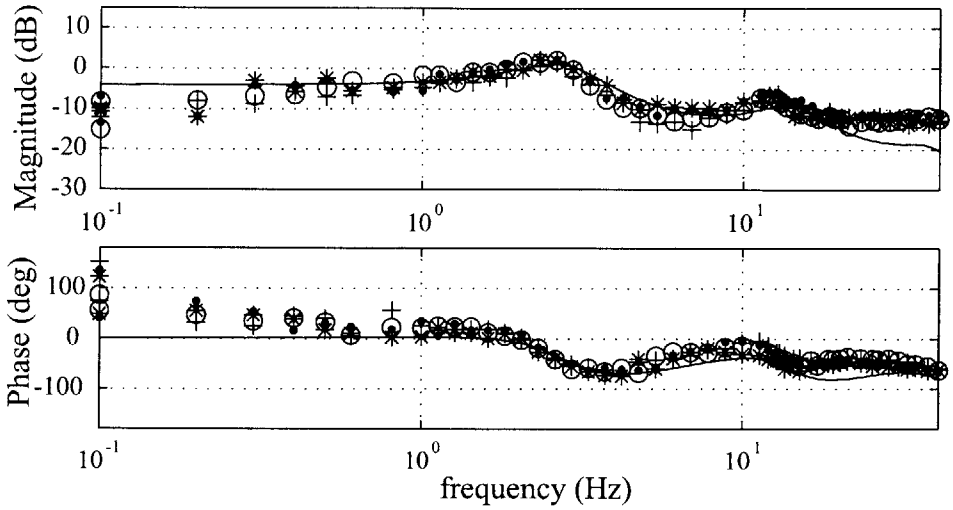


**Figure 3-7:** Frequency Response of $g_{13}(s)$ (symbols are experiment data, solid line is model prediction), $\bar{\phi}$ = stalling mass flow + 1.5%

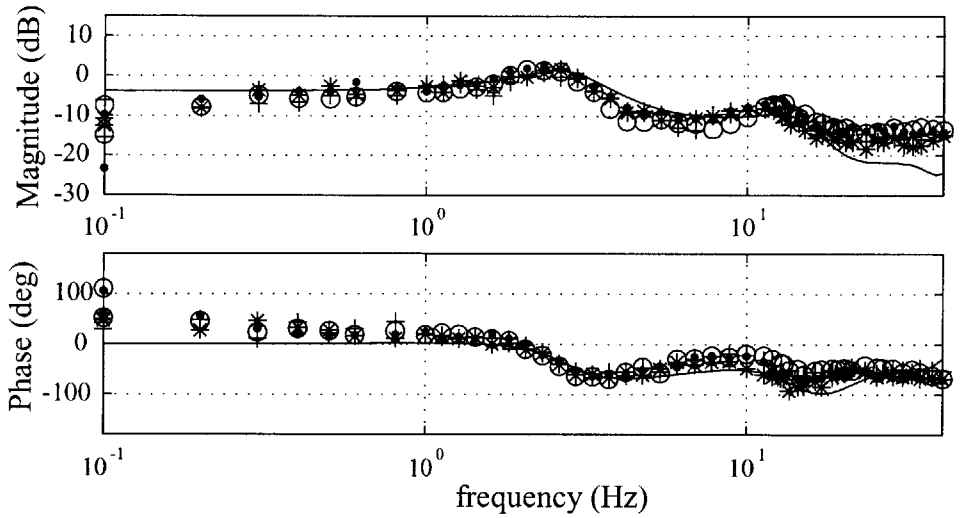


**Figure 3-8:** Frequency Response of $g_{14}(s)$ (symbols are experiment data, solid line is model prediction), $\bar{\phi}$ = stalling mass flow + 1.5%

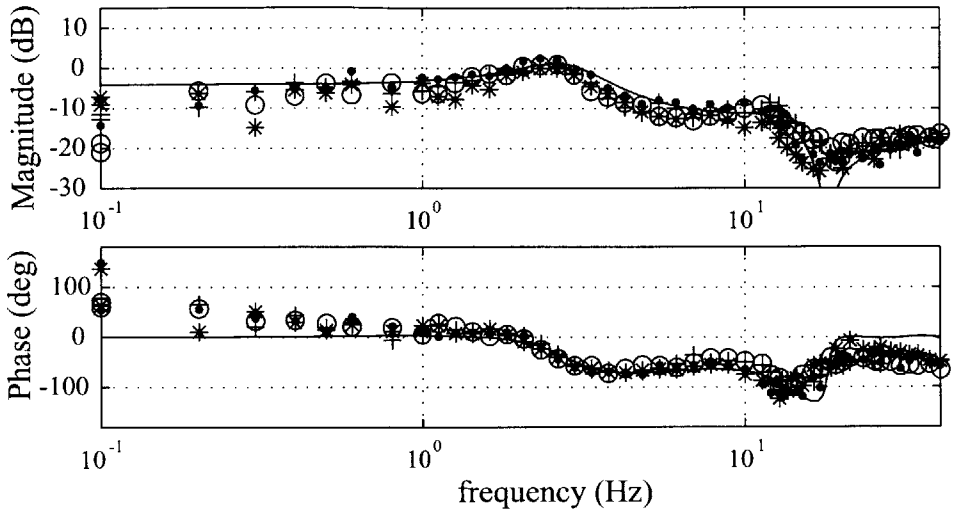


**Figure 3-9:** Frequency Response of $g_{15}(s)$ (symbols are experiment data, solid line is model prediction), $\bar{\phi}$ = stalling mass flow + 1.5%

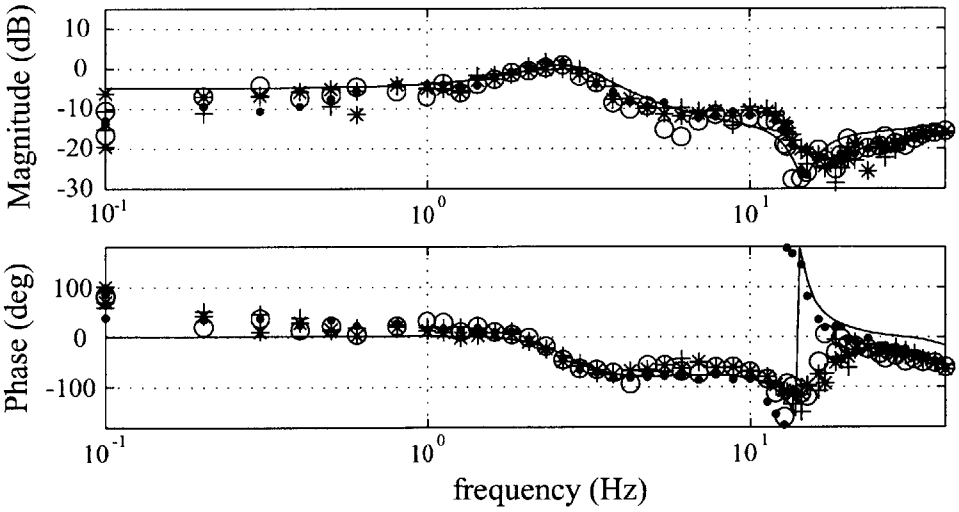


**Figure 3-10:** Frequency Response of $g_{16}(s)$ (symbols are experiment data, solid line is model prediction), $\bar{\phi}$ = stalling mass flow + 1.5%

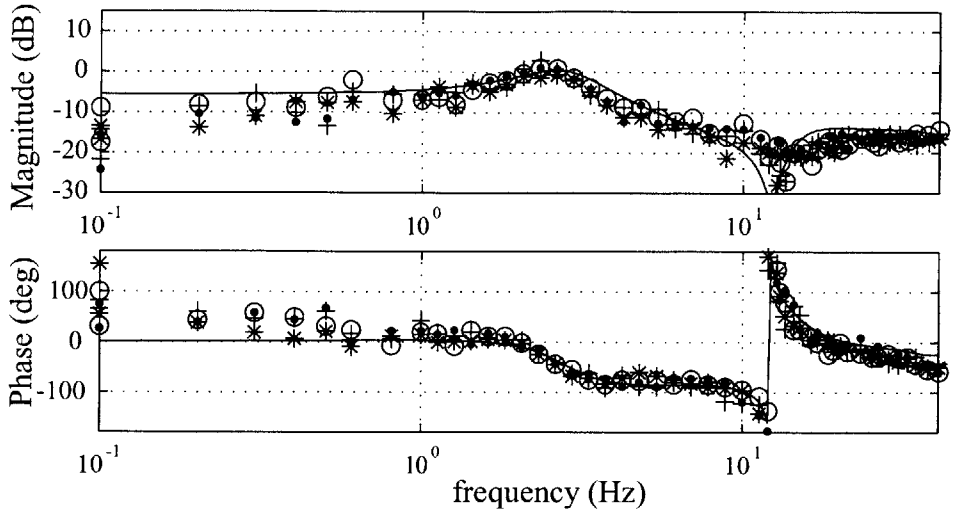


**Figure 3-11:** Frequency Response of $g_{17}(s)$ (symbols are experiment data, solid line is model prediction), $\bar{\phi}$ = stalling mass flow + 1.5%

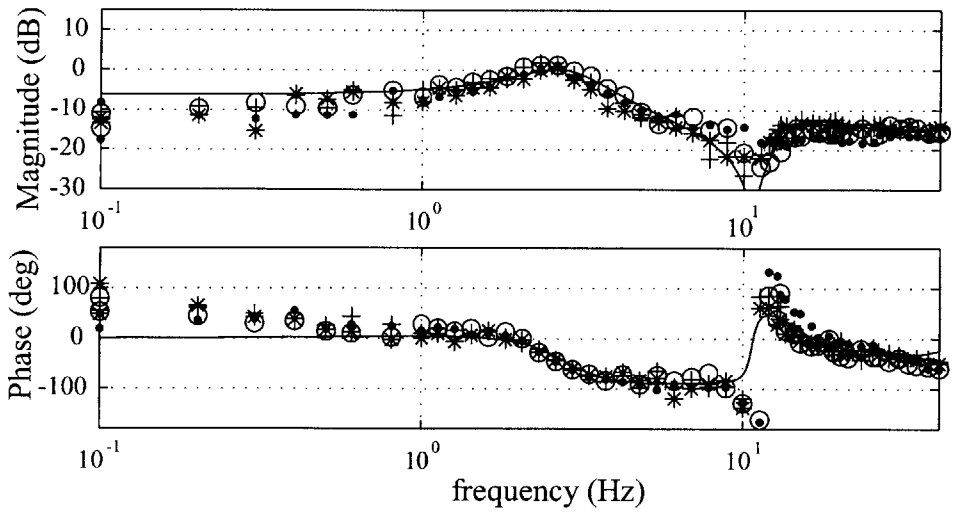


**Figure 3-12:** Frequency Response of $g_{18}(s)$ (symbols are experiment data, solid line is model prediction), $\bar{\phi}$ = stalling mass flow + 1.5%

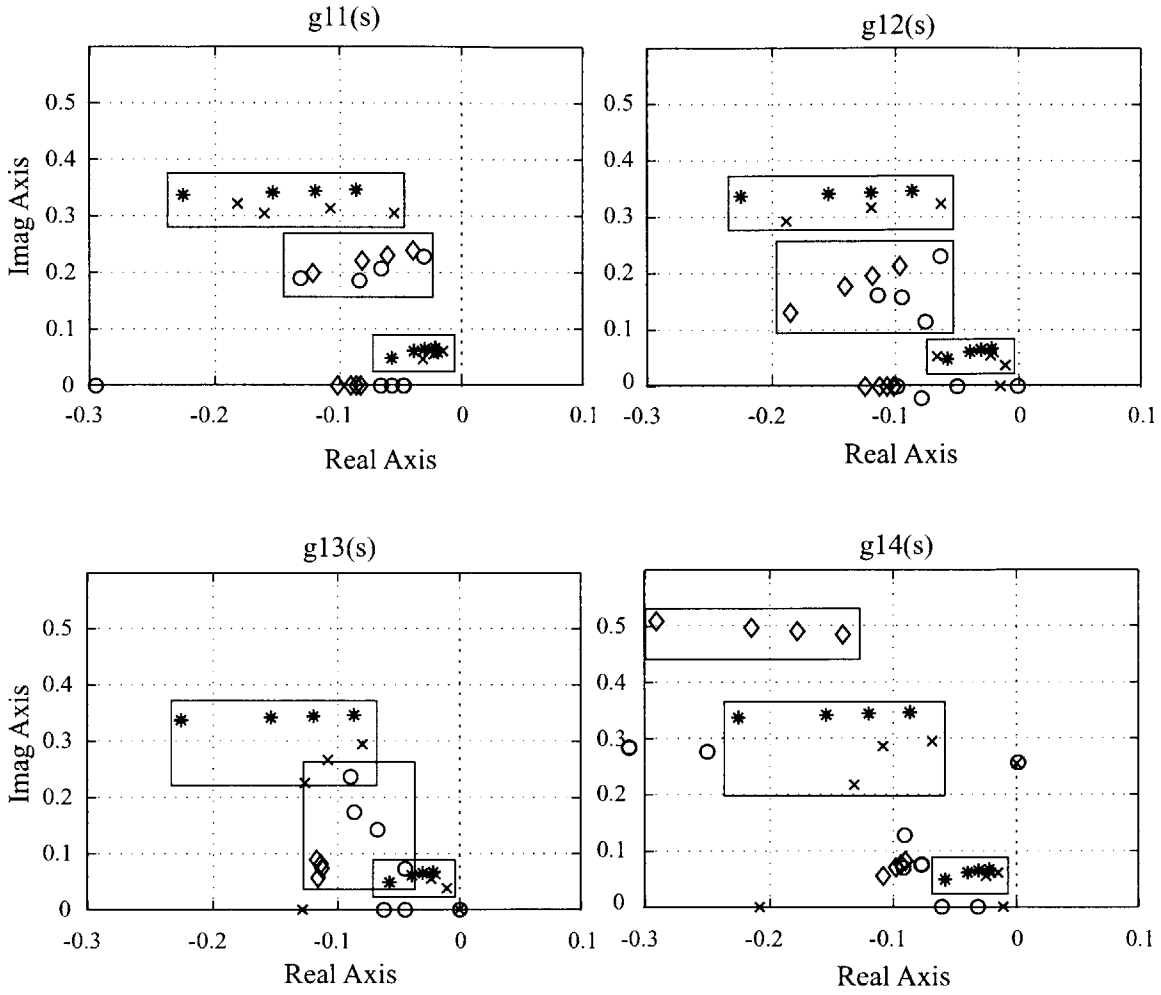


**Figure 3-13:** Pole Zero Map of $g_{11}(s) - g_{14}(s)$ (symbols: $*$ – model poles, $\Diamond$ – model zeros, $\times$ – experiment poles, $\circ$ – experiment zeros)

## 3.5 Physical Effects Of Downstream Bleed

In the last two sections, we derived and experimentally verified a downstream bleed model. To better understand what the bleed valves do to the system, we here explore the downstream bleed from an intuitive physical perspective.

As we did in the model, we only account for mass and momentum relations across the bleed valves. First, we note that bleeding mass flow is very similar to opening the main throttle in the sense of the mean flow. If the mean bleed mass flow is larger

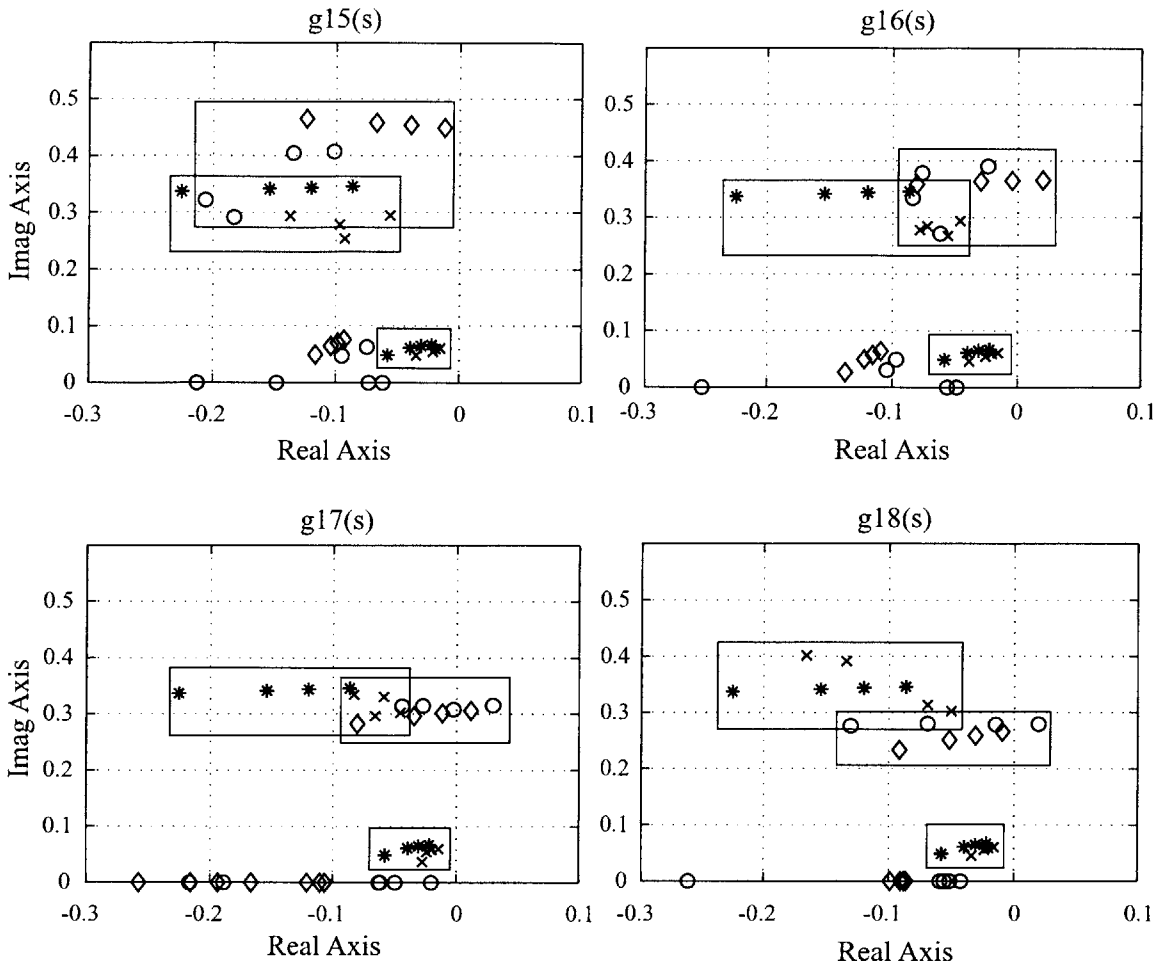


**Figure 3-14:** Pole Zero Map of $g_{15}(s) - g_{18}(s)$ (symbols: $*$ – model poles, $\Diamond$ – model zeros, $\times$ – experiment poles, $\circ$ – experiment zeros)

than zero, the equation for plenum then becomes

$$\begin{aligned} 4l_c B^2 \dot{\psi} &= \bar{\phi}_d - \sqrt{\frac{2}{K_t}\psi} \\ &= \bar{\phi} - \bar{\phi}_b - \sqrt{\frac{2}{K_t}\psi} \\ &= \bar{\phi} - \sqrt{\frac{2}{K_{t,eff}}\psi} \end{aligned}$$

where $\bar{\phi}_d$ is the mean mass flow downstream of the bleed valves and $K_{t,eff}$ is an "effective" throttle parameter. So bleeding mass flow is similar to opening the throttle, which is known to have a stabilizing effect.

Momentum conservation implies pressure rise across the bleed valves. This means

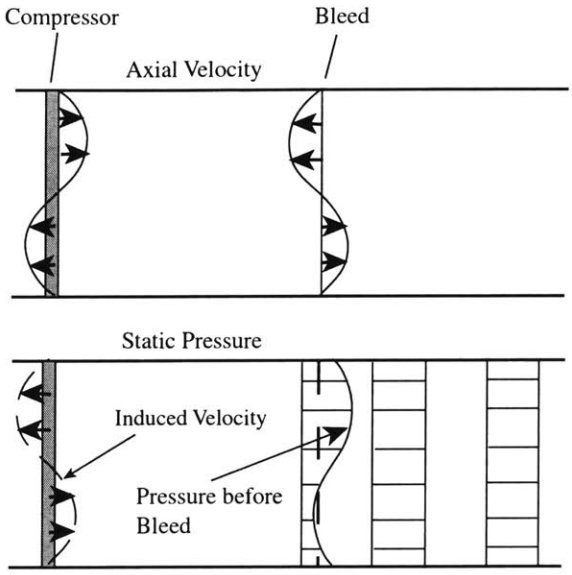


**Figure 3-15:** Physical Explanation of Bleed Effects

that the bleed valves act like local diffusers. As shown in Figure 3-15, If the local mass flow deficit exists in the compressor (destabilizing effect), the controller makes the bleed valves open locally corresponding to that annular location. Then pressure rise across the local bleed is generated by this opening. Because the static pressure far down stream remains uniform, to account for the local pressure rise, the local static pressure just before the bleed valves must go down. The local flow at that location of the flow defect is thus accelerated due to the reduced back pressure. Base on this discussion, we conclude that flow defects can be mitigated by bleeding mass flow. So this "diffuser-like" local pressure rise is introduced as stabilizing effect.

As indicated by Greitzer [40], an downstream diffuser tends to be destabilizing (see also Appendix D). It seems that the mean bleed which behaves like a diffuser, would be destabilizing. The truth is that the mean bleed also have the effect of moving the operating point to high mass flows. As shown in Figure 3-16, The diffuser effect move the peak of the effective compressor characteristic to a higher mass flow. The bleed also moves the throttle line to a higher mass flow, which will have a stronger stabilizing effect on the compression system. This can be shown by calculating the slope of the equilibrium. Assume the bleed mass flow is a fixed portion of the corresponding mean mass flow (we can use the maximum portion as this constant), so

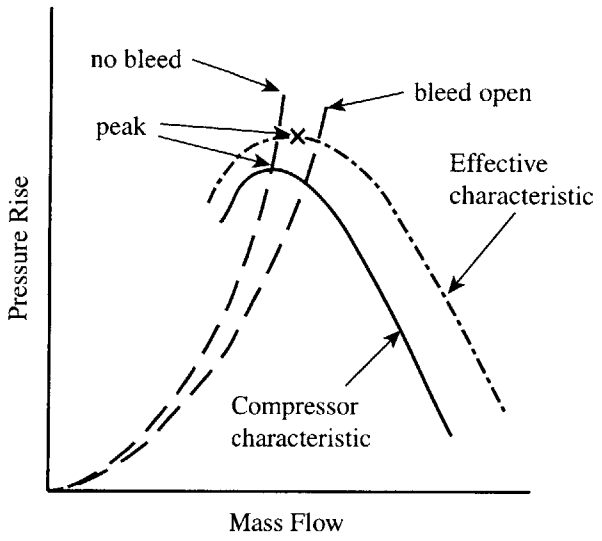


**Figure 3-16:** The Effective Compressor Characteristic

pressure rise due to bleed, $\Delta\psi$ is

$$\Delta\psi = \bar{\phi}\bar{\phi}_b = C\bar{\phi}^2$$

The effective compressor characteristic is

$$\psi_e = \psi_c + \Delta\psi$$

The slope of the effective characteristic is

$$\frac{d\psi_e}{d\phi}(\phi) = \frac{d\psi_c}{d\phi}(\phi) + 2C\phi$$

Suppose the equilibrium is at the peak ($\phi_p$), so the slope is zero. By opening the bleed, the operating point moves to ($\phi_p + \phi_b$). Using the compressor characteristic of Equation (5.1) gives

$$slope = -20.4990\phi_b + 2C\phi_p = -18.4990\phi_p < 0.$$

So, the combined effect is still stabilizing.

In the control perspective, the mean bleed will not be used to stabilize the unstable operating points, but will be used to prevent the system from going into instabilities in the face of disturbances. Especially the mean bleed will add stabilizing effect to the system when the single-sided actuation (see Chpater 4) is implemented and additional mean bleed is added.

# Chapter 4

# Range Extension Tests Of Downstream Bleed Control

In order to examine the effectiveness of the downstream bleed control, range extension tests were conducted. Stalling mass flows with and without downstream bleed control were measured to determine range extension. the frequency spectra of the hot wire signals prior to rotating stall are also examined to determine how effective the bleed valves are for suppressing the unstable modes of the compression system.

## 4.1 Constant Gain Control

A constant gain controller has been used by many researchers [19, 20, 15, 16] to demonstrate either the concept of active control or implementations of actuators. This simple controller was proved very effective. It is a good idea to start with this controller to examine the control effectiveness of downstream bleed.

The idea of constant gain feedback is based on the assumption that the spatial modes of rotating stall are decoupled. Then the spatial modes can be controlled independently. This is only true for axisymmetric flow field. Each spatial mode (the first mode and higher modes) is controlled by a proportional controller. A spatial phase shift is also accounted for to compensate computational delay and actuation

and system dynamical lags (see [20] for more details).

The constant gain controller can be written as

$$\hat{u}_n = -Ke^{i\varphi}\hat{\phi}_n, \quad n \neq 0 \tag{4.1}$$

where, $\hat{u}_n$ is the n-th harmonics of actuation, $\hat{\phi}_n$ is n-th harmonics of mass flow, $\varphi$ is spatial phase shift and $K$ is control gain. In our implementation, only the zeroth and first harmonics were used because there are only four bleed valves installed.

In the implementation of Haynes [20], the zeroth harmonic was not considered important because the B parameter was small for that case. In our case, the B parameter is large due to the addition of the large plenum. Because of this, the damping of the zeroth mode becomes small near the stall point [17]. It will be shown later that significant zeroth mode oscillations were observed in the pre-stall hot wire signals when first mode control was applied and the throttle was closed further. So a linear dynamical compensator was designed to suppress the zeroth mode oscillations which could otherwise be the most lightly damped mode as shown later.

Control gains and spatial phase shift ($\varphi$) were tuned on-line to obtain maximum steady state operating range extension.

## 4.2 Power Spectral Density Of Pre-Stall Flow Field

Power spectral densities are calculated from the hot wire signals prior to rotating stall to show which mode resonates the strongest before the compressor goes into rotating stall with either control or no control. This provides information about how well a specific spatial mode is suppressed by a given controller. To carry out this analysis, hot wire measurements around the compressor annulus were taken and decomposed into spatial Fourier coefficients. Because rotating stall precursors rotate around the annulus, they are naturally represented as phasors. The nth spatial mode

of the flow coefficient can be written as

$$\delta\phi_n^+ = a_n + jb_n \tag{4.2}$$

where $a_n$ and $b_n$ are the cosine and sine Fourier coefficients of the nth spatial mode. These phasors represent the positive direction (rotor rotating direction) rotating wave. A stationary spatial wave can be decomposed into two rotating waves with the same amplitude but in opposite rotating directions. In order to take out those non-rotating contents (such as distortions) of hot wire measurements, the following opposite direction phasors are also defined

$$\delta\phi_n^- = a_n - jb_n \tag{4.3}$$

In the results shown later, power spectral densities (PSD) of higher spatial modes ($n > 1$) are plotted into positive and negative frequencies referring to positive and negative rotating directions respectively.

Two controllers were implemented to extend the compressor operating range. One relies on the first mode control only, another one uses a combination of the zeroth and first modes feedback. Comparisons with open loop data are shown in the following results. The data shown below are generated using hot wire signals taken immediately prior to loss of stability with or without controls. So those data were taken at different operating points.

Figure 4-1 shows the PSDs of the zeroth mode of the three cases. The case with first mode control has stronger zeroth mode oscillations prior to rotating stall than the open loop case. This is because the first mode control moves the stall point to a lower mass flow where the zeroth mode becomes more lightly damped and the system is a high B system. That means we reach a more unstable flow coefficient for the zeroth mode. By adding a zeroth mode compensator, the zeroth mode oscillations were well damped (as the solid line indicates).

Figure 4-2 shows the PSDs of higher spatial modes. There is a significant reso-

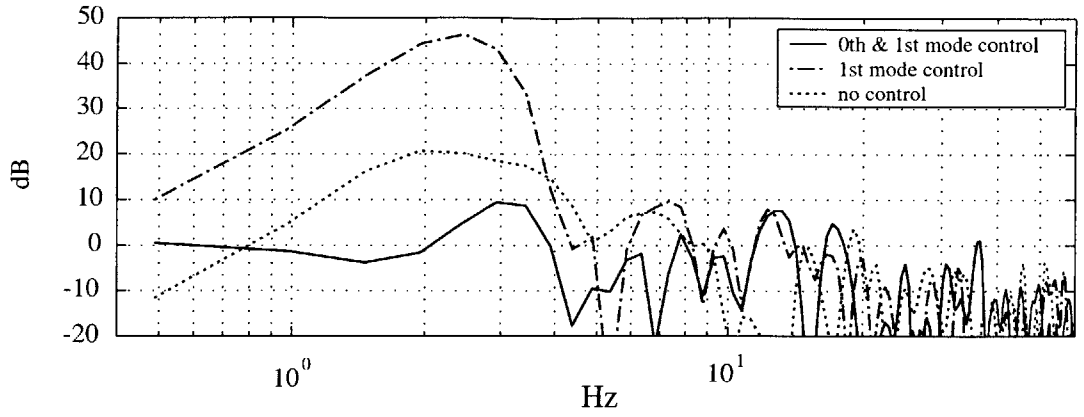


**Figure 4-1:** Power Spectral Densities of Zeroth Mode ($\bar{\phi}$ is 0.4529 for no control, 0.4458 for only the 1st mode control, 0.4440 for the 0th+1st mode control)

nance at about 13 Hz in the open loop run, which is consistent with previous reported data [20, 15] . Both controllers reduced the pre-stall first mode oscillations by about 20 dB. With only first mode control, there are no significant second mode oscillations. The zeroth mode oscillation is the most lightly damped and likely to be the factor which drove the system into instability. By adding zeroth mode control, we observed the increased second mode PSD between 30 to 40 Hz. As indicated by Paduano [19] and Haynes [20], the second mode is close to its unstable point which is beyond our control because our actuators are only capable of generating up to the first spatial mode.

Figure 4-3 shows the hot wire traces of these three runs which have different mean mass flow. In the left figure, the first mode precursor is clear over about 15 revolutions. In the middle figure, the time scale is different from the other two to show the zeroth mode oscillations with lower frequency (the mean mass flow is lower than that of the open loop case with the first mode oscillations suppressed) . In the right figure, there are visible second mode precursors for about 5 revolutions immediately prior to rotating stall inception after the zeroth and first modes were supressed.

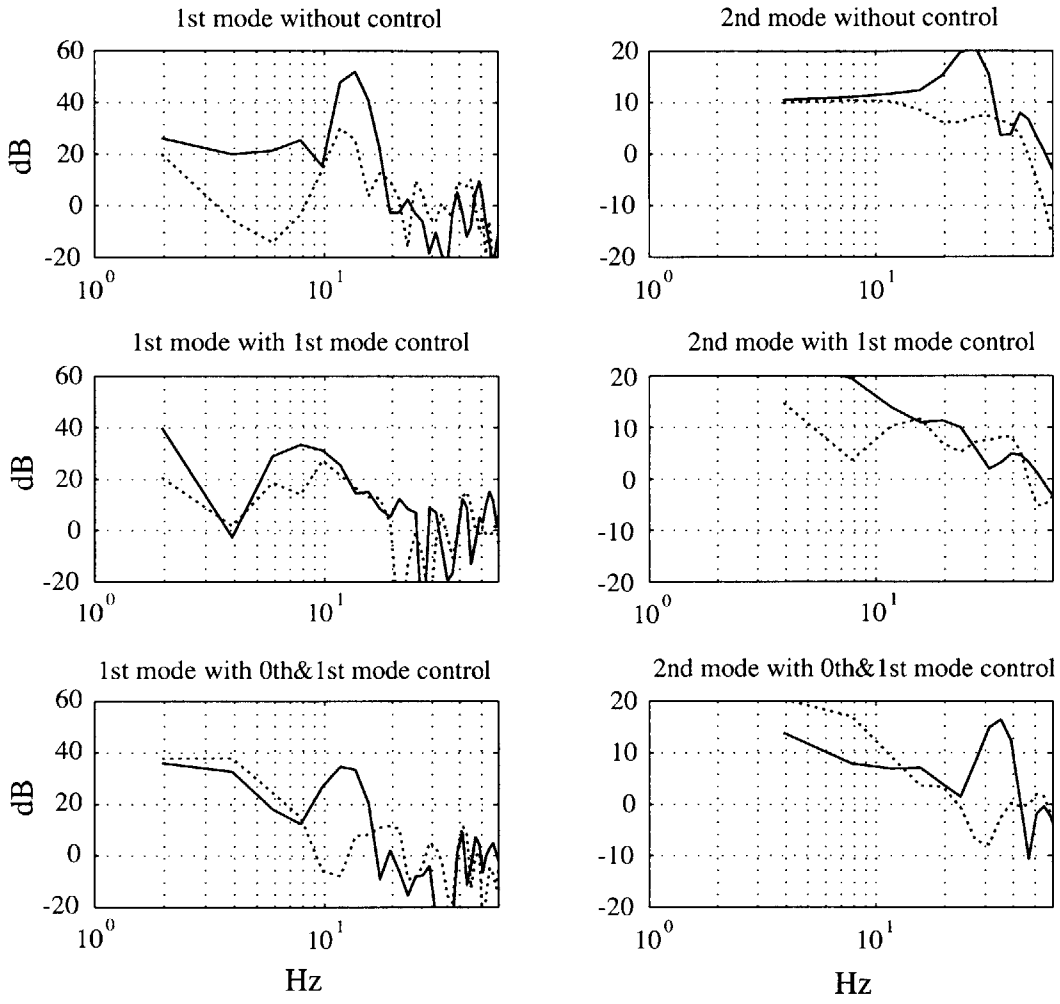


**Figure 4-2:** Power Spectral Densities of Higher Modes (solid line – positive frequency, dashed line – negative frequency), see Figure 4-1 for $\bar{\phi}$

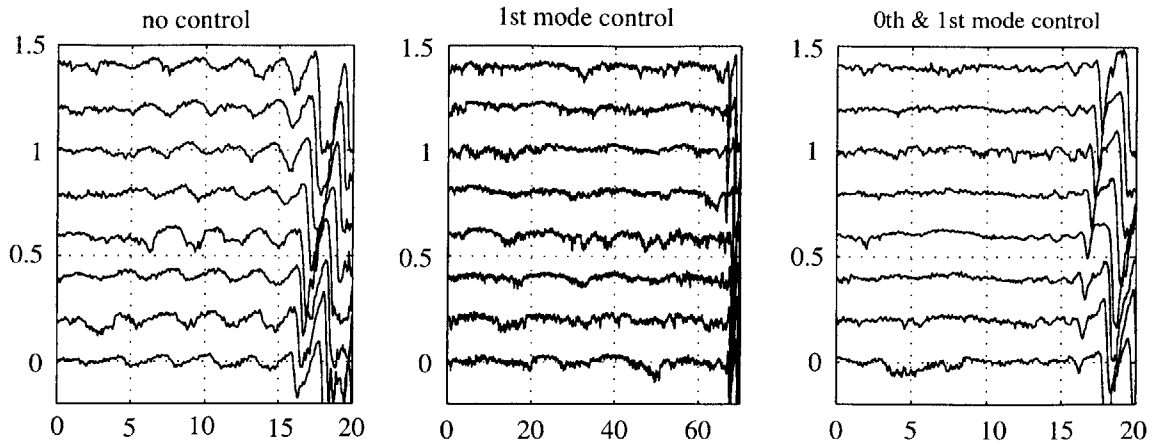


**Figure 4-3:** Hot Wire Traces

## 4.3 Steady State Performance Of Active Control

Steady state measurements of upstream flow coefficient and compressor pressure rise were taken to determine the range extension achieved by active control. Figure 4-4 shows the operating range for the open loop compressor as well as zero-th and 1st mode control.

From the results, we observe that about 2% range extension was achieved by active control of only four bleed valves, which is comparable to those by other actuators (IGVs [20], jet injection [16]). In the figure, the dotted line is the fitted stable part of the compressor characteristic. With only first mode control, the range extension is very close to that with the combination of zeroth and first mode control.

Based on these and previous experiments [19, 20], we believe that the first mode reaches first its stability boundary as we close the throttle. Then the zeroth mode becomes unstable. Further closing the throttle pushes the second mode into its unstable region. This can also be seen in the model constructed in Chapter 3. Figure 4-5 shows the real parts of the first three modes as functions of the mass flow coefficient from model prediction. It is apparent that the zeroth mode loses stability after the first mode and before the second mode, which is consistent with our observations from the experiments.

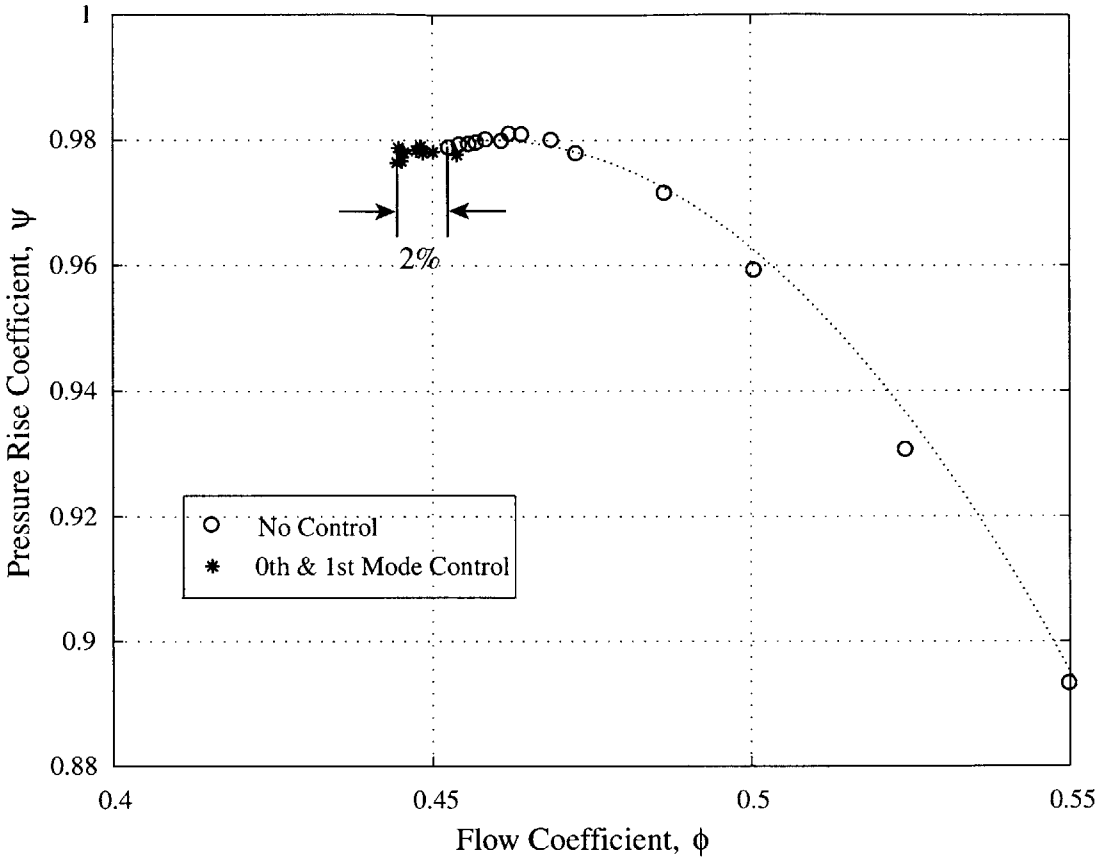


**Figure 4-4:** Compressor Characteristics With And Without Control

## 4.4 Single-Sided Actuation

The constant gain feedback control investigated above is a linear control law in which a nominal level of actuation was set and the actuation responded either decelerated or accelerated the local flow. We call this kind of actuation "double-sided" actuation. For double-sided actuation, the actuation can be positive or negative with reference to the nominal value. In real applications, there are considerations in which double-side actuation is not favorable. The nominal bleed mass flow might not be desirable because it wastes high pressure air when there are not significant circumferential waves. So the single-sided bleed scheme is a good alternative in which the actuators only react to the decelerated local flow, but not to accelerated local flow. There will be no required nominal bleed mass flow. Then actuations reacting to circumferential non-uniformities also add mean actuation to the system. As mentioned

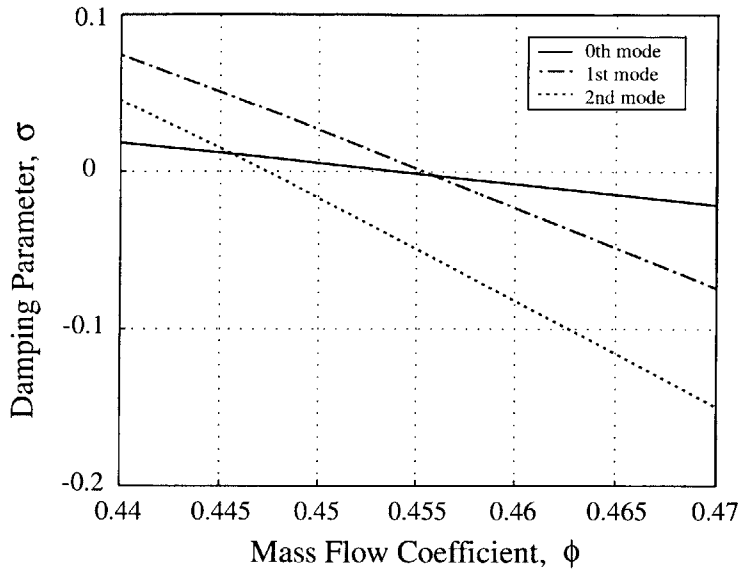


**Figure 4-5:** Stability Of Spatial Modes vs Mass Flow Coefficient

in Chapter 3, this is not a problem because the mean bleed acts like opening the main throttle, which is identified as a stabilizing effect. Instead of cutting the negative part of the first mode actuation, we actually raise the whole wave form above the zero level as shown in Figure 4-6.

The range extension achieved by single-sided bleed is also about 2%. The actuation level of single-sided bleed for normal stable runs is less than that of double-sided bleed. In order to show this, we plot the actuation level of one bleed valve for these two cases as shown in Figure 4-7. The time average opening of the valve is 5.64° for single-side actuation, 24.06° for double-side actuation. So total bleeded air of single-side bleed is much less than that of double-side bleed. We will use single-sided bleed scheme for all other control tests in this thesis.

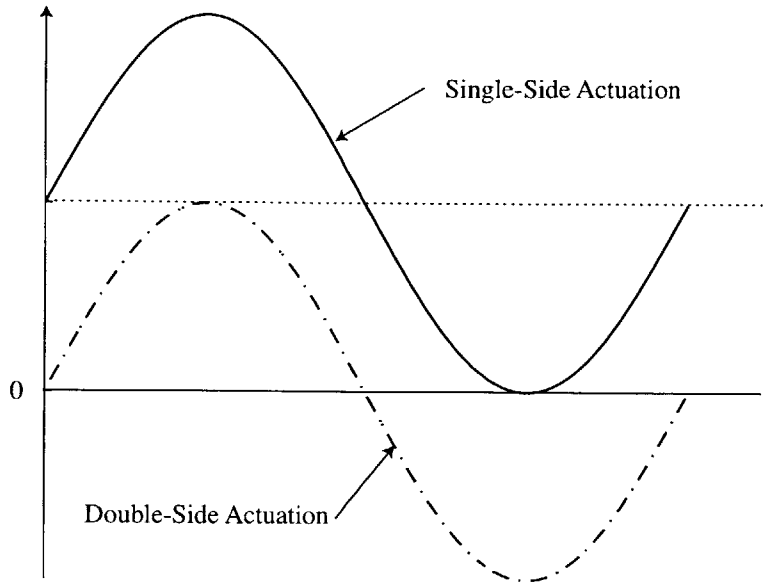


**Figure 4-6:** Single-Side Actuation Scheme

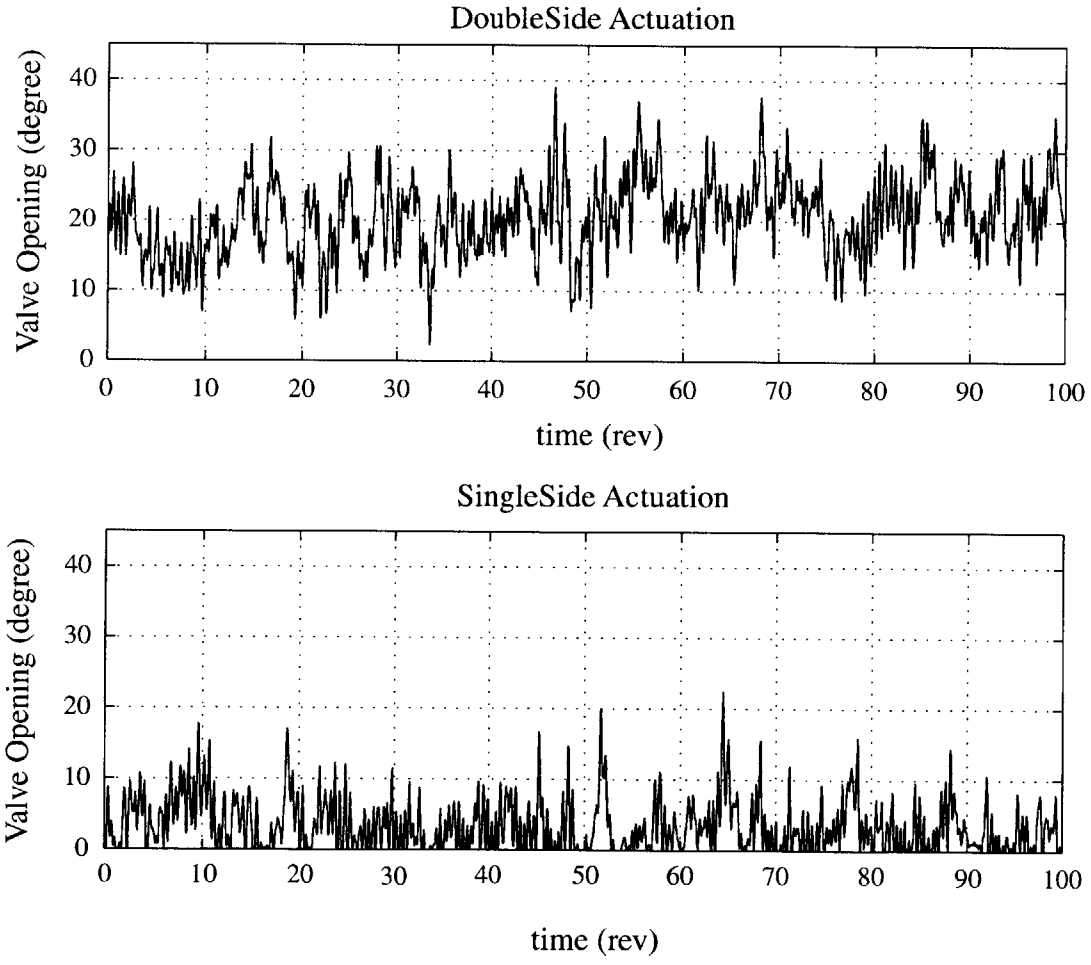


**Figure 4-7:** Actuation Level of One Bleed Valve

# Chapter 5

# Approximate Domain of Attraction for Clean Flow

In this chapter, the concept of nonlinear stability is introduced to characterize the degree of stability of an operating point. "Domain of attraction" is adopted to measure how far the system can be perturbed from a stable equilibrium and still return to its equilibrium point. Some simulations will show how we can use this new stability measure to better characterize the stability of the compression system. An experimental measurement of the approximate domain of attraction is also presented in this chapter. A plenum disturbance valve, as described in Chapter 2, was used to perturb the compression system. The approximate domain of attraction was measured first without control. Then a constant gain controller and a nonlinear sliding mode controller were implemented. The resulting approximate domain of attraction was measured to demonstrate enhancement of robustness of stability by active control.

## 5.1 Linear Stability vs Nonlinear Stability

As mentioned in Chapter 1, many researches of compressor stability and active control based on the linear theory have been successfully done [11, 19]. The basic assumption of linear analysis is that the disturbances are small. This implies that the linear analysis is only valid in a small vicinity of the equilibrium point. When

a nonlinear system is considered, the linear analysis is not enough to characterize the stability property of the system. The disturbances entering the system may be large enough to break the validity of the small disturbance assumptions. A nonlinear analysis is needed to better characterize the stability of the nonlinear system.

In the engine applications, both linear and nonlinear stability considerations have already been made. In the compressor map, the stall line (or surge line) actually marks the linear stability limit. A safety margin is also preserved in consideration of large amplitude disturbances. In order to run the compressor at a lower mass flow (for higher pressure ratio), we can use active control to extend the linearly stable operating range and thus shift the stall line to the left. This approach was demonstrated successfully by many researchers [19, 20]. The second approach targets making the operating points near stall line resist instabilities in the face of disturbances. This needs a more general stability analysis — nonlinear stability.

In order to explain nonlinear stability, we consider the one dimensional motion of a small ball on a curved surface, as shown in Figure 5-1(a). There are three

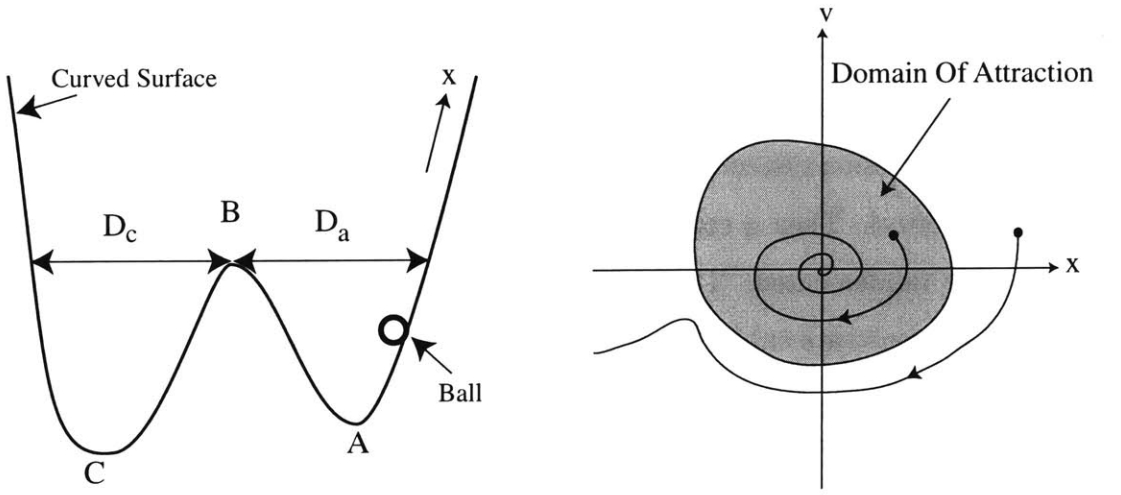


(a) Curved Surface

(b) Domain of Attraction of Point A

**Figure 5-1:** Nonlinear Stability: Motion on a Curved Surface

equilibrium points in this nonlinear system, labeled A, B and C. In linear sense, Points A and C are stable because the ball will return to the original point after

small perturbations, if we assume the motions are not frictionless. Point B is unstable. But in the nonlinear sense, if the perturbations become large enough, either Point A or Point C will lose stability. For example, if the ball starts at Point A and a large perturbation is added, the ball may go through Point B and finally come to equilibrium at Point C. The ball will no longer return to Point A. This example shows again that a linearly stable equilibrium point might not be stable when subject to relatively large disturbances. How far the system can be perturbed from Point A can be discussed in Figure 5-1(b), the phase plane. In Figure 5-1(b), axis x is the location of the ball along the curved surface with origin at Point A; axis v is the velocity of the ball. There is a region in the phase plane called the domain of attraction. If the perturbation is inside this region, the system will return to the equilibrium finally. Otherwise the system will no longer return to its original equilibrium. Mathematically the domain of attraction is defined as the largest set of points around the equilibrium such that trajectories initiated at these points will eventually converge to that equilibrium.

Mansoux [27] conducted a basic nonlinear stability analysis based on Lyapunov's indirect method. An estimate of the domain of attraction was also performed for the compression system model without unsteady losses. Based on this theoretical approach, she was able to obtain a set of conditions of allowable disturbances. However, choosing Lyapunov function candidates is still a difficult task. In the following section, numerical simulations will be performed.

## 5.2 Numerical Simulation of Nonlinear Stability

This section concentrates on the numerical simulations. First, the numerical simulation scheme is set up. The domain of attraction is estimated on the phase plane of the mean and first mode perturbations, resulting in a two dimensional region which we refer to as the approximate domain of attraction. Active control schemes are also applied to the simulations.

### 5.2.1 Simulation Setup

The Moore-Greitzer model is used to conduct the numerical simulations. There are two things which need to be clarified. First, even though the duct flow is linearized in the model, it was found that nonlinearities of the duct flow are relatively small even in the case of very large inlet distortions, as discussed in Hynes and Greitzer [22]. The model is qualified for our nonlinear simulations. Second, due to the complexity of the low mass flow regime and our incomplete knowledge of the compressor characteristic there, it is difficult to match the simulation results with the experimental data in this regime. The goal of the simulations is to capture the essential physics of the compression system in the moderate mass flow regime, where the stability analysis will be conducted, and where active control will be implemented. The extremely low flow regime is outside our interest.

The model derived in Chapter 3 will be used for numerical simulations. The following model parameters are used. For the so-called "actual" compressor charac-

**Table 5.1:** Model Parameters

| | | |
|---|---|---|
| $U = 72$ m/s (at 2400 rpm) | $\mu = 1.2937$ | $\lambda = 0.95$ |
| $R = 0.287$ (mean wheel radius) | $l_c = 7.0$ | $\tau = 0.3$ |
| $r = 0.738$(rotor reaction) | $l_b = 1.0$ | $m = 2$ |

teristic, we use

$$\psi_c(\phi) = \begin{cases} -10.2495\phi^2 + 9.4301\phi - 1.1848, & \phi > 0.4 \\ 1.5594\phi^3 - 1.9175\phi^2 + 2.0\phi + 0.3511 & 0 < \phi < 0.4 \end{cases} \tag{5.1}$$

The ideal compressor characteristic is taken to be [15]

$$\psi_i(\phi) = -15.5341\phi^3 + 24.1238\phi^2 - 15.0262\phi + 4.6951; \tag{5.2}$$

A typical stall transient was simulated and compared with the experimental data in Figure 5-2. Figure 5-2(a) shows the hot wire traces of experimental data and the corresponding simulation results. The stall inception in the simulation is very similar to the experiment. Figure 5-2(b) shows a good match of mean mass flow between experiment and simulation. These results combined with the results of Chapter 4, give us confidence that the numerical simulation will be suitable for our purposes of investigating nonlinear properties of the compression system.

### 5.2.2 Approximate Domain of Attraction

The compression system has an infinite number of degrees of freedom theoretically because there are infinite number of spatial modes (or harmonics). As a result, the domain of attraction is a multi-dimensional domain, which is impossible to calculate numerically. However, it is practically unnecessary to calculate all the dimensions, because the projections of the domain of attraction on most axes are very large or infinite. To simplify the characterization of domain of attraction, we will look only at its projection on a two dimensional plane. As observed by many researchers [19, 20, 15], the lower spatial modes, especially the zeroth and first spatial modes, are dominant in a low speed compressor like the MIT three stage compressor. For stability, these lower spatial modes are more critical. Furthermore, the plenum pressure is not important as described by Mansoux [27]. So a two dimensional (the zeroth and first modes) description will be used to characterize the real domain of attraction.

To obtain the approximate domain of attraction of the compression system, the throttle setting is first chosen and fixed. The equilibrium operating point at this throttle setting is calculated. Then a combination of the mean mass flow perturbation and first spatial mode perturbation are superimposed on the equilibrium point. The simulation is started to see whether the system returns back to the chosen equilibrium operating point. According to the resulting stability, a boundary can be determined on the plane of the mean perturbation and the first mode amplitude. The system sustains stability with disturbance combinations inside this boundary. So the region

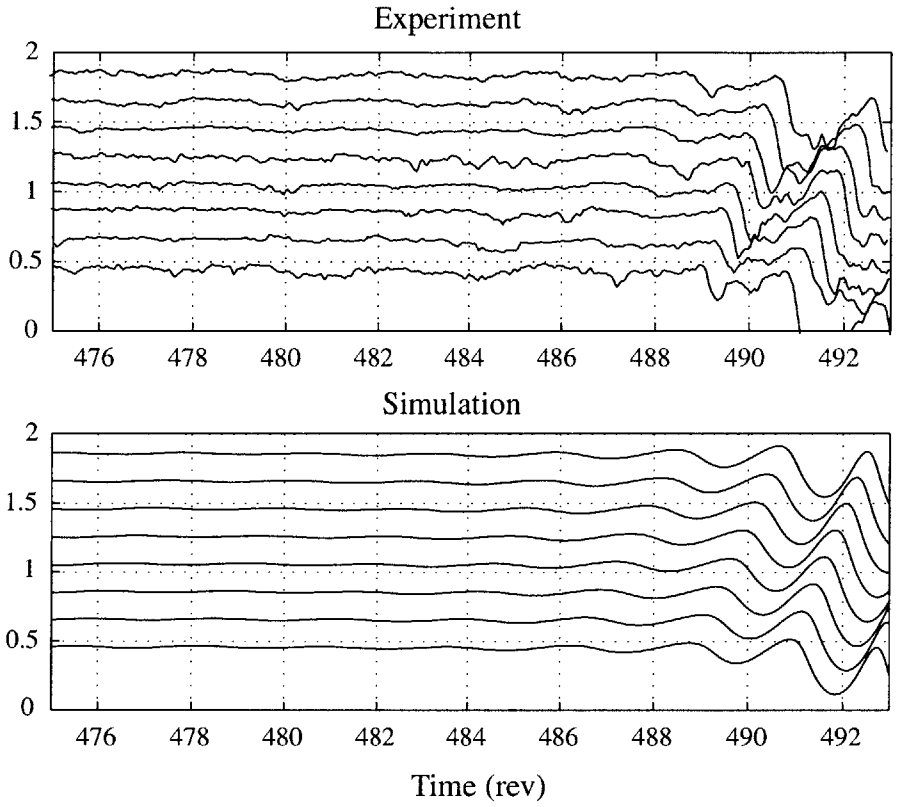


(a) Comparison of Hot Wire Traces

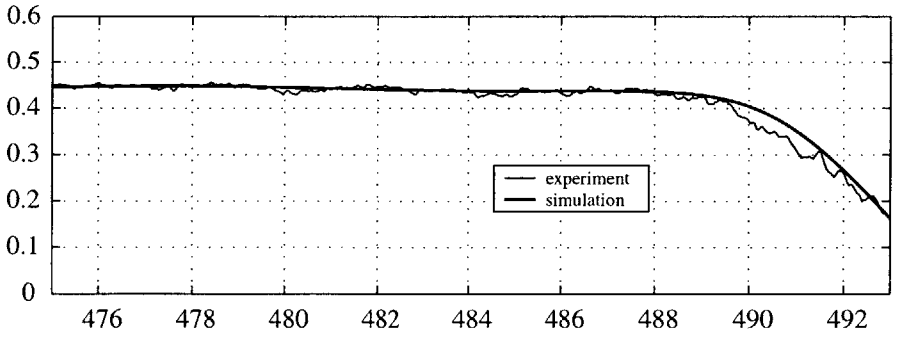


(b) Comparison of Mean Mass Flow

**Figure 5-2:** Comparison of Simulation Results and Experimental Data

under this boundary is the approximate domain of attraction. In simulations, we only concern ourselves about negative mean flow perturbations. Figure 5-3 shows the calculated approximate domain of attraction at equilibrium point $\phi_e = 0.4675$. In

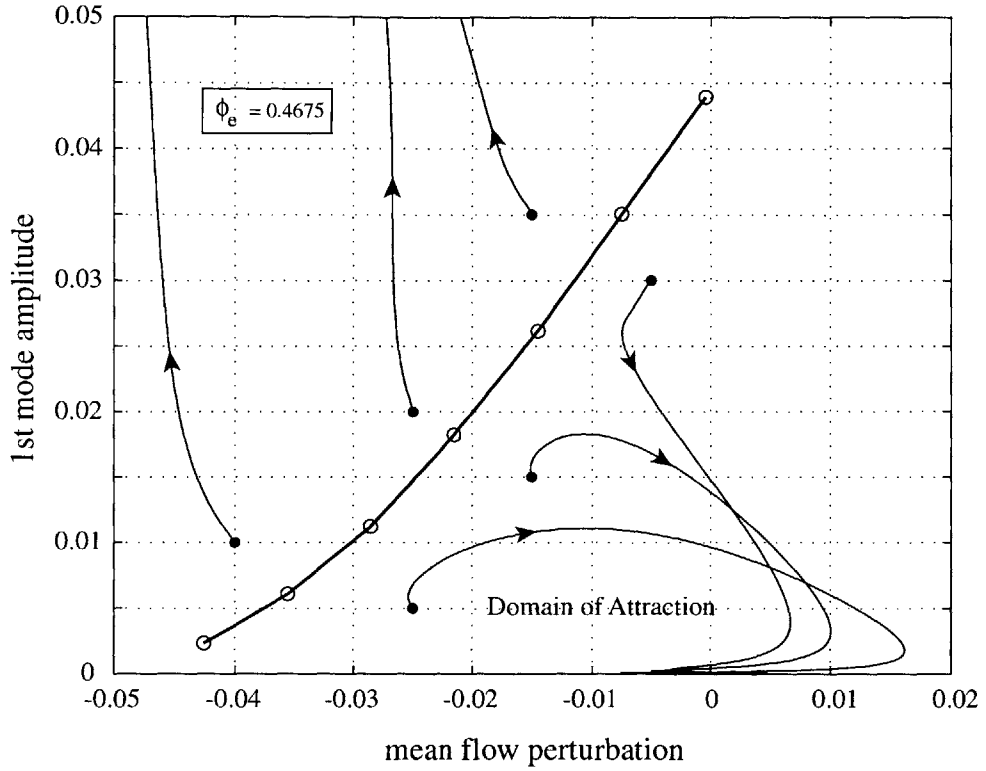


**Figure 5-3:** Simulated Approximate Domain of Attraction at $\phi_e = 0.4675$

the figure, the circles on the boundary represent the points the simulations run on. There are also six transients. Three of the transients initiated from the points under the boundary, return back to the origin. The other three just go into rotating stall. On the two axes, the boundary lies at around 10% of the mass flow at the equilibrium point.

### 5.2.3 Parametric Studies of the Domain of Attraction

In order to better understand the domain of attraction, this section shows how it depends on the mean mass flow and model parameters. Three cases are shown in the following results.

**Domain of Attraction vs Mass Flow** As we know in linear analysis, the stability is closely related to the slope of the compressor characteristics. Normally, higher mass flow means more "negative" slope of the compressor characteristic, which implies more damping associated with the corresponding operating point. It is interesting to see whether this damping will affect the domain of attraction. Table 5.2 lists the equilibrium points used for simulations.

**Table 5.2:** Equilibrium Points Used for Simulations

| $K_t$ | $\phi_e$ | $\psi_e$ |
|---|---|---|
| 9.3 | 0.4601 | 0.9843 |
| 9.0 | 0.4675 | 0.9837 |
| 8.7 | 0.4751 | 0.9819 |
| 8.4 | 0.4828 | 0.9789 |
| 8.1 | 0.4906 | 0.9747 |
| 7.8 | 0.4985 | 0.9691 |
| 7.5 | 0.5065 | 0.9621 |

The simulation results are shown in Figure 5-4. When mass flow increases by opening the throttle, the domain of attraction increases. This was also demonstrated by Mansoux [27]. As equilibrium mass flow moves from $\phi_A$ to $\phi_B$, the size of approximate domain of attraction should increase by at least $(\phi_B - \phi_A)$. Larger increases are due to the increase of damping. Figure 5-5 shows the maximum allowable mean flow perturbation amplitude and maximum allowable first mode perturbation versus equilibrium mass flow. The dotted line is the mass flow increases over the reference $\phi = 0.4556$ (the stalling mass flow). The dashed line is steeper than the dotted line. The increase of maximum allowable perturbations is greater than the mass flow increase over different equilibrium points. We also note that the maximum allowable first mode perturbation increases more than the maximum allowable mean perturbation when mass flow increases, which implies that the first mode is more sensitive to the equilibrium mass flow even in the nonlinear sense (refer to Figure 4-5).

**Domain of Attraction vs B Parameter** In the linear analysis, the B parameter plays an important role in the surge dynamics, but not in the rotating stall

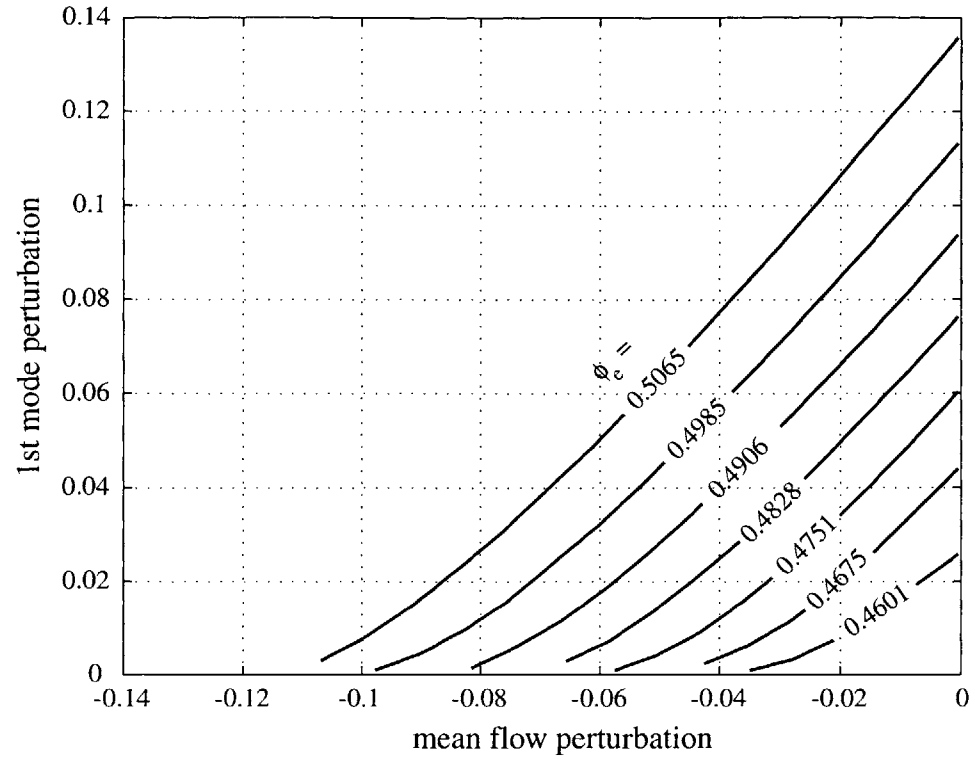


**Figure 5-4:** Domain of Attraction vs Mass flow

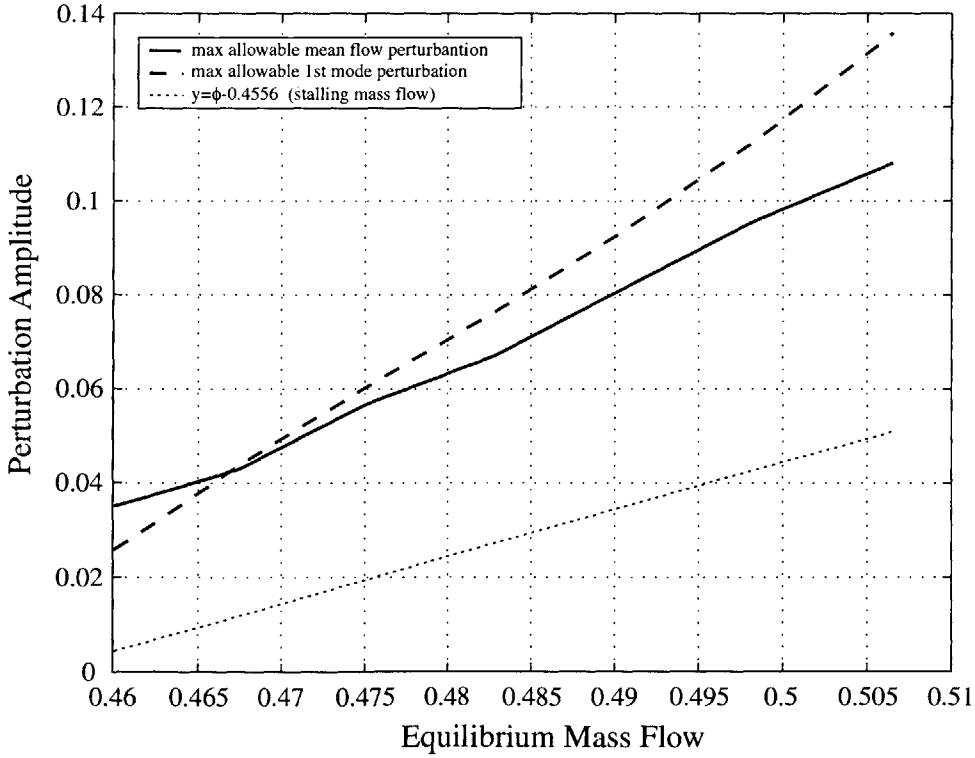


**Figure 5-5:** Maximum Allowable Perturbations vs Mass flow

dynamics. However, surge and rotating stall are coupled in the nonlinear system. Figure 5-6 shows how the B parameter affect the domain of attraction. Both maximum

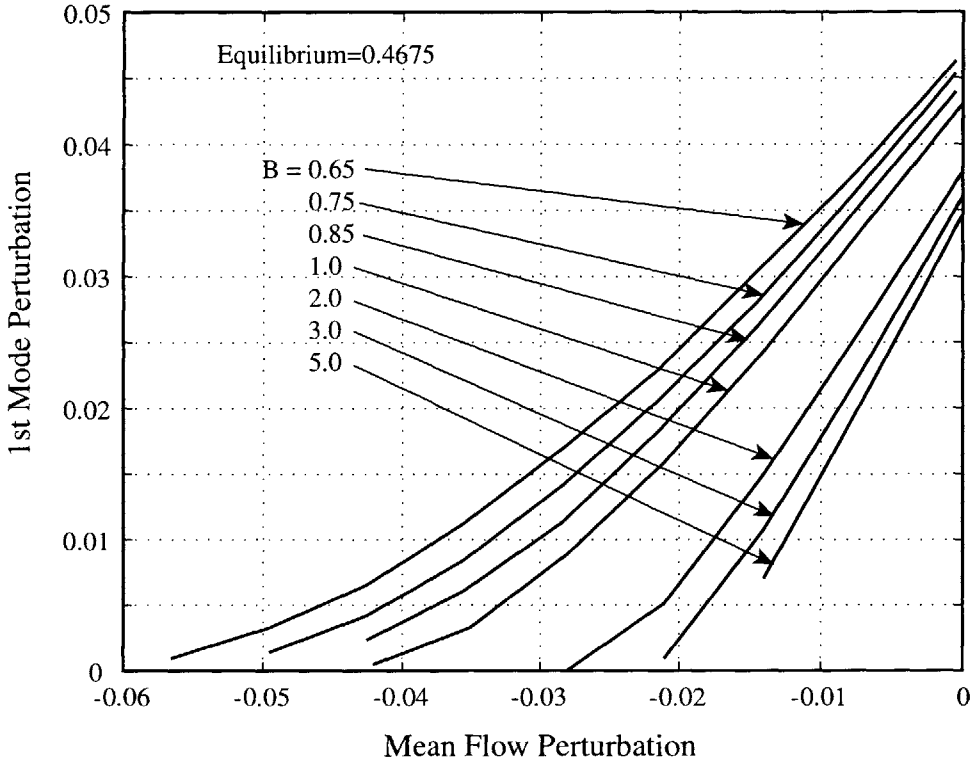


**Figure 5-6:** Domain of Attraction vs B parameter

allowable mean and first mode perturbations increase when B parameter decreases. Also maximum allowable mean perturbation increases more than first mode perturbation when the B parameter decreases. This means that the B parameter is still more important to surge mode than rotating stall modes, even when viewed from the nonlinear perspective.

**Domain of Attraction vs Unstable Part of Characteristics** In linear analysis, the stability of a stable operating point has nothing to do with the unstable part of the compressor characteristic. Linear stability is only dependent on the local slope of the characteristic. Nonlinear stability, however, is very different since perturbations are no longer assumed small, the system may be perturbed far from it equilibrium point. Then the part of the compressor characteristic far from the equilibrium point could be very important in determining how the system trajectories

will go and therefore its stability.

Figure 5-7 shows changes in the domain of attraction due to changing the unstable part of the compressor characteristic. As the unstable part of the characteristic becomes steeper, the approximate domain of attraction becomes smaller. This implies that the unstable part of the characteristic plays an important role in the disturbance-resisting ability of the compression system. Based on this, the following example will illustrate why nonlinear stability is important. As shown in Figure 5-8, the circle represents the linear stability limit. On the left of this point, the system is linearly unstable. On the right of this point, the system is linearly stable. In a manner similar to the way the stall margin is typically set, we assume the compressor runs at a mass flow 15% higher than the linear stability limit. Assume now that a disturbance comes into the system, causing a first mode perturbation of about 40% of this operating mass flow. Stability limits were examined for three different unstable parts of the characteristic. Point A (diamond) is the stability limit for characteristics A. As the unstable part of characteristics becomes steeper, the stability limits move to higher mass flows, as indicated by point B and C. This means that stability limits are different for different unstable parts of the characteristic. So a simple 15% stall margin is not enough to describe the safety margin when there are strong disturbances. Two compressors with the same stable characteristic shape but different unstable shape might be assigned the same stall margins, although they should be different for these two. So, without knowledge of the unstable part of the characteristic, traditional stall margin procedures are not meaningful. Nonlinear characterization of the stability of the compression system, i.e. domain of attraction, is therefore necessary.

From the parametric studies, we see that the approximate domain of attraction is relatively large at higher mass flows (Figure 5-4). This index can be used as a measure of how much stall margin the operating points need. Also the approximate domain of attraction does not change much when B parameter changes from 0.65 to 1.0, especially the maximum allowable first mode amplitude (Figure 5-6). The approximate domain of attraction is sensitive to the unstable part of the compressor

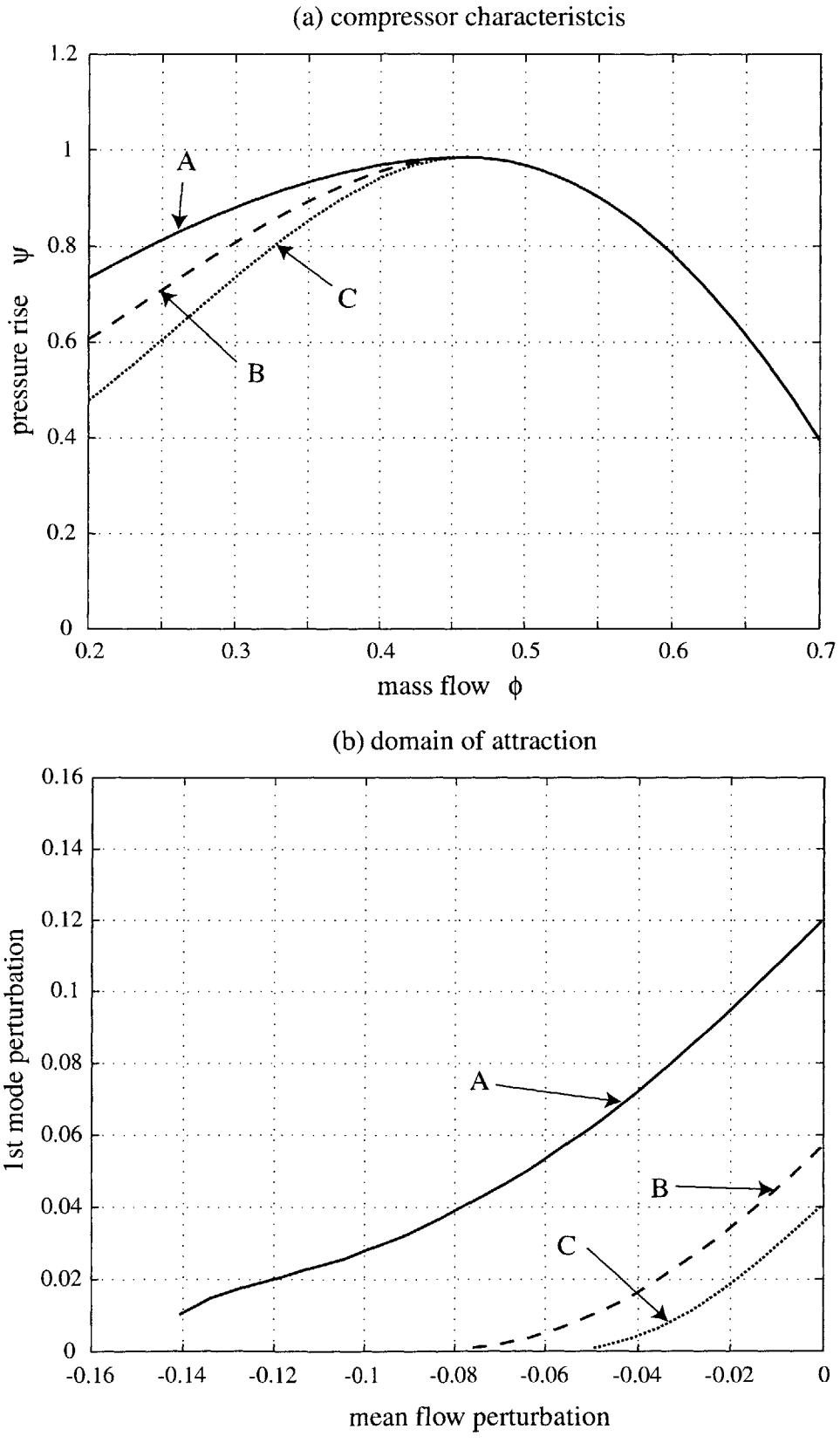


**Figure 5-7:** Domain of Attraction vs Unstable Part of Characteristics

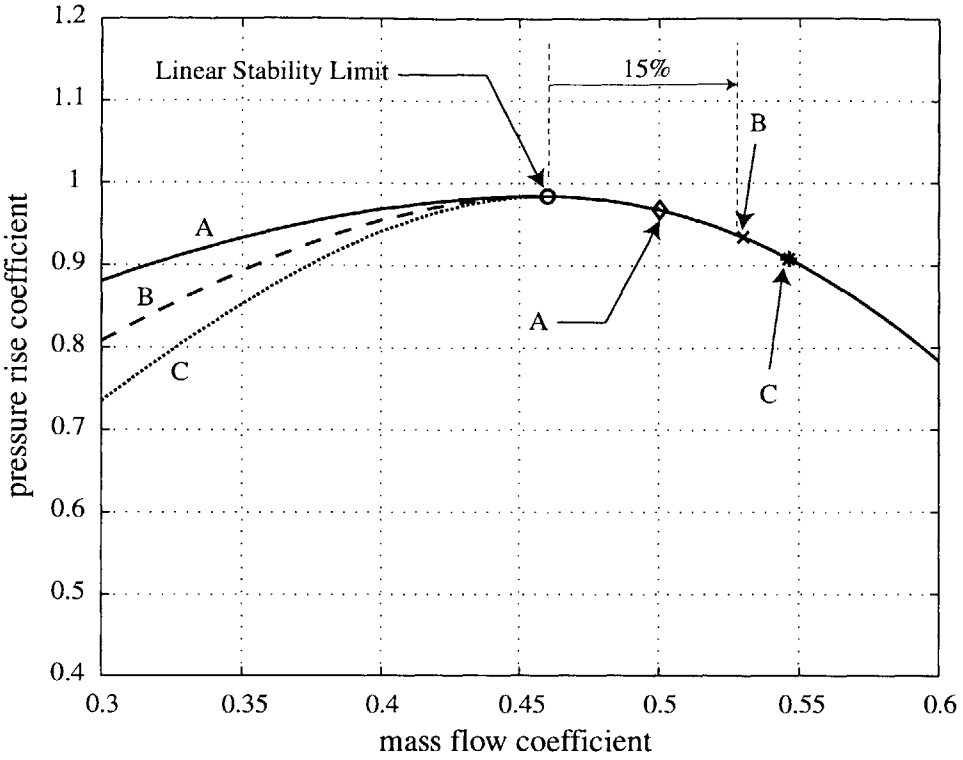


**Figure 5-8:** Stability Limit Under Disturbances

characteristic. If the unstable part of the compressor characteristic is very steep, the approximate domain of attraction (disturbance rejection) tends to be small (Figure 5-7). This means that a fixed number of stall margin for different compressors is not appropriate. Generally the domain of attraction provides more detailed information of the system stability, and therefore is a better measure of compressor stability.

### 5.2.4 Active Control Schemes

In order to examine how active control can improve the domain of attraction of compressor operating points, both constant gain and nonlinear controllers are considered. Because there is no systematic design method targeting improvement of domain of attraction, a constant gain control was therefore first chosen for its simplicity and its effectiveness in extending the operating range.

Because of the nonlinear nature of the domain of attraction, linear controllers may

be not effective if the system transients go beyond the valid region of linearization. Nonlinear controllers are naturally good choices for this purpose. Sliding mode control design provides a systematic approach to the problem of maintaining stability in the presence of modeling imprecisions. It also provides an intuitive physical picture of the control process which is very useful in controlling nonlinear systems. The controller normally consists of a nominal part, similar to a feedback linearization or inverse control law, and of additional terms aimed at dealing with model uncertainties.

**Constant Gain Controller** The constant gain controller is the same as the one used for range extension. It consists of a 0th mode controller and a first mode controller as described in Chapter 4. The 0th and first mode control are not coupled. Single-sided actuation is used in simulations to reduce the nominal bleed level.

**Sliding Mode Controller** The model used for sliding mode controller design does not include unsteady losses, because real-time implementation of the high order controllers that would result is not realistic. From Equation (3.19), we have the following model:

$$\begin{cases} E\dot{\underline{\phi}} = -A\underline{\phi} + \phi_c(\underline{\phi}) - T\psi + \underline{\Psi}_{dist} + (S^T\underline{\phi})\mathcal{F}\underline{u} + \mathcal{G}\mathcal{F}\dot{\underline{u}} \\ \dot{\psi} = \dfrac{1}{4l_cB^2}\left[S^T\underline{\phi} - S^T\mathcal{F}\underline{u} - \sqrt{\dfrac{2}{K_t}\psi}\right] \end{cases} \tag{5.3}$$

This model can also be written into matrix form:

$$E_\phi\dot{\underline{w}} = E_A\underline{w} + f(\underline{w}) + E_u\underline{u} + E_d(\underline{w})\dot{\underline{u}} \tag{5.4}$$

Where

$$E_\phi = \begin{pmatrix} E & 0 \\ 0 & \beta \end{pmatrix}, \quad E_A = \begin{pmatrix} -A & -T \\ S^T & 0 \end{pmatrix}, \quad \underline{w} = \begin{pmatrix} \underline{\phi} \\ \psi \end{pmatrix}, \quad \beta = 4l_cB^2$$

$$f(\underline{w}) = \begin{pmatrix} \psi_c(\phi) \\ -\sqrt{\dfrac{2}{K_t}\psi} \end{pmatrix}, \quad E_u(\underline{w}) = \begin{pmatrix} (S^T\underline{\phi})\mathcal{F} \\ -S^T\mathcal{F} \end{pmatrix}, \quad E_d = \begin{pmatrix} \mathcal{G}\mathcal{F} \\ 0 \end{pmatrix}$$

Assume the equilibrium point of interest is $\underline{w}^*$. Write the perturbation as

$$\underline{\tilde{w}} = \underline{w} - \underline{w}^*, \quad f(\underline{w}^*, \underline{\tilde{w}}) = f(\underline{w}) - f(\underline{w}^*), \quad E_u(\underline{w}^*, \underline{\tilde{w}}) = E_u(\underline{w}) - E_u(\underline{w}^*)$$

Then the perturbation equation can be written as follow

$$E_\phi \dot{\underline{\tilde{w}}} = E_A \underline{\tilde{w}} + f(\underline{w}^*, \underline{\tilde{w}}) + E_u(\underline{w}^*, \underline{\tilde{w}})\underline{u} + E_d \dot{\underline{u}} \tag{5.5}$$

The above equation is exactly the same as Equation (5.4) except that it is written in perturbation form. No linearization is performed in Equation (5.5). Define

$$\underline{\tau} = E_u(\underline{w}^*, \underline{\tilde{w}})\underline{u} + E_d \dot{\underline{u}} \tag{5.6}$$

We can have a sliding mode controller of the form

$$\underline{\tau} = -\hat{f}(\underline{w}^*, \underline{\tilde{w}}) - \hat{E}_A \underline{\tilde{w}} - \underline{k} sat(\underline{\tilde{w}}/W) \tag{5.7}$$

where $\hat{f}$ and $\hat{E}_A$ are estimates of $f$ and $E_A$ respectively, by considering model uncertainties. $\underline{k}$ is a gain matrix. $W$ is a factor for smoothing purposes. $sat(y)$ is defined as

$$sat(y) = \begin{cases} sign(y), & |y| > 1, \\ y, & |y| \leq 1 \end{cases}$$

Details on the controller design can be found in Appendix C.

**Actuation Saturation** For a constant gain controller, the 0th and first mode controls are decoupled, so the saturation level is divided into two portions for these two mode controls respectively. We denote the saturation level for the 0th mode control as $\mathcal{S}_0$, the one for the first mode control as $\mathcal{S}_1$. The ratio of $\mathcal{S}_0/\mathcal{S}_1$ can be changed to study which one is important for our purpose. For sliding mode control, the controls for all modes are coupled. No division of saturation level is needed. From this, we can expect that the sliding mode control will better use the saturation and hopefully have better control effectiveness.

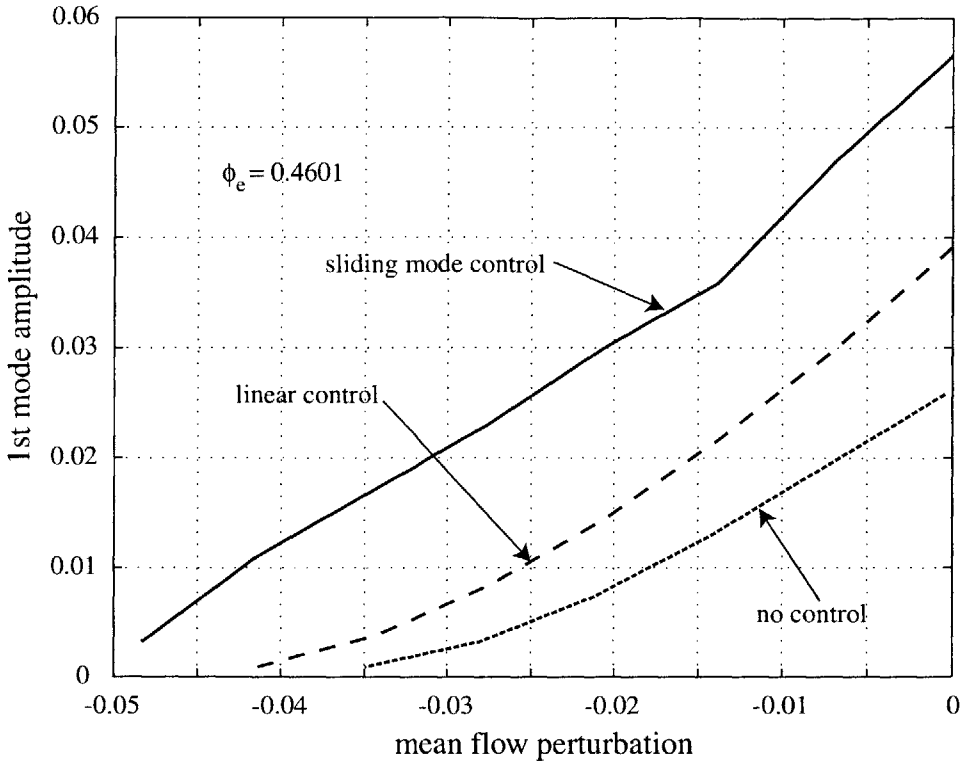


**Figure 5-9:** Simulation Results of Active Control

### 5.2.5 Simulation Results of Active Control

Figure 5-9 shows both the constant gain and sliding mode control results. The constant gain controller (designed for range extension) is still effective in enhancing robustness of stability. The maximum allowable first mode perturbation increases from 5.6% to 8.5% of the equilibrium mass flow ($\phi_e$), which is 51% enhancement. The sliding mode control achieves even more enhancement. The maximum allowable first mode perturbation increases up to 12.3% of the equilibrium mass flow, more than doubling the open loop value. As we expected in Section 5.2.4, the sliding mode design couples the zeroth and first mode feedback. Therefore it provides better feedback and also better use of the saturation level of the actuation. Figure 5-10 compares the maximum allowable first mode perturbations at different throttle settings (different $\phi_e$). The controllers are effective at all mass flows.

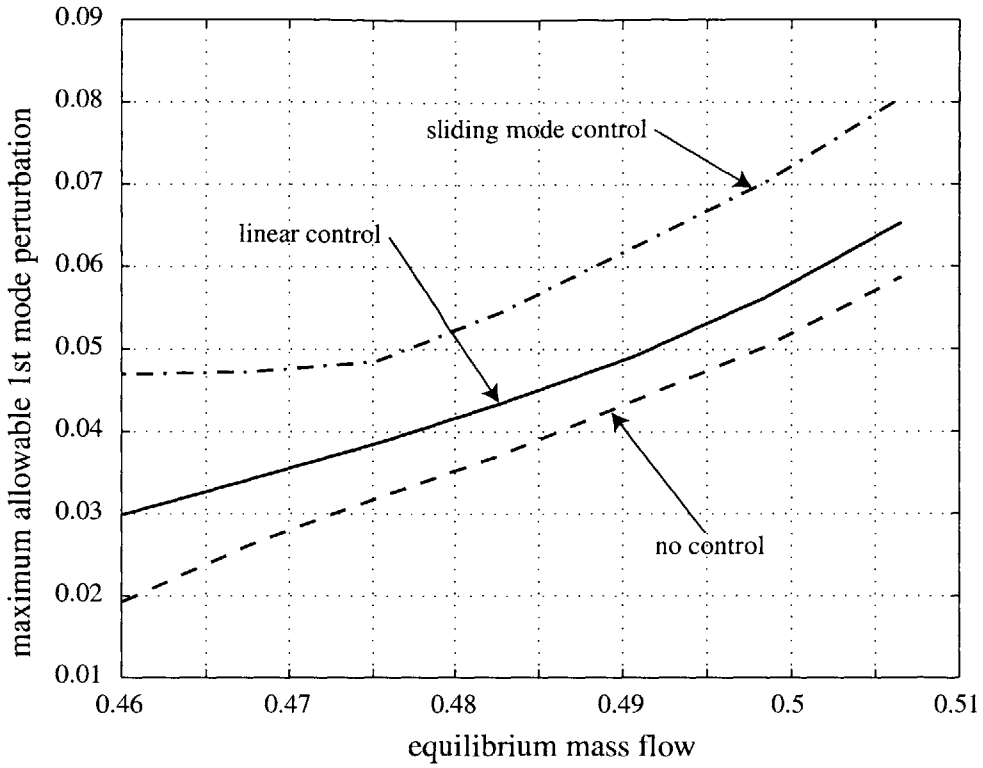


**Figure 5-10:** The Maximum Allowable First Mode Perturbations At Different Equilibrium Mass Flow

### 5.2.6 Parametric Studies of Active Control

Numerical simulation is a good way to do parametric studies which are usually difficult in experiments. In this subsection, several constant gain control parameters are examined. First, different saturation ratios between the zeroth and first mode control are simulated to see which mode is more important for domain of attraction. Second, different overall saturation levels are examined to see how much the saturation limits the control effects.

**Saturation Ratio** The following cases are simulated and compared: the first mode control only, the zeroth mode control only and the combined mode control which is referred to as "constant gain control" ($Sat_0/Sat_1 = 1/2$). Figure 5-11 shows the results. It is shown that the approximate domain of attraction is still enlarged with only the zeroth mode control. This is because the mean bleed moves the operating points to higher mass flows and therefore provides more damping to disturbances.

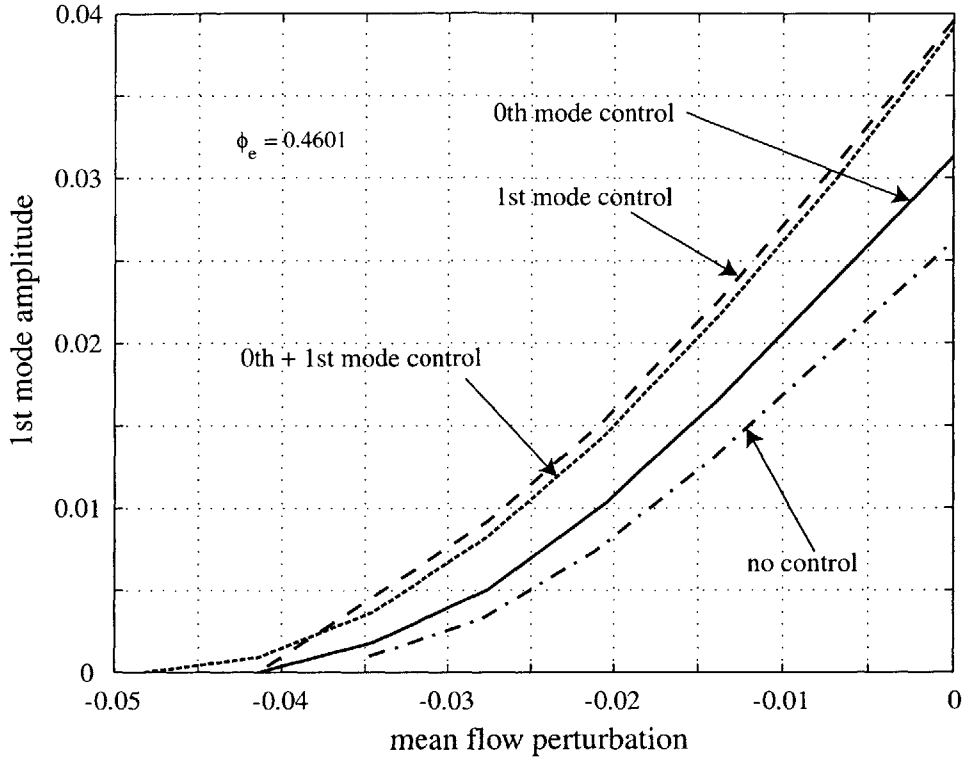


**Figure 5-11:** Comparison of Saturation Ratios

Also the pure first mode control is better than the pure zeroth mode control. The combined mode control has better effects in the low first mode amplitude region than the pure first mode control. So suppressing the first mode disturbances is more important in enhancing the robustness of stability.

**Saturation Level** Different saturation levels are also compared as shown in Figure 5-12. The saturation levels used for comparison are one, two, four and six times of the actual saturation. Apparently, increasing the saturation level enlarges the approximate domain of attraction significantly. The maximum allowable first mode perturbation benefited more from increasing saturation, because it is more important as mentioned above.

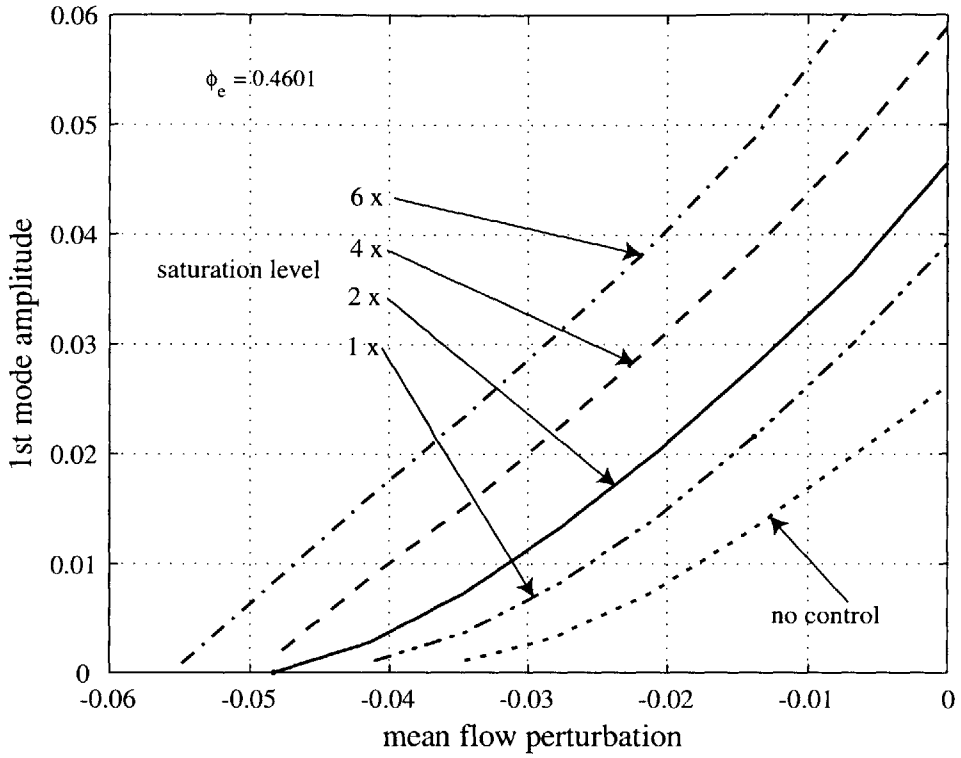


**Figure 5-12:** Effect of Saturation Level on Domain of Attraction

## 5.3 Disturbance Generation

In order to characterize the domain of attraction, disturbances should be generated to drive the system away from its equilibrium point. A plenum disturbance valve was designed as described in Chapter 2. This section describes the perturbation procedure.

The perturbations generated by a plenum valve are actually one dimensional (axial direction). To be able to induce first mode perturbations as well, the mean mass flow must be perturbed below the stalling mass flow. Otherwise, the damping of the system is too high to let the first mode grow. To do this, the equilibrium point is chosen close enough to the stall point so that the system is easy to perturb into low mass flow region. As indicated in Haynes [20], the mass flow measured from bellmouth has relatively large variation (1.77%) from day to day. To ensure the same operating point on different days, the stalling mass flow was measured each day. The mass flow of the equilibrium point of interest was determined to be a fixed percent

higher than the stall mass flow. In the following experiments, the fixed percentage is 2%.

The perturbation procedure is illustrated in Figure 5-13. Point A is the equilib-

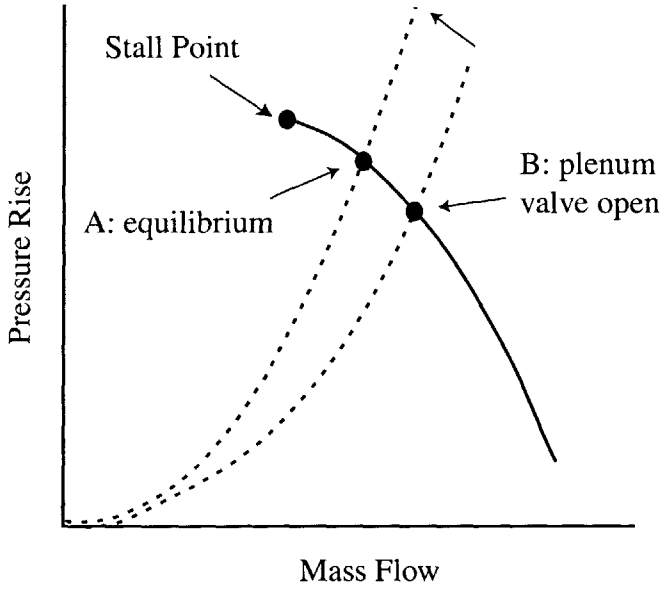


**Figure 5-13:** Schematic of Perturbation Procedure

rium point chosen which is close to stall point. The main throttle of the compression system is fixed. Opening the plenum disturbance valve is equivalent to effectively moving the throttle line to point B. In experiments, the throttle is first positioned such that point A is reached. The plenum disturbance valve is then opened. The system equilibrates at point B. Finally we close the plenum disturbance valve suddenly. A transient occurs, causing the mean mass flow to undershoot the equilibrium mass flow, briefly visiting mass flow below the stall point. As we can see in Figure 5-14, the first spatial mode grows during this transient. Depending on whether the perturbations go beyond the domain of attraction, the system can either return to the desired equilibrium point or go into rotating stall. Because the first mode is randomly excited, it will provide a number of possible perturbation transients. Then we can use these transients to estimate the approximate domain of attraction.

A typical run is shown in Figure 5-14. The result shows a run that remains stable after the perturbation. The data were filtered by a rotating filter as described

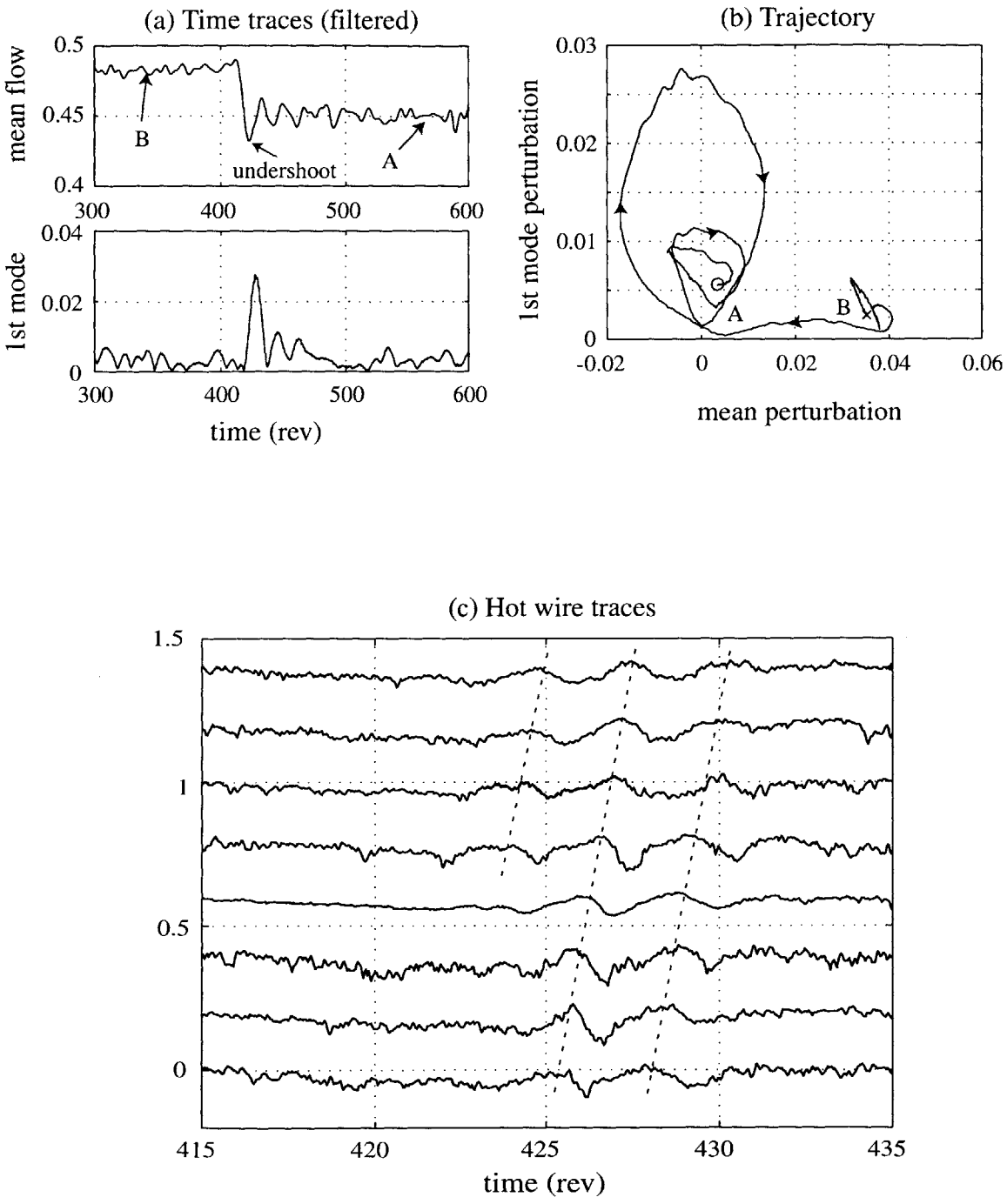


**Figure 5-14:** A Typical Run of Perturbation

in Section 2.3.2 and Appendix A. In Figure 5-14(a), time traces of mean mass flow and first mode amplitude are plotted. After perturbation from the open-disturbance-valve point B, the mean mass flow undershoots the equilibrium point A. The system then returns to point A after several oscillations. The bottom plot in part (a) clearly shows that the first mode grew to a significant level and then returned back to the noise level. Figure 5-14(b) shows the trajectory on the phase plane of mean mass flow and first mode amplitude. The origin represents point A, which is our equilibrium point of interest. The trajectory represents a solution of the system differential equations which should belong to the domain of attraction of point A. Figure 5-14(c) clearly shows the induced first mode in the hot wire traces.

The perturbation method described above is very simple and easy to implement. It is able to produce both zeroth and first mode perturbations. But there are still penalties. Because the perturbation is actually one dimensional, the first spatial mode excitation and growth can not be directly tuned. The first spatial mode is randomly excited by environmental noise (e.g. fluctuations in the flow field). A number of runs are needed to cover as much of the region of the domain of attraction as possible. When active control is applied, the time period before the control is turned on, is tunable to let the first mode have more chances to grow. The details will be presented later.

## 5.4 Experiment Results of Domain of Attraction for Open Loop System

In this section, the approximate domain of attraction determination method will be described. Then experimental results of the approximate domain of attraction are shown.

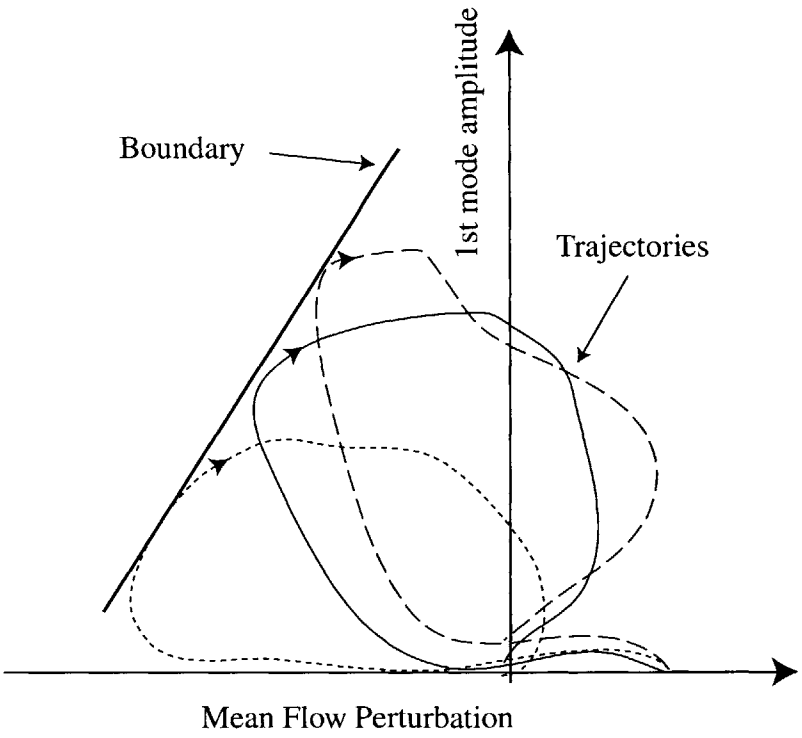


**Figure 5-15:** Determination of Domain of Attraction

### 5.4.1 Experimental Determination of Domain of Attraction

For the specific perturbation method we used, the domain of attraction can not be measured directly. As we described above, the growth of the first spatial mode can not be directly tuned. The trajectories of the perturbation transients are usually different for different runs due to the uncertainty of the excitations. However, if there are enough different runs, we are able to use the envelop of these trajectories of stable runs to approximate the domain of attraction.

Figure 5-15 show how the approximate domain of attraction was determined. Three trajectories are plotted. A boundary is found which envelops all of these stable trajectories as closely as possible. In the real data processing, the outermost segments of these trajectories were connected together to represent the boundary of domain of attraction. This is at worst a conservative estimate of the domain of attraction in which the trajectories initiated will converge to the desired equilibrium point.

For open loop runs, it is impossible to determine whether our estimate of the

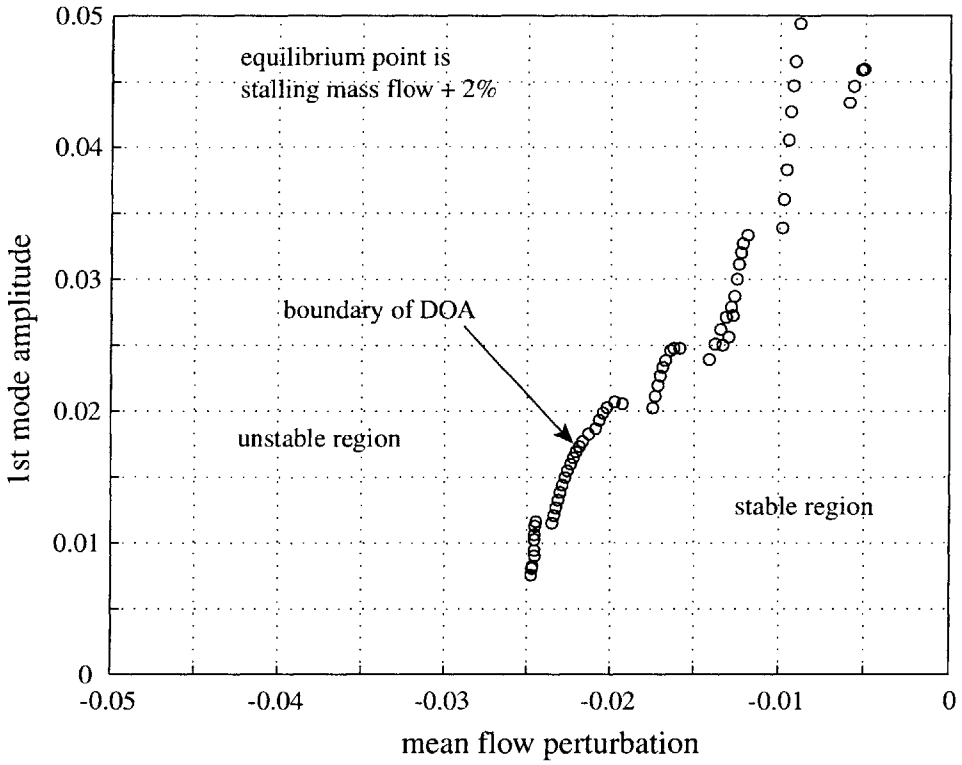


**Figure 5-16:** Experiment Result of Domain of Attraction for Open Loop System

domain of attraction is close to the real value. However, the unstable trajectories of the control runs will provide a way to verify the validity of these tests. In the control runs, the time when control is turned on can be recorded. The control-on point of a trajectory — the point when the control is turned on — is then examined to see whether it is located outside the boundary of the domain of attraction.

### 5.4.2 Domain of Attraction for Open Loop System

The measured approximate domain of attraction is shown in Figure 5-16. In the figure, the circles represent the experimental boundary of the approximate domain of attraction. Any perturbation falling inside the region enclosed by this boundary will return to the equilibrium point. Those perturbations going beyond the domain of attraction will drive the system to instability (rotating stall for our case).

In experiments, we found that there are fewer data points falling in the region

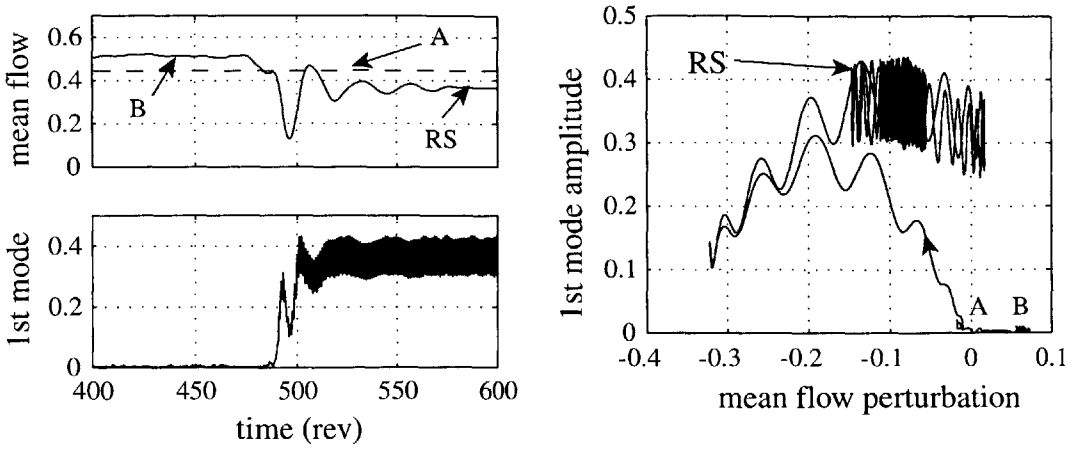


**Figure 5-17:** An Unstable Perturbation

which has smaller mean mass flow perturbation and larger first mode amplitude. The reason is that the first mode disturbances were induced only where the mean mass flow undershot enough beyond the stalling mass flow. In the smaller mean mass flow perturbation region, the first mode disturbances are relatively highly damped. The following experiments experience a similar situation.

Figure 5-14 shows the time traces of mean flow perturbation and first mode amplitude, as well as the trajectory in the phase plane. Figure 5-17 shows a run which finally went into rotating stall after perturbation. In the figure, point B represents the equilibrium point with plenum disturbance valve open, while point A represents the desired equilibrium point, as shown in Figure 5-13. The desired equilibrium point is taken as a reference point which is located at the origin of the phase plane. The first mode induced by the perturbation grows to a fully developed rotating stall. As we can see, the final value of the mean flow is lower than the desired equilibrium value. The label "RS" represents the fully developed rotating stall point.

## 5.5 Experiment Results of Active Control

In this section, two controllers used in the experiments are introduced, including some practical considerations. Then the control results are presented to demonstrate

enhancement of the robustness of compressor operation through active control.

### 5.5.1 Controllers

The controllers used for active controls were introduced in Section 5.2.4. Here more implementation details are summarized.

The constant gain controller used here is exactly the same as the controller used in Chapter 4. This controller was tuned to obtain the best range extension result. Because our purpose is to demonstrate the ability of this controller — which is designed for range extension — to enhance the robustness of compressor operations, no further tuning is performed. Total saturation level is divided between the zeroth and first mode control as described in Section 5.2.6.

For the sliding mode controller, more parameters need to be determined. Compressor characteristics and other rig specific parameters are the same as those used in the simulations. The control gains and phases were tuned to obtain the best range extension, because tuning control parameters to maximize the approximate domain of attraction — which is a two dimensional property — would be extremely time-consuming. There is another thing worth mentioning. The states needed by sliding mode control are directly calculated from hot wire and pressure sensor measurements. This is one advantage of the distributed compression system model, where the system states consist of local mass flow and the plenum pressure. The hot wire measurements were first filtered by a rotating filter (see Chapter 2 and Appendix A) before they entered the calculation of sliding mode control. Otherwise the measurement noise will enter the nonlinear operations performed by the controller algorithm, which will generate unexpected results.

The time period between closing the disturbance valve and turning control on is also tunable on line. This allows the first mode to have enough time to grow before it is suppressed by control.

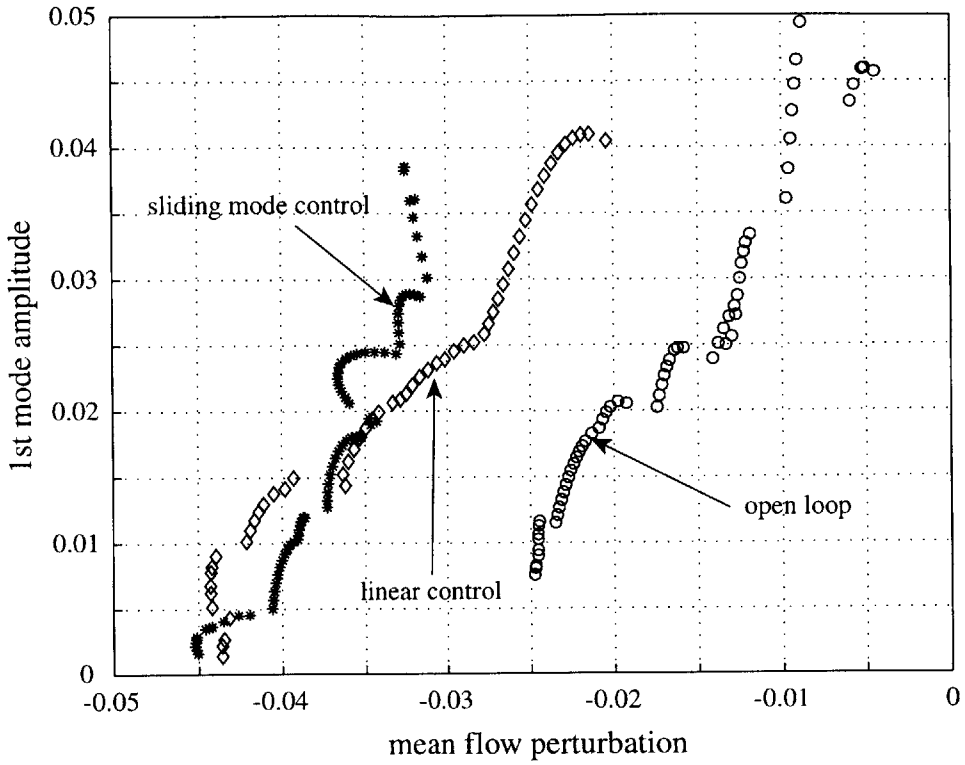


**Figure 5-18:** Domain of Attraction with Active Control

### 5.5.2 Domain of Attraction with Active Control

The results of the domain of attraction experiments with active control are shown in Figure 5-18. The approximate domain of attraction of the open loop system is also plotted for reference. The diamonds represent the results with constant gain control. The allowable first mode disturbances for a given mean flow perturbation are about twice those of the open loop system. The maximum allowable mean flow perturbation also increases to about twice the open loop case. In conclusion, the constant gain controller designed for range extension also shows an ability to enhance the approximate domain of attraction.

The result for sliding mode control is also plotted in the figure. In the region of high mean flow perturbation, the controller is less effective than constant gain control. In the region of high first mode amplitude, the sliding mode control is more effective than constant gain control. The success of the sliding mode control is encouraging, because the control is completely model based. Another point is that the actuation is

considered discrete. Instead of trying to generate sinusoidal waves, each bleed valve was commanded according to the desired feedback. The effect of sliding mode control is not as good as shown in the simulations. This may be because the effect of sliding mode control relies on the accuracy of the system model — even though it can deal with model uncertainty to some extent. There are more model uncertainties in the experiments than in the simulations, where the exact system model is used in the control law.

### 5.5.3 Transient Behavior of Active Control

Figure 5-19 shows a stable transient with constant gain control. In the mean

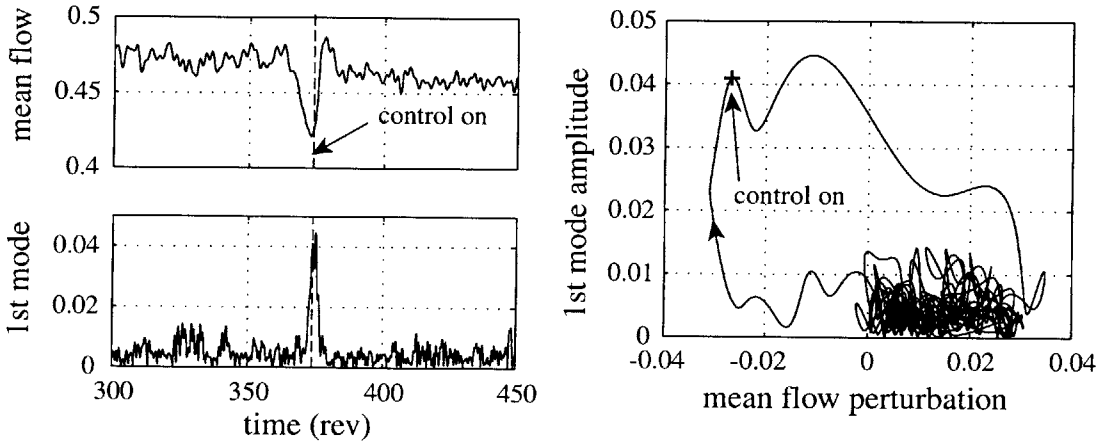


**Figure 5-19:** Stable Transient With Constant Gain Control

flow trace, there are fewer oscillations after the control is turned on (the dashed line represents the time when control is turned on) . The actuation also causes the mean flow to overshoot. The first mode plot shows that the control is turned on near the peak. The trajectory in the phase plane is shown on the right figure. The cross symbol indicates the control-on point. The arrow shows the direction of the trajectory. This trajectory goes outside the approximate domain of attraction of the open loop system. So it is the control that suppresses the first mode growth.

Figure 5-20 shows an unstable transient with constant gain control. In this case, the system goes into rotating stall. The mean flow shows strong oscillation before it

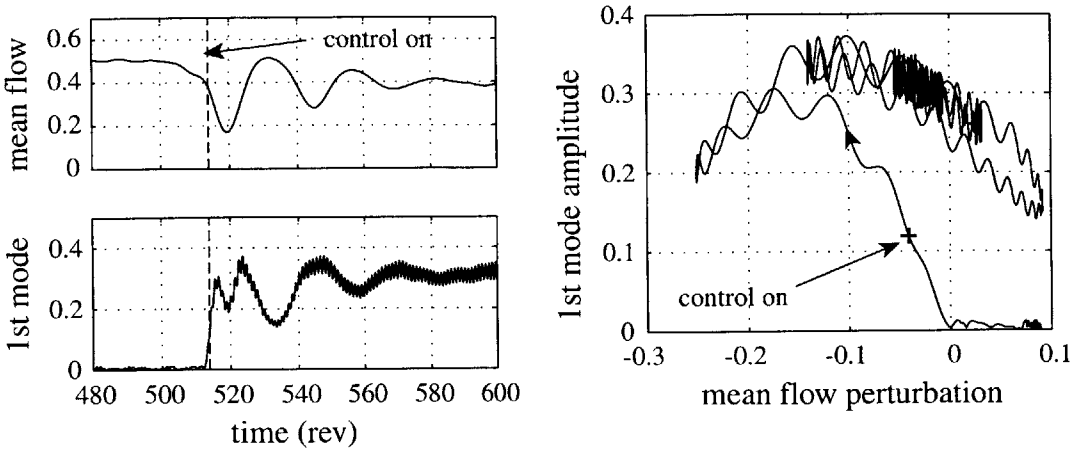


**Figure 5-20:** Unstable Transient With Constant Gain Control

falls to stalled mass flow. The cross symbol in the trajectory plot shows the control-on point is outside the approximate domain of attraction. The first mode has grown to a large value when the control is turned on.

Figure 5-21 shows the mean and first mode actuation of constant gain control (the same run as shown in Figure 5-19. There is a mean actuation level before the constant gain control is turned on. This is set to keep the equilibrium point without control the same as that with control. When the control is present, it reacts to noise even when the system is stable. This actuation level due to noise will effectively move the equilibrium point to higher mass flow. The figure shows that the actuation reacts to the perturbation correctly. In the left figure, we can also see that the mean actuation hit the saturation. It seems that the gain of the first mode control can be increased to get better results because it hasn't reached the saturation. But increasing the gain will also amplify the feedback of noise. It is undesirable to have the average actuation level too high when the system is stable.

Figure 5-22 shows the perturbation transients and the actuation for sliding mode control. We see that the sliding mode controller also reacts to the system perturbation correctly.

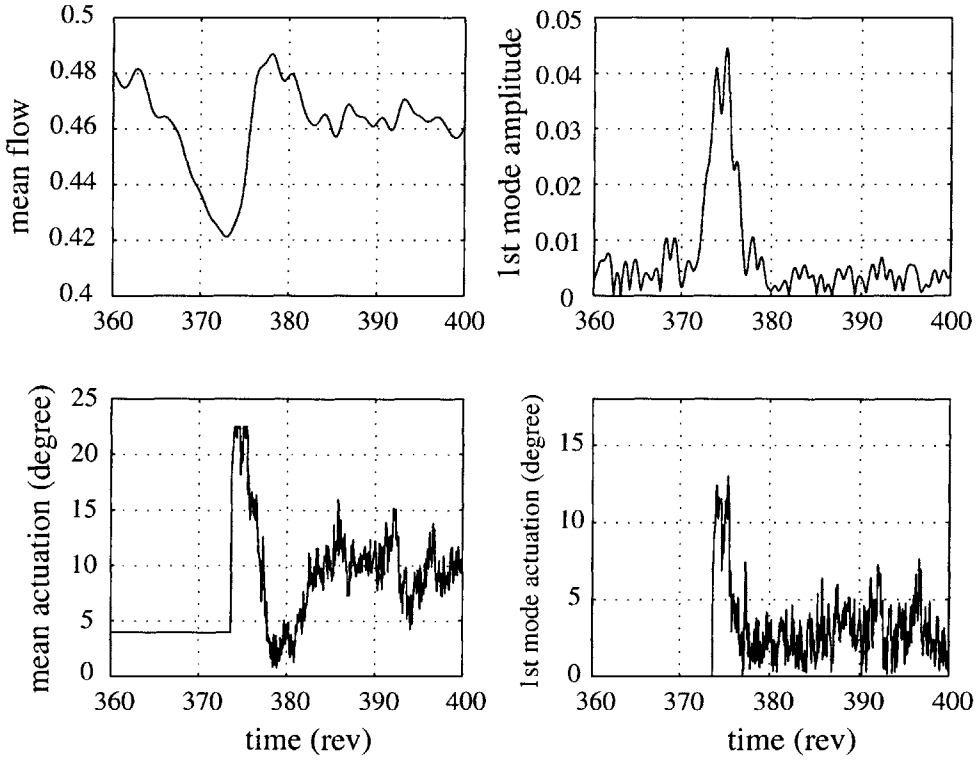


**Figure 5-21:** Actuation Traces of Constant Gain Control

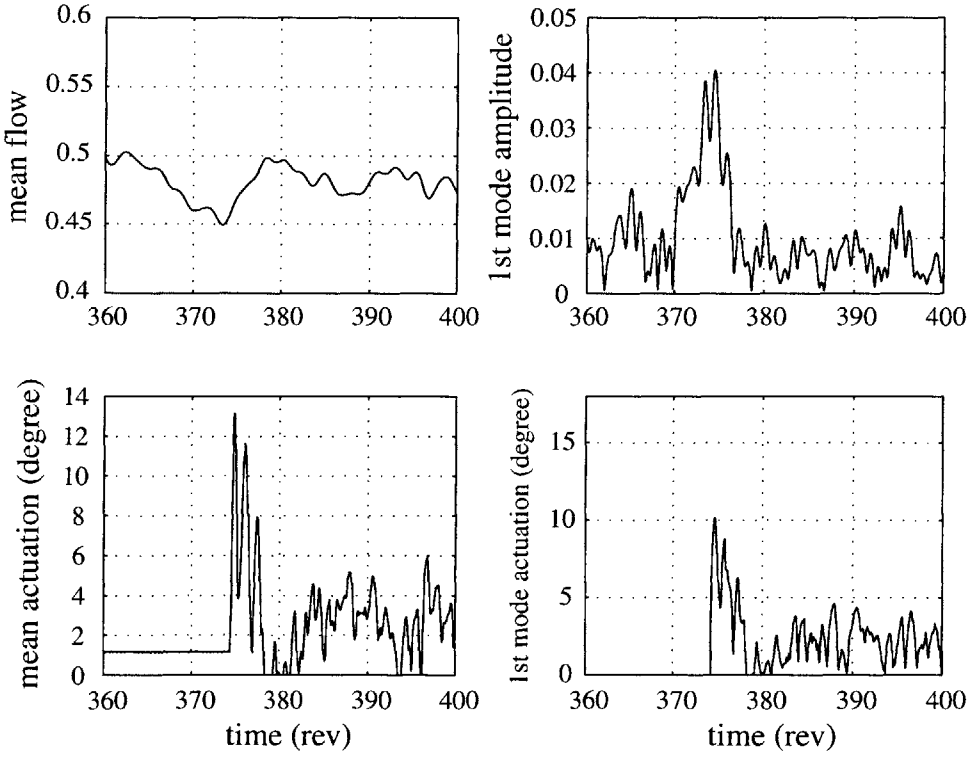


**Figure 5-22:** Actuation Traces of Sliding Mode Control

### 5.5.4 Validation of Domain of Attraction

As mentioned in Section 5.4.1, it is possible to examine whether the control-on points is located outside the approximate domain of attraction, when the system goes into rotating stall due to disturbances.

Figure 5-23 shows the unstable control-on points and the approximate domain of attraction with constant gain control. The tests were done by changing the time

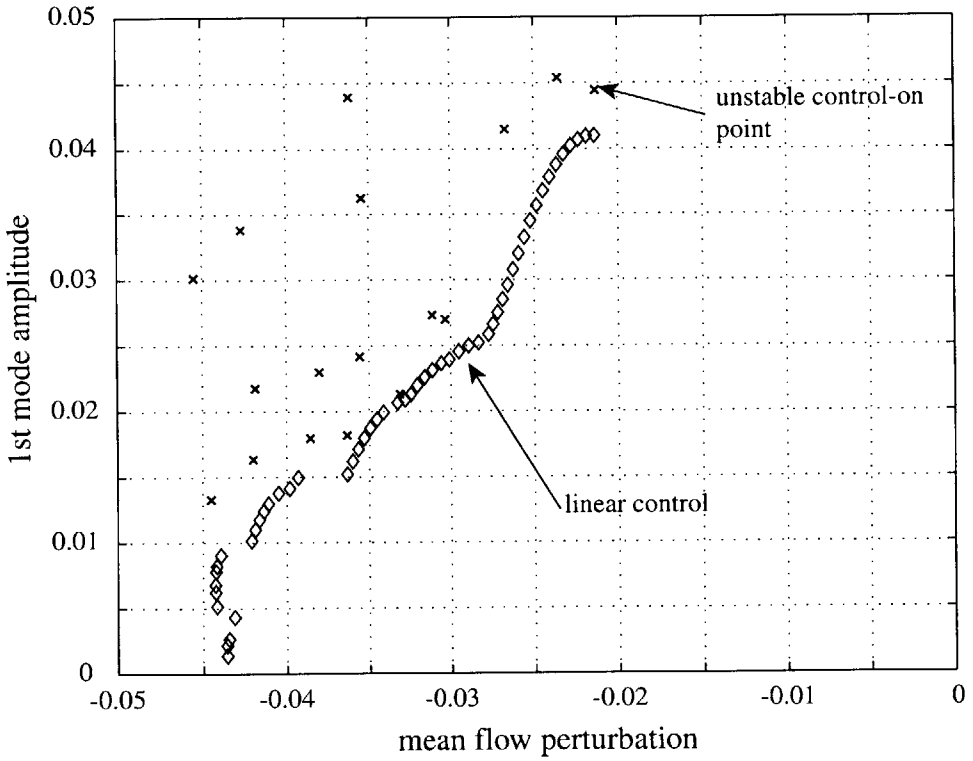


**Figure 5-23:** Validation of Domain of Attraction

period between closing the disturbance valve and turning control on. It is found that for all those unstable trajectories, their control-on points fall outside the approximate domain of attraction with constant gain control. In the figure, the cross symbols represent those unstable control-on points. These points spread over a wide region, which validates our measurements of the approximate domain of attraction. Some of the cross points are very close to the measured boundary, which means that the measured boundary of the approximate domain of attraction is very close to the stability boundary.

# Chapter 6

# Approximate Domain of Attraction for Distorted Flow

This chapter applies the concept of nonlinear stability considered in Chapter 5 for clean flow to the compression system with inlet distortion. The distortion is treated as a steady state background distorted flow. Based on this, the stability of the compression system is investigated in the face of disturbances. The active control schemes designed for the clean flow are used in the distorted flow. Numerical simulations are conducted to characterize the nonlinear stability.

## 6.1 Introduction

Inlet distortion is a very important factor that affects the stability of compression systems. Inlet distortion can be generated in many ways, like flow separation (in the inlet diffuser or at the inlet lip), shock wave/boundary layer interaction, vortex or boundary layer ingestion, etc. There are two classifications of inlet distortion: radial and circumferential. Inlet distortion can also be classified as total pressure distortion and total temperature distortion. The most frequently investigated inlet distortion is circumferential total pressure distortion, which is generated by a distortion screen located upstream of the compressor in research environments. For our purpose, this type of distortion can be easily included in our two dimensional system model.

As is customary, inlet distortion is treated here as a steady state phenomenon. Investigations have shown that the compression system responds to total pressure distortions which persist for a period of time on the order of one rotor revolution [33]. Other experiments concluded that screen-generated distortion test results can accurately predict the effect of inlet distortion [33]. We will adopt these traditional steady state assumptions of inlet distortion. In Hynes and Greitzer [22], the steady state distorted background flow was considered in their theory in a nonlinear way. Then small perturbations were added to this background distorted flow to see how the perturbations evolved, thereby judging the stability. The Hynes-Greitzer model successfully predicted the trends observed experimentally by Reid [37]. Van Schalkwyk [15] used active control to extend the stable operating range in a three-stage compressor with circumferential total pressure distortion. The experimental results shown by Van Schalkwyk (on the same compressor used in this thesis) are in good agreement with the Hynes-Greitzer model. As an extension, arbitrary amplitude disturbances are used to perturb the system. The domain of attraction under distorted background flow will be calculated by numerical simulations.

## 6.2 Domain of Attraction under Inlet Distortion

The total pressure inlet distortion can be modeled as [22]

$$\frac{\Delta P_t}{\rho U^2} = \frac{1}{2}\sigma\bar{\phi}S(\theta) \tag{6.1}$$

where $\Delta P_t$ is the total pressure difference across the distortion screen. $\sigma S(\theta)$ is a local screen loss parameter characterizing the circumferential shape of the total pressure loss [22]. $\sigma$ represents the strength of the distortion in terms of mean flow dynamic head. The distortion is shown in Figure 6-1. The extent used here is 120°, the same as in experiments by Van Schalkwyk [15]. Using the assumption of linearized duct flows, the inlet distortion is easily included into our compression system model. In

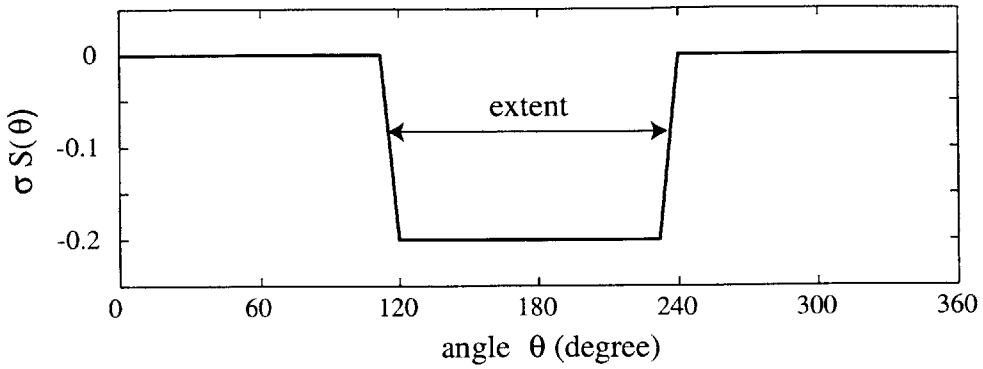


**Figure 6-1:** Inlet Distortion Magnitude and Extent

Equation (3.17), the term $\Psi_{dist}$ represents the total pressure inlet distortion

$$\Psi_{dist} = \frac{1}{2}\sigma\bar{\phi}S(\theta)$$

**Relative Angle of Distortion and Disturbances** When we impose the first mode perturbation, the relative angle of the distortion and the perturbation is an important parameter. Under inlet distortion, the steady axial velocity profile is no longer axisymmetric. This implies that the slope of the local compressor characteristic may vary from positive to negative. Perturbations can be amplified in some regions but attenuated in the other regions. Details can be found in [22, 15]. So it is important to account for the relative angle of the distortion and the disturbance. Figure 6-2 shows the configuration of the relative phase between the distortion and the perturbation, $\beta$. There exists a worst case angle which make the system most

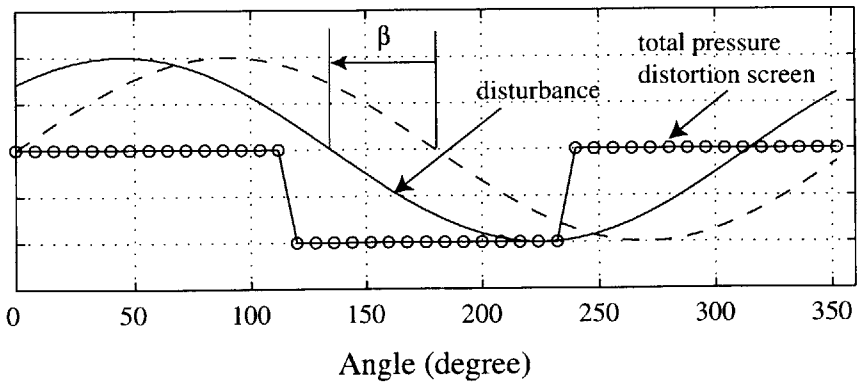


**Figure 6-2:** Relative Angle Between Distortion and Perturbation

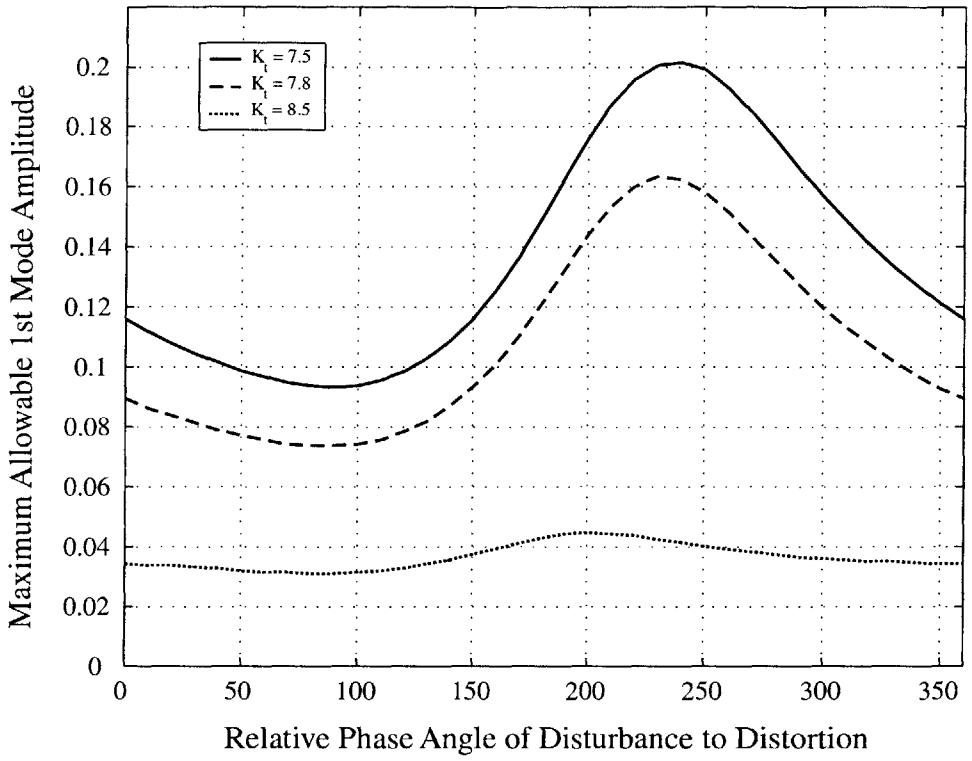


**Figure 6-3:** Determination of The Worst Relative Angle

unstable. In a real compression system, the perturbations are introduced randomly in frequency, magnitude and phase. So stability at the worst relative angle should be the stability criterion for practical operation.

The worst relative angle is obtained through numerical simulation. To do this, we assume the mean flow perturbation is zero. At each relative angle, the maximum allowable first mode magnitude is calculate by simulation. Figure 6-3 shows the simulation results. Three different throttle settings were tested. For each throttle setting, there are maximum and minimum values for maximum allowable first mode amplitude. For all three cases, the worst relative angle is almost constant, $\beta_{worst} = 90°$. In the following simulations, this value will be used to obtain the approximate domain of attraction.

**Domain of Attraction** The operating equilibrium point is changed by the presence of inlet distortion. In order to see how the inlet distortion affects the robustness of stability (domain of attraction), the following scenario is considered.

The throttle setting of the compression system is set. Then the inlet distortion comes in. The loss of robustness of stability is examined. Figure 6-4 shows the comparison of domain of attraction at a fixed throttle setting. Two of the distortion magnitudes (0.8

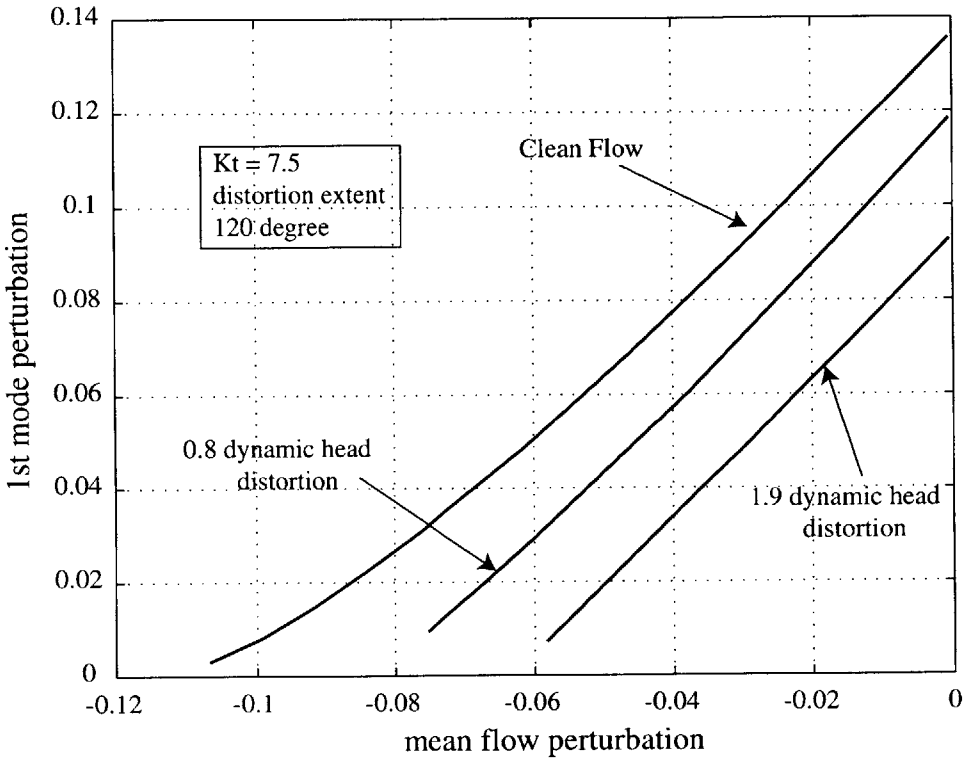


**Figure 6-4:** Domain of Attraction Under Inlet Distortions

and 1.9, which were in Van Schalkwyk's experiments [15]) are used to calculated the approximate domain of attraction. The approximate domain of attraction decreases when the magnitude of the distortion increases.

## 6.3 Active Control Under Inlet Distortion

In this section, both controllers used in the simulations and experiments for clean flow are applied to distorted flow. The motivation to directly use these two controllers is that the knowledge of inlet distortion is usually not available when the controllers are designed. It is desirable to have an active control scheme which doesn't need the knowledge of inlet distortion, but is effective in improving the nonlinear stability of

**Table 6.1:** Comparisons of Maximum Allowable First Mode Amplitude

| | no control | linear control | | sliding mode control | |
|---|---|---|---|---|---|
| | | $A_{1,max}$ | increase (%) | $A_{1,max}$ | increase (%) |
| clean flow | 0.0763 | 0.0826 | 8.26 | 0.0970 | 27.13 |
| 0.8 DH distortion | 0.0579 | 0.0655 | 13.13 | 0.0821 | 41.8 |
| 1.9 DH distortion | 0.0381 | 0.0491 | 28.87 | 0.0597 | 56.69 |

the compression system.

Two distortion strengths are simulated: 0.8 and 1.9 dynamic head (DH) base on the mean flow as mentioned above. The distortion extent is 120°. The comparisons are based on the same throttle setting ($K_t = 8.4$). Figure 6-5 shows the results of linear controls. From the figure, we see that the constant gain controls enlarge the

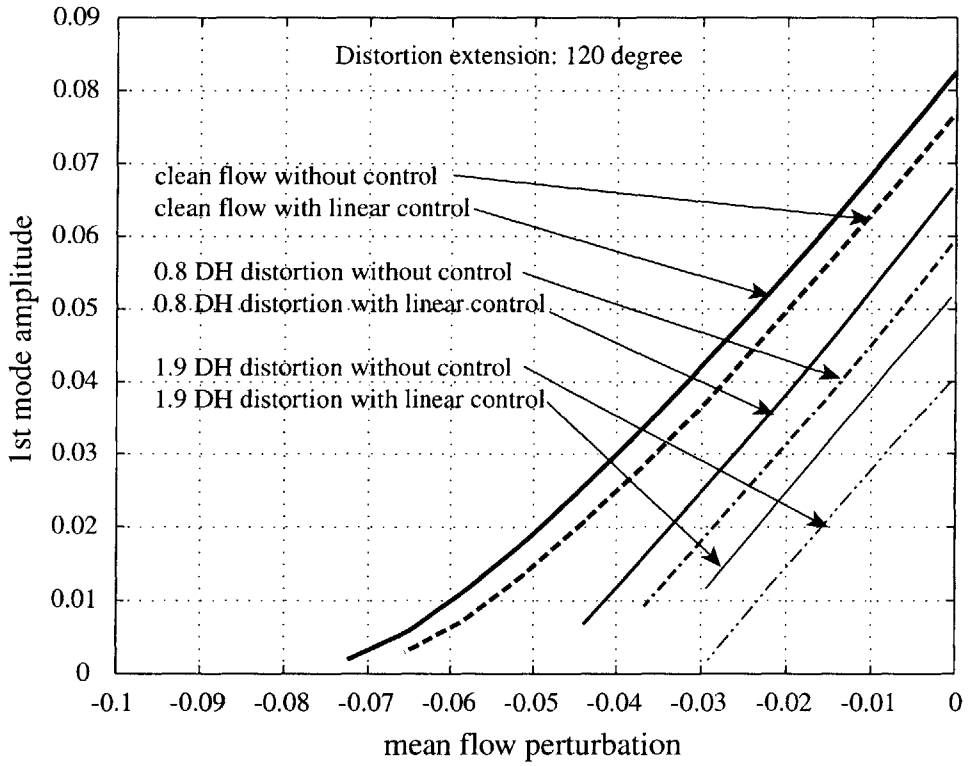


**Figure 6-5:** Linear Control Under Inlet Distortions

approximate domain of attraction with both distortion strengths. The increases of maximum allowable first mode amplitude are shown in Table 6.1. The percentage of increase becomes larger with increasing the distortion strength, which means that

there is more room to improve nonlinear stability by active control for inlet distortions. We also note that the approximate domain of attraction of 0.8DH distortion is still smaller than that of the open loop system. Inlet distortion is very harmful to the robustness of the system stability.

Figure 6.3 shows the simulation results of sliding mode control. The sliding mode

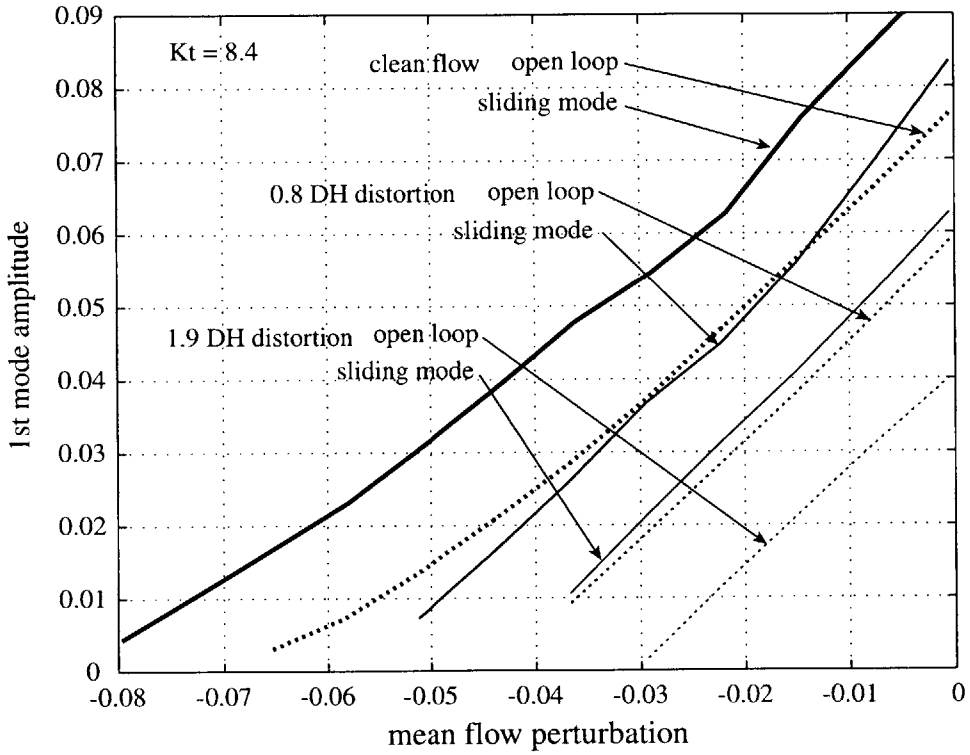


**Figure 6-6:** Sliding Mode Control Under Inlet Distortions

control enlarges the approximate domain of attraction for all three case as shown in the figure. From Table 6.1, we see that the sliding mode control is more effective than the linear control for both clean and distorted flows. We also note that, with sliding mode control, the controlled compressor is as effective at rejecting disturbances as the uncontrolled compressor, up to a distortion level of 0.8 dynamic head. Up to this level, active contrl eliminates the deleterious effects of inlet distortions. Figure 6-7 shows the profiles of distorted flow and bleed flow when the sliding mode control goes into steady state feedback. The bleed flow is lower when the the distorted flow is higher, while the bleed flow is higher when the distorted flow is lower. This means

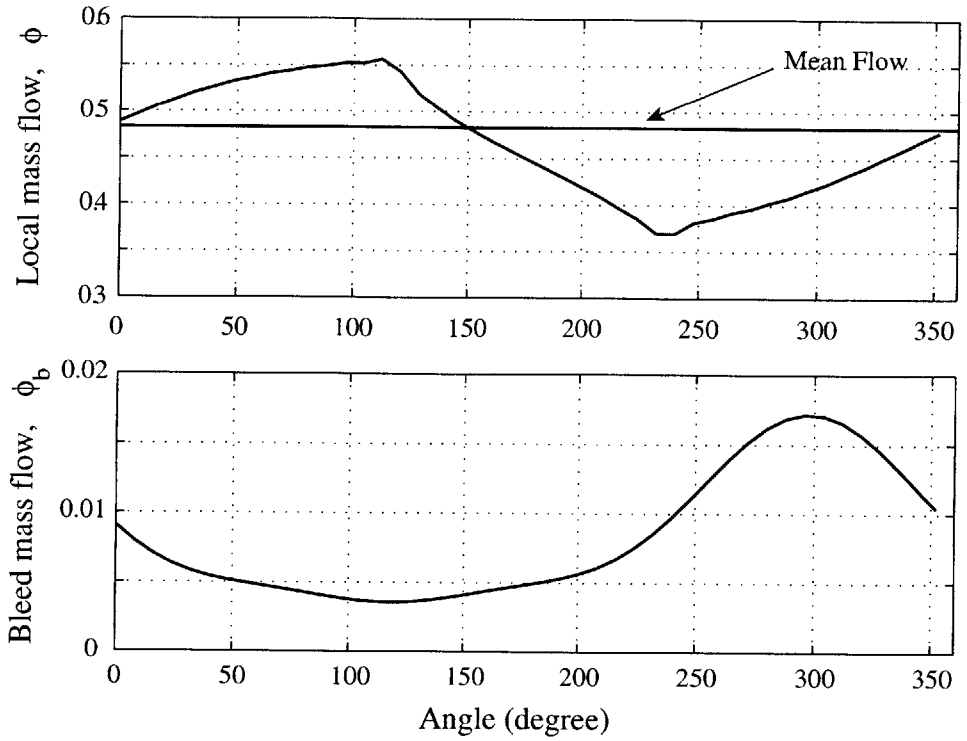


**Figure 6-7:** Flow Profiles of Sliding Mode Control

that the bleed flow reacts to the background distorted flow correctly. This verify the design of the sliding mode controller that the controller targets suppressing any possible deviations from the equilibrium point (uniform axial velocity).

# Chapter 7

# Summary, Conclusion and Recommendations

### 7.0.1 Summary

In this thesis, the issue of compressor stability is explored from a new point of view. Instead of trying to stabilize linearly unstable operating points, the operability or robustness of stability is considered. Simulations and experiments were done to characterize and improve the robustness of stability on a low-speed multistage compressor.

Chapter 2 described the experimental rig. A plenum disturbance valve was built to introduce disturbances into the system. A data processing technique is also constructed to extract the rotating waves in the environment of low signal-to-noise ratio.

Chapter 3 presented a downstream bleed model which includes the gap between compressor exit and the bleed valves and the discrete nature of the actuation. Forced response tests were also described in which tests were conducted at different mass flows to verified the downstream bleed model. Chapter 4 tested the control effectiveness of the downstream bleed in extending the stable operating range. In these tests, only four bleed valves were used.

Chapter 5 discussed the nonlinear stability. A measure of nonlinear stability, called domain of attraction was introduced. Simulations and experiments quantified

the domain of attraction for both open loop systems and active controlled systems when no inlet distortion is present. Chapter 6 calculated approximate domain of attraction with inlet distortions. Active controls were also applied to the distorted flows.

### 7.0.2 Conclusions

The following conclusions can be drawn from this research:

1. The quantitative characterization of disturbance rejection ability or robustness of stability in a realistically scaled compressor can be measured experimentally.

2. The two-dimensional downstream bleed is a viable control approach. Specifically, the following sub-conclusions can be drawn.

   - The model captures the essential physics of the downstream bleed.
   - Physical and beneficial effects of downstream bleed are elucidated.
   - The only four bleed valves are able to achieve 2% of range extension which is comparable to that of other actuators

3. The nonlinear performance (disturbance rejection) of the compressor can be improved by active control. The four bleed valves double the maximum allowable amplitude of the zeroth and first mode perturbations.

4. With the sliding mode control, the compressor with an inlet distortion level up to 0.8 dynamic head based on the mean flow, is as effective in disturbance rejection as the uncontrolled compressor.

### 7.0.3 Recommendations for Future Work

This research has proposed that the domain of attraction provides a better characterization of compressor stability than linear analysis. The experiments also demon-

strate the possibility to enhance it by active control. In order to extend this idea to industry, the following further research is recommended:

1. The use of domain of attraction in industry needs to be explored. The benefits of making the system robust to disturbances needs to be quantified. How to use this new information in the design process is also important.

2. Further modeling effort is needed to improve the predictive capability of the model. This is useful for designing more effective nonlinear controllers.

3. Extending this idea to high speed compressors is desirable. The questions might be: What factors determine the domain of attraction? Can active control enhance the robustness of high-speed compressors? How large a benefit is it possible to achieve?

4. Because the domain of attraction is a nonlinear property, careful nonlinear control design is needed. Actuation saturation needs to be included into nonlinear control design.

# BIBLIOGRAPHY

[1] Emmons, H. W., Pearson, C. E. and Grant, H. P., *Compressor Surge and Rotating Stall Propagation*, Transactions of the ASME, vol. 79, pp 455-469, 1955.

[2] Greitzer, E. M., *The Stability of Pumping Systems - The 1980 Freeman Scholar Lecture*, J Fluids Engineering, Vol. 103, pp 193-242, 1981.

[3] McDougall, N. M., *Stall Inception in Axial Compressors*, PhD thesis, Cambridge University, 1988.

[4] Garnier, V. H., Epstein, A. H., and Greitzer, E. M., *Rotating Stall Waves As A Stall Inception Indication in Axial Compressors", ASME J. Turbomachinery*, vol. 113, pp 290-302, 1991.

[5] Day, I. J., *Stall Inception in Axial Compressors*, ASME J. Turbomachinery, vol. 115, pp 1-9, 1993.

[6] Greitzer, E. M., *Surge and Rotating Stall in Axial Flow Compressors, Part I and II*, J. Engineering for Power, vol. 98, No. 2, pp 190-217, 1976.

[7] Moore, F. K., *A Theory of Rotating Stall of Multistage Compressors, Part I - III*, ASME J. Engineering for Power,vol 106, pp 313-336, 1984.

[8] Bonnaure, L. P., *Modeling High Speed Multistage Compressor Stability*, Master thesis, Department of Aeronautics and Astronautics, MIT, 1991.

[9] Feulner, M. R., Hendricks, G. J. and Paduano, J. D., *Modeling for Control of Rotating Stall in High Speed Multi-Stage Axial Compressors*, ASME Paper 94-GT-292.

[10] Weigl, H. J., *Active Stabilization of Rotating Stall and Surge in a Transonic Single Stage Axial Compressor*, PhD Thesis, Department of Aeronautics and Astronautics, MIT, 1997.

[11] Epstein, A. H., Ffowcs Williams, J. E. and Greitzer, E. M., *Active Suppresion of Aerodynamic Instabilities in Turbomachines*, AIAA J. Propulsion and Power, Vol. 5, pp 204-211, 1989.

[12] Ffowcs Williams, J. E. and Huang, X., *Active Stabilization of Compressor Surge*, J. Fluid Dynamics, vol. 204, pp 245-262.

[13] Simon, J. S., Valavani, L., Epstein, A. H. and Greitzer, E. M., *Evaluation of Approaches to Active Compressor Surge Stabilization*, ASME J. Turbomachinery, Vol. 115, pp 57-67, 1993.

[14] Lavrich, P. L., *Time Resolved Measurement of Rotating Stall in Axial Flow Compressors*, MIT GTL Report No. 194, 1988.

[15] Van Schalkwyk, C. M., *Active Control of Rotating Stall With Inlet Distortion*, PhD thesis, Department of Aeronautics and Astronautics, MIT, 1996.

[16] Vo, H. D., *Active Control of Rotating Stall in a Three-Stage Axial Compressor With Jet Actuators*, Matser thesis, Master thesis, Department of Aeronautics and Astronautics, MIT, 1997.

[17] Protz, J. M., *Nonlinear Active Control of Rotating Stall and Surge*, Matser thesis, Master thesis, Department of Aeronautics and Astronautics, MIT, 1997.

[18] Moore, F. K. and Greitzer, E. M., *A Theory of Post-Stall Transients in Axial Compressors, Part I & II*, ASME J. of Engineering for Gas Turbine and Power, Vol. 108, pp 68-76, 231-239, 1986.

[19] Paduano, J. D., *Active Control of Rotating Stall in Axial Compressors*, PhD thesis, Department of Aeronautics and Astronautics, MIT, 1992.

[20] Haynes, J. M., *Active Control of Rotating Stall in a Three-Stage Axial Compressor*, Master thesis, Department of Aeronautics and Astronautics, MIT, 1993.

[21] Haynes, J. M., Hendricks, G. J. and Epstein,A. H., *Active Stabilization of Rotating Stall in a Three-Stage Axial Compressor*, ASME J. of Turbomachinery, Vol. 116, pp 226-239, 1994.

[22] Hynes, T. P. and Greitzer, E. M., *A Method for Assesing Effects of Circumferential Flow Distortion on Compressor Stability*, ASME J. of Turbomachinery, Vol. 109, pp 371-379, July 1987.

[23] Lonley, J. P., *Inlet Distortion and Compressor Stability*, PhD Thesis, Trinity College, Cambridge University, 1988.

[24] Hoying, D. A., Tan, C. S., Vo, H. D. and Greitzer, E. M., *Role of Blade Passage Flow Structures in Axial Compressor Rotating Stall Inception*, ASME paper 98-GT-588.

[25] Gong, Y., *A Computational Model for Rotating Stall and Inlet Distortions in Multistage Compressors*, PhD thesis, Department of Aeronautics and Astronautics, MIT, 1999.

[26] McCaughan, F. E., *Application of Bifurcation Theory to Axial Flow Compressor Stability*, ASME J. Turbomachinery, vol 3, pp 426-433, 1989.

[27] Mansoux, C, *Distributed Nonlinear Stability Analysis of Rotating Stall*, Master thesis, Department of Aeronautics and Astronautics, MIT, 1994.

[28] Setiawan, J. D., *Distortion Tolerance of Stall/Surge Controllers in Axial Compression Systems*, Master thesis, Department of Aeronautics and Astronautics, MIT, 1996.

[29] Eveker, K. M., Gysling, D. L., Nett, C.N. and Sharma, O. P., *Integrated Control of Rotating Stall and Surge in a Low Speed Axial Compression System*, Proceedings of SPIE, vol 2494, pp 17-18,1995.

[30] Eveker, K. M., Gysling, D. L., Nett, C.N. and Sharma, O. P., *Integrated Control of Rotating Stall and Surge in a High-Speed Multi-Stage Compression System*, ASME paper 97-GT-352.

[31] D'Andrea, R., Behnken, R. L. and Murray, R. M., *Active Control of an Axial Flow Compressor via Pulsed Air Injection*, ASME J. Turbomachinery, pp 742-752, 1998.

[32] Yeung, S., *Nonlinear Control of Rotating Stall and Surge with Axisymmetric Bleed and Air Injection on Axial Flow Compressors*, PhD thesis, California Instaitute of Technolgy, 1998.

[33] Collins, T. P., *Engine Stability Considerations*, AFAPL-TR-78-52, The Aerothermodynamics of Aircraft Gas Turbine Engines, Chapter 23.

[34] Fahim, A, *Experimental Evaluation Of Asymmetric Bleed Actuation For Rotating Stall And Surge Control*, Master thesis, Department of Aeronautics and Astronautics, MIT, 1998.

[35] Chi, John N., *Air Injection In Axial Compressors: Modeling, Experimental Validation, And Control of Instabilities*, PhD thesis, Department of Aeronautics and Astronautics, MIT, 1999.

[36] Spakovszky, Z. S., Weigl, H. J., Paduano, J. D., Van Schalkwyk, C. M., Suder, K. L., Bright, M. M. and Strazisar, A. J., *Rotating Stall Control in a High Speed Stage With Inlet Distortion, Part I: Radial Distortion, Part II: Circumferential Distortion*, ASME paper 98-GT-264, 98-GT-265.

[37] Reid, C., *The Resopnse of Axial Flow Compressors to Intake Flow Distortion*, ASME paper 69-GT-29, 1969.

[38] Oppenheim, A. V., Willsky, A. S. and Nawab, S. H., *Signals and Systems*, Prentice Hall, 1997.

[39] Slotine, J.-J. E. and Li, W., *Applied Nonlinear Control.* Prentice-Hall, 1991.

[40] Greitzer, E. M., *Coupled Compressor-Diffuser Flow Instability*, J Aircraft, Vol. 14, No. 3, March 1977, pp 233-238.

[41] Liaw, D. C. and Abed, E. H., *Stability Analysis and Control of Rotating Stall*, Proceedings of the 2nd IFAC Nonlinear Control Systems Design Symposium, June 1992.

# APPENDIX A

# A BAND PASS FILTER SENSITIVE TO ROTATING WAVES

As mentioned in Chapter 2, direct estimate of the first mode amplitude is very noisy. In this appendix, a band pass filter which is sensitive to rotating waves is designed to filter out those non-rotating contents and contents of irrelevant rotating frequencies.

Because rotating stall wave is rotating around the annulus at some constant speed, it is better represented as a phasor. For convenience, we only present the case of the first spatial mode. Higher spatial modes can be treated exactly the same. A phasor can be written as a complex expression:

$$\phi(t) = a(t) + jb(t) \tag{A.1}$$

The opposite direction one is written as

$$\phi^*(t) = a(t) - jb(t) \tag{A.2}$$

where $a(t)$ and $b(t)$ are the spatial cosine and sine coefficients of the rotating wave respectively.

A band-pass filter was designed to pass the first spatial mode rotating frequency.

We write the filter as $G_1(s)$ which is a real coefficient transfer function. The filtered version of rotating phasor can be written as

$$\phi_I(t) = G_1(s)\phi(t) \tag{A.3}$$

Figure A-1 shows the spectrum of the original and filtered signal and filter.

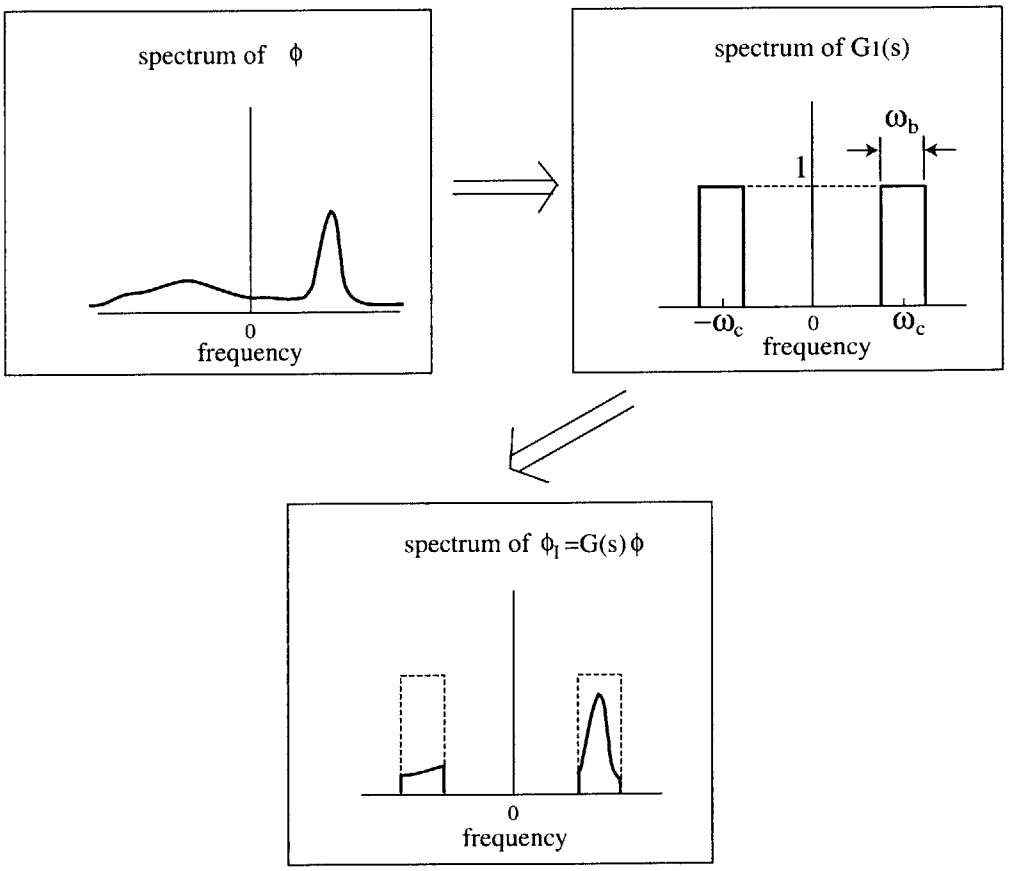


**Figure A-1:** Spectrum of signals and filter

A real coefficient filter passes both the positive and negative frequency band symmetrically. The resulting signal still has negative frequency content. Here we assume that this negative frequency content is caused by some stationary waves (e.g. distortion) which we do not want to measure. These stationary waves have symmetric spectrum in positive and negative frequencies. In order to filter out these stationary waves, The following filter was designed [38]. First, a low pass filter $G'(s)$ with half-width band of the above band pass filter was designed. Then the following filtering

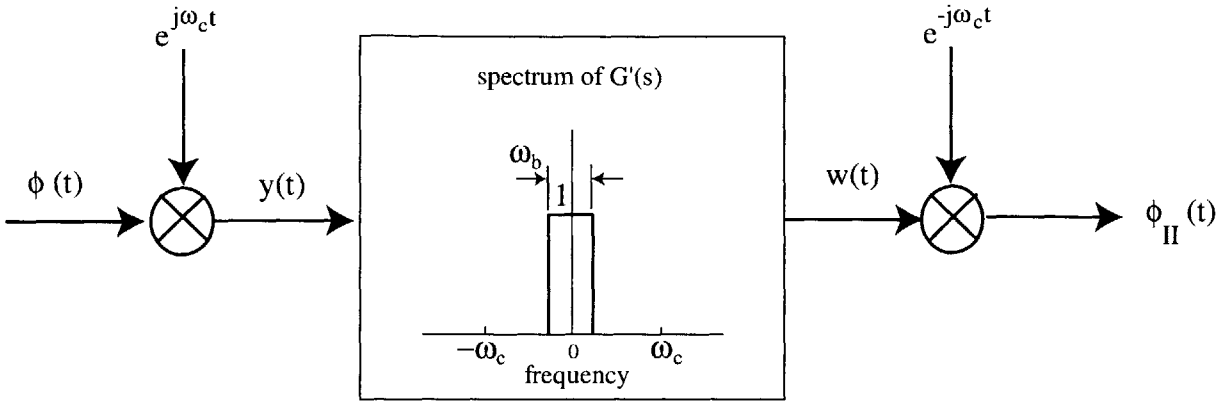


**Figure A-2:** Selective Frequency Filter

scheme was performed, as shown in Figure A-2. The spectrum of $y(t)$,$w(t)$ and $\phi_{II}(t)$ are shown in Figure A-3. The signal is first multiplied by $e^{j\omega_c t}$. The resulting spectrum is shifted by $\omega_c$ ($\omega_c$ is the center frequency of the above band pass filter). After passing through low pass filter, the resulting filtered spectrum is shifted back by multiplying $e^{-j\omega_c t}$. The resulting signal is $\phi_{II}(t)$. We write this as

$$\phi_{II}(t) = e^{-j\omega_c t} G'(s)[\phi(t) e^{j\omega_c t}] \tag{A.4}$$

where $G_2(s)$ represents the whole filter shown in Figure A-2. Then the final signal $\phi_f$ by rotating filtering is

$$\phi_f(t) = \phi_I(t) - 2Re(\phi_{II}(t)) \tag{A.5}$$

A filtering example is shown in Figure 2-7, in which we see that the filter performs very well.

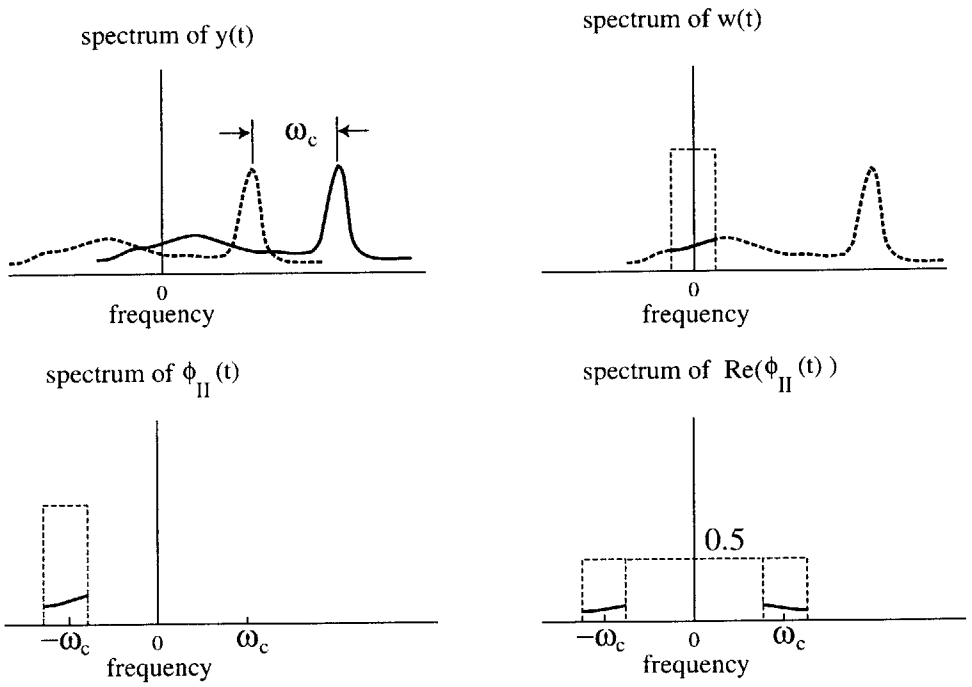


**Figure A-3:** Spectrum of $y(t)$,$w(t)$ and $\phi_{II}(t)$

# Appendix B

# Inter-Stage Bleed Model

Inter-stage bleed valves exist in aero-engines for many reasons. There are bleed valves for cooling turbine blades, avoiding instabilities at takeoff, etc. Especially for those bleed valves used at takeoff, they are possible to be used systematically for active control purpose. Downstream bleed model derived in Chapter 3 can be extended to inter-stage bleed. Figure B-1 shows the configuration and notations of inter-stage bleed model.

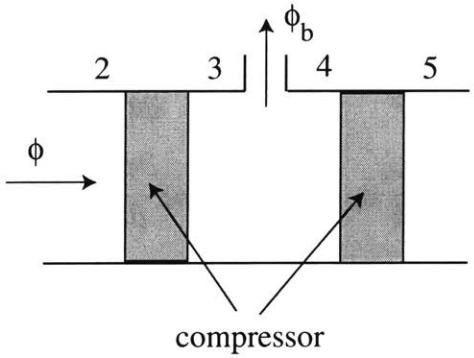


**Figure B-1:** Schematic of Inter-Stage Bleed

The bleed can be modeled similarly as in Equation (3.1), (3.6) and (3.7):

$$\phi_3 - \phi_4 = \phi_b \tag{B.1}$$

$$\psi_4 - \psi_3 = \phi_3 \phi_b \tag{B.2}$$

The compressor is divided into two parts by the inter-stage bleed valves. The inertia and effective length of these two segments of compressor are $\lambda_1$, $\mu_1$ and $\lambda_2$, $\mu_2$ respectively. The pressure rise for these two parts of compressor are $\psi_{c1}$ and $\psi_{c2}$. We also use the following definitions

$$l_{c1} = l_I + \mu_1, \quad l_{c2} = l_e + \mu_2$$

where $l_I$ and $l_e$ are upstream and downstream duct length respectively as defined in Figure 3-1. The unsteady performance of the two parts of compressor can be written as follows

$$\frac{P_3 - P_{t2}}{\rho U^2} = \psi_{c1}(\phi_3) - \lambda_1 \frac{\partial \phi_3}{\partial \theta}|_{\eta=0} - \mu_1 \frac{\partial \phi_3}{\partial t}|_{\eta=0}$$

$$\frac{P_5 - P_4}{\rho U^2} = \psi_{c2}(\phi_4) - \lambda_2 \frac{\partial \phi_4}{\partial \theta}|_{\eta=0} - \mu_2 \frac{\partial \phi_4}{\partial t}|_{\eta=0}$$

where $\eta$ is the coordinate along axial direction with origin at compressor face. By considering the mass and momentum addition of bleed valves as in Equation (B.1) and (B.2), we can get

$$\begin{aligned} \frac{P_5 - P_{t2}}{\rho U^2} &= \psi_c(\phi_3) - \lambda \frac{\partial \phi_3}{\partial \theta} - \mu \frac{\partial \phi_3}{\partial t} \\ &- \frac{\partial \psi_{c2}}{\partial \phi}\phi_b + \lambda_2 \frac{\partial \phi_b}{\partial \theta} + \mu_2 \frac{\partial \phi_b}{\partial t} + \phi_3 \phi_b \end{aligned} \tag{B.3}$$

where $\psi_c(\phi) = \psi_{c1}(\phi) + \psi_{c2}(\phi)$. Also a linearization is made as

$$\psi_{c2}(\phi_4) = \psi_{c2}(\phi_3 - \phi_b) = \psi_{c2}(\phi_3) - \frac{\partial \psi_{c2}}{\partial \phi}\phi_b$$

The pressure relations in upstream and downstream ducts can be derived in the exact same way as in Reference [18, 22]. The station numbers and notations are specified in Figure 3-1 except the part of compressor and bleed valves shown in Figure B . From now on, the subscript 3 of $\phi_3$ will be eliminated. $\phi$ denotes the mass

flow coefficient at compressor face. The upstream pressure relation is

$$\frac{P_{t2} - P_{t0}}{\rho U^2} = -\frac{1}{|n|}\frac{\partial \delta\phi}{\partial t} - l_I \frac{\partial \bar{\phi}}{\partial t} + \Psi_{dist}(\theta) \tag{B.4}$$

where $\Psi_{dist}(\theta)$ is the total pressure loss across the distortion screen (see Section 6.2 for details). The downstream pressure relation is

$$\frac{P_6 - P_5}{\rho U^2} = -l_e \frac{\partial(\bar{\phi} - \bar{\phi}_b)}{\partial t} - (m-1)\frac{1}{|n|}\frac{\partial \delta(\phi - \phi_b)}{\partial t} \tag{B.5}$$

where we substitute $(\phi_3 - \phi_b)$ into $\phi_5 = \phi_4$. m is the pressure redistribution parameter with a value of 2.0 for long ducts or 1.0 for short ducts.

By combining Equation (B.3 – B.5), the overall equation can be written as

$$l_c \frac{\partial \bar{\phi}}{\partial t} + \lambda \frac{\partial \delta\phi}{\partial \theta} + (\mu + \frac{m}{|n|}\frac{\partial \delta\phi}{\partial t} = \psi_c(\phi) - \psi + \Psi_{dist} + \Psi_{bleed} \tag{B.6}$$

where $\psi = P_6/\rho U^2$ is the plenum pressure. $l_c = l_{c1} + l_{c2}$ is the overall length of the compression system. We can assume the pressure rise of the second part of the compressor is a fraction ($\alpha$) of the entire compressor, $\psi_{c2} = \alpha\psi_c$. Also, if the compressor stages are identical (e.g. in GTL low speed compressor), the same fraction is valid for effective length and inertia. Then we write the pressure term due to inter-stage bleed $\Psi_{dist}$ as

$$\Psi_{dist} = (\phi - \alpha m_c)\phi_b + \alpha\lambda \frac{\partial \delta\phi_b}{\partial \theta} + l_{c2}\frac{\partial \bar{\phi}_b}{\partial t} + (\alpha\mu + \frac{m-1}{|n|})\frac{\delta\phi_t}{\partial t} \tag{B.7}$$

$$m_c = \frac{\partial \psi_c}{\partial \phi}$$

For control purposes, the above dynamic equation is still too complicated to use in control design. A model of reduced order is desired in this situation. The Galerkin projection is a suitable method which assumes the spatial shapes of the solutions

based on a series of trial functions. Here sine and cosine function are chosen as the trial functions. Let

$$\delta\phi(t,\theta) = a(t)cos\theta + b(t)sin\theta \tag{B.8}$$

The compressor characteristics is assume to be a cubic function

$$\psi_c(\phi) = k_3\phi^3 + k_2\phi^2 + k_1\phi + k_0 \tag{B.9}$$

So

$$\psi_c^{'}(\phi) = 3k_3\phi^2 + 2k_2\phi + k_1$$

$$\psi_c^{''}(\phi) = 6k_3\phi + 2k_2$$

$$\psi_c^{'''}(\phi) = 6k_3$$

By applying Galerkin projection to Equation (B.6), we obtain

$$\begin{cases} \dot{\bar{\phi}} = \dfrac{1}{l_c}\left[\psi_c(\phi) + \dfrac{1}{4}\psi_c^{''}(\bar{\phi})(a^2+b^2) - \psi + \bar{\Psi}_{dist} + \bar{\Psi}_{bleed}\right] \\ \dot{\psi} = \dfrac{1}{4l_cB^2}(\bar{\phi} - \bar{\phi}_b - \sqrt{\dfrac{2\psi}{K_t}}) \\ \dot{a} = \dfrac{1}{\mu+m}\left\{[\psi_c^{'}(\bar{\phi}) + \dfrac{1}{8}\psi_c^{'''}(\bar{\phi})(a^2+b^2)]a - \lambda b + \hat{\Psi}_{dist}^{a} + \hat{\Psi}_{bleed}^{a}\right\} \\ \dot{b} = \dfrac{1}{\mu+m}\left\{[\psi_c^{'}(\bar{\phi}) + \dfrac{1}{8}\psi_c^{'''}(\bar{\phi})(a^2+b^2)]b - \lambda a + \hat{\Psi}_{dist}^{b} + \hat{\Psi}_{bleed}^{b}\right\}, \end{cases} \tag{B.10}$$

where $\hat{\Psi}_{dist}^{a}$ and $\hat{\Psi}_{dist}^{b}$ are the first cosine and sine spatial Fourier coefficients of the distortion. $\hat{\Psi}_{bleed}^{a}$ and $\hat{\Psi}_{bleed}^{b}$ are the first cosine and sine spatial Fourier coefficients of the pressure rise due to inter-stage bleed.

# APPENDIX C

# SLIDING MODE CONTROL DESIGN

The model used for designing sliding mode controller was written into perturbation form as shown in Equation (5.5). We rewrite it here by substituting with Equation (5.6).

$$E_\phi \dot{\tilde{\underline{w}}} = E_A \tilde{\underline{w}} + f(\underline{w}^*, \tilde{\underline{w}}) + \underline{\tau} \tag{C.1}$$

The states of system are local mass flows and plenum pressure. Because of symmetry, there is no preferred circumferential location. The sliding surface $s(\underline{w}, t)$ is defined as

$$s(\underline{w}, t) = \tilde{\underline{w}} \tag{C.2}$$

The sliding surface is actually a physical surface or physical point which is equilibrium point. The control goal is to make the system trajectories approach to this surface: $s = 0$ or $\tilde{\underline{w}} = 0$. T do this, the following sliding condition is required

$$\frac{1}{2}\frac{d}{dt}(\tilde{\underline{w}}^T E_\phi \tilde{\underline{w}}) \leq -\eta(\tilde{\underline{w}}^T \tilde{\underline{w}})^{1/2} \tag{C.3}$$

where $\eta$ is a strictly positive number. $E_\phi$ is a positive definite matrix (see Man-

soux [27]). Expanding the sliding condition gives

$$\underline{\tilde{w}}^T E_\phi \dot{\underline{\tilde{w}}} \leq -\eta(\underline{\tilde{w}}^T \underline{\tilde{w}})^{1/2}$$

Substituting Equation (C.1) into the above sliding condition gives

$$\underline{\tilde{w}}^T E_A \underline{\tilde{w}} + \underline{\tilde{w}}^T f(\underline{w}^*, \underline{\tilde{w}}) + \underline{\tilde{w}}^T \underline{\tau} \leq -\eta(\underline{\tilde{w}}^T \underline{\tilde{w}})^{1/2} \tag{C.4}$$

The estimate of desired control due to model uncertainties can be written as

$$\underline{\hat{\tau}} = -\hat{E}_A \underline{\tilde{w}} - \hat{f}(\underline{w}^*, \underline{\tilde{w}}) \tag{C.5}$$

In order to account for these model uncertainties, an additional term is added to the estimate of desired control. So we have

$$\underline{\tau} = \underline{\hat{\tau}} - \underline{k} sign(\underline{\tilde{w}}) \tag{C.6}$$

Substituting the above control into Equation (C.4) gives

$$\underline{\tilde{w}}^T \Delta\hat{E}_A \underline{\tilde{w}} + \underline{\tilde{w}}^T \Delta\hat{f}(\underline{w}^*, \underline{\tilde{w}}) - \underline{\tilde{w}}^T \underline{k} sign(\underline{\tilde{w}}) \leq -\eta(\underline{\tilde{w}}^T \underline{\tilde{w}})^{1/2}$$

where $\Delta\hat{E}_A = E_A - \hat{E}_A$, $\Delta\hat{f} = f - \hat{f}$. In order to satisfy the sliding condition, the gain matrix can be chosen as a diagonal matrix and satisfies

$$k_i \geq |[\Delta\hat{E}_A \underline{\tilde{w}} + \Delta\hat{f}(\underline{w}^*, \underline{\tilde{w}})]_i| + \eta \tag{C.7}$$

As we see, the additional control term is a discontinuous term. Here a smoothing technique suggested by Slotine [39] is used. The final form of the sliding mode control is

$$\underline{\tau} = -\hat{f}(\underline{w}^*, \underline{\tilde{w}}) - \hat{E}_A \underline{\tilde{w}} - \underline{k} sat(\underline{\tilde{w}}/W) \tag{C.8}$$

where $W$ is a smoothing factor and

$$sat(y) = \begin{cases} sign(y), & |y| > 1, \\ y, & |y| \leq 1 \end{cases}$$

# Appendix D

# Downstream Diffuser

The coupling between the compressor and downstream diffuser has been investigated by [40]. Here a brief qualitative explanation of the effect on the stability of the diffuser is given.

The diffuser can be modeled in Figure D-1. The mass and momentum conserva-

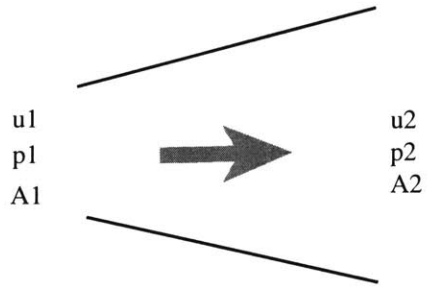


**Figure D-1:** Diffuser

tion can be written as (incompressible, inviscid)

$$u_1 A_1 = u_2 A_2 or u_2 = \frac{A_1}{A_2} u_1$$

$$p_1 + \frac{1}{2}\rho u_1 = p_2 + \frac{1}{2}\rho u_2$$

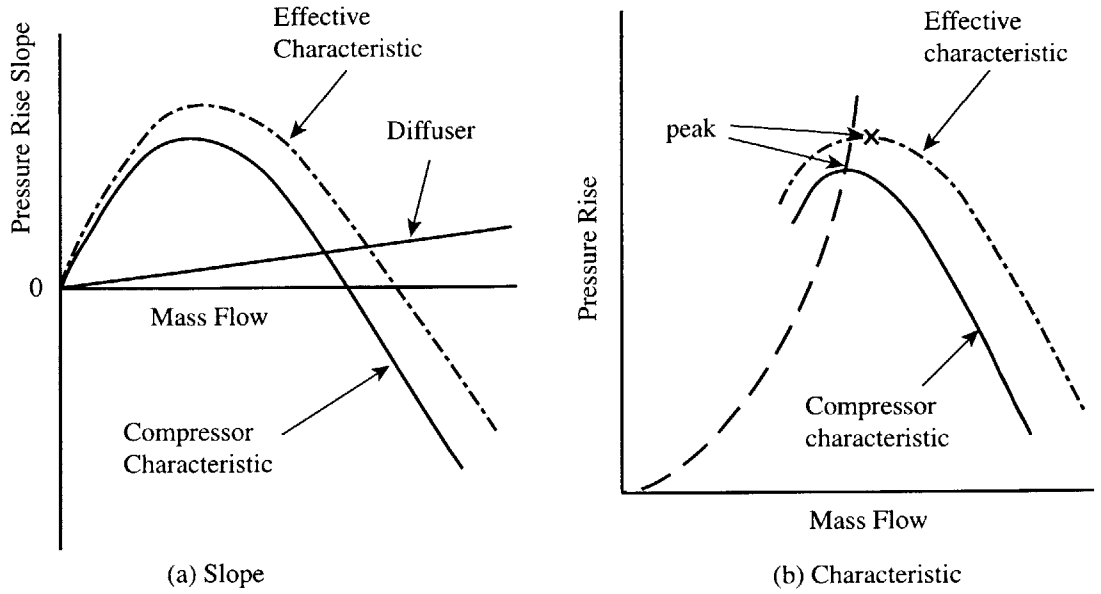


**Figure D-2:** The Effective Compressor Characteristic

Non-dimensionalization as shown in Chapter 3 gives

$$\Delta\psi = \frac{1}{2}[1 - (A_1/A_2)^2]\phi^2 \tag{D.1}$$

The slope of the pressure rise of the diffuser with respect to the mass flow is then

$$\frac{d\Delta\psi}{d\phi} = [1 - (A_1/A_2)^2]\phi \tag{D.2}$$

If we assume the compressor characteristic is a cubic curve as shown in [18], we can draw an effective compressor characteristic including the effects of the diffuser. In Figure D-2(a), It is shown that the pressure rise peak (zero slope) is shifted to a higher mass flow by the effects of the diffuser. So a downstream diffuser will destabilize the compressor. Figure D-2(b) shows the effective compressor characteristic.